Università degli Studi di Napoli *Federico II*

DOTTORATO DI RICERCA IN FISICA

Ciclo XXIX

Coordinatore: Prof. Salvatore Capozziello

Development of the Spectral Analysis System for a Spaceborne High Spectral Resolution Lidar

Settore Scientifico Disciplinare Fis/01

Dottorando
Changbo Song

Tutore
Dr. Xuan Wang
Prof. Nicola Spinelli

Anni 2014/2017

Contents

Abstract

Aerosol particles are an important component of the atmosphere. Most of the aerosol mass suspended in the atmosphere resides within the PBL, which is the atmospheric layer directly above the ground. Atmospheric aerosols affect air quality and, in turn, human and ecosystem well-being (WHO, 2013a), and they also play an important role in the Earth's climate system (IPCC, 2013). In fact, PM (Particles Mater) Mater) pollution is probably the most urgent issue in air quality regulation worldwide, and at the same time it represents one of the biggest sources of uncertainty in current climate simulations. Therefore, vertically resolved measurements of physical and optical properties of aerosol particles are of great interest, and height-resolved observations of these parameters can only be carried out with lidar techniques.

The lidar technique has proved to be effective to measure the vertical profile of aerosol optical properties with high vertical and temporal resolution. Spaceborne lidars are capable of mapping vertical distributions of aerosol over globe spatial regions in a short amount of time. For existing spaceborne lidars, such as Cloud-Aerosol Lidar and Infrared Pathfinder Satellite Observation (CALIPSO), an assumption of aerosol extinction-to-backscatter ratio is needed to retrieve aerosol optical properties. To measure the vertical profile of aerosol extinction without assumptions of the aerosol extinction-to-backscatter ratio, High Spectral Resolution Lidar (HSRL) technique has been employed due to the advantage of day and night measurements compared to Raman lidar.

A spectral analysis system developed for a spaceborne HSRL has been implemented and is presented in this thesis. The spectral analysis system is based on the combination of an interference filter, a planar Fabry-Perot interferometer (PFPI) background filter, and a confocal Fabry-Perot interferometer (CFPI) high spectral resolution filter. By the comparison of a molecular absorption filter and three kinds of interferometer filters, the CFPI has been adopted for the high spectral resolution filter of the spaceborne HSRL. Unlike gas absorption cells, CFPI has no problem of leak and vapor formation, which would make the gas absorption cells useless. Compared

to other interferometers, the CFPI can provide high spectral resolution and a large *étendue* simultaneously, and is much less sensitive to alignment errors and vibrations.

A frequency-locking subsystem is used to lock the center transmission wavelength of the spectral analysis system with the wavelength of the emitted laser. The developed two-stage frequency-locking technique is a novel technique and can be used whether the locking laser is a pulsed laser or a continuous laser. The frequency-locking subsystem of the spectral analysis system has been designed and realized. The tests show that it is a robust apparatus, with very good stability.

The parameter requirements of the spectral analysis system have been obtained by a simulation of the spaceborne HSRL. All the components of the spectral analysis system have been designed and realized. After being assembled, the spectral analysis system has been tested by using a narrow linewith continuous laser. The test results show that transmission and reflection at the wavelength of 532nm are close to the theoretical value, when the central wavelength of the spectral analysis system is locked to the wavelength of the laser source by the developed frequency-locking system.

The error sources that affect the accuracy of aerosol optical properties are analyzed. The results show that the detector noise is the dominant source of error. Further analysis also shows that the relative error of the retrieved aerosol and molecular signals are more sensitive to the error of the CFPI peak transmission than to the error of the CFPI bandwidth.

1 Introduction

1.1 Atmospheric aerosols

The atmosphere is a relatively thin gaseous layer surrounding the earth; 99% of the mass of the atmosphere is contained in the lowest 30km. There are five main layers within the atmosphere. They are, from top to bottom, the exosphere, the thermosphere, the mesosphere, the stratosphere, and the troposphere. Within the troposphere, the planetary boundary layer (PBL), which is the atmospheric layer directly above the ground, is a particularly important sublayer [1]. Most of the aerosol mass suspended in the atmosphere resides within the PBL, which is generally very turbulent (due to surface features, friction, wind shear and thermal convection), and strongly influenced by ground conditions. The PBL can be heated or cooled directly by the ground, and can also pick up aerosols from the ground, such as blowing dust and smoke from fires [2].

Aerosol particles affect the Earth's climate in two different ways. They scatter and absorb the solar and terrestrial radiation, and they also act as cloud condensation nuclei, thus influencing cloud properties. According to the findings of the IPCC, the current level of scientific understanding of the impact of aerosols on the global climate system is considered as medium to low. In particular, the way aerosols affect chemical and microphysical properties, as well as the reflectance of the underlying surface depends on their spatial distribution [3].

Clouds and aerosols continue to contribute to the largest uncertainty to the estimates and interpretations of the Earth's changing energy budget. Observational uncertainties of climate variables other than temperature, uncertainties in aerosols properties, and limits in understanding the main processes taking place continue to hamper a precise attribution of climate system changes. Aerosol and cloud variability at scales significantly smaller than those resolved in climate models, and the subtle responses of clouds to aerosol at those scales, imply that, for the foreseeable future, climate models will continue to rely on parameterizations of aerosol-cloud interactions that introduce subgrid variability. This implies that large uncertainties for

estimates of the forcings are associated with aerosol-cloud interactions [4].

Human activity directly affects the properties of PBL layer, and much of the atmospheric chemistry also occurs in this layer. Atmospheric aerosols affect air quality and, in turn, human and ecosystem well-being (WHO, 2013a), and also play an important role in the Earth's climate system (IPCC, 2013). From the environmental perspective, aerosol analyses are also an important issue in atmosphere and climate sciences. In fact, PM (Particles Mater) pollution is probably the most urgent issue in air quality regulation worldwide, and at the same time it represents one of the biggest sources of uncertainty in current climate simulations [5].

In summary, atmospheric aerosols play an important role in many atmospheric processes. Although only a minor constituent of the atmosphere, they have appreciable influence on the Earth's radiation budget, air quality and visibility, clouds, precipitation, and chemical processes in the troposphere and stratosphere. The physical properties, chemical composition, and corresponding complex refractive-index characteristics of the particles, as well as the resulting climate-relevant optical properties are subject to large diversity especially in the troposphere because of widely different sources and meteorological processes. Therefore, vertically resolved measurements of physical and optical properties of particles such as the particle surface area concentration, volume and mass concentrations, mean particle size, and the volume extinction coefficient are of great interest. Routine (longterm), height-resolved observations of these parameters can only be carried out with Lidar [6].

1.2 Aerosol lidar

Lidar is an acronym for light detection and ranging. In the case of lidar, a light pulse is emitted into the atmosphere. Light from the beam is scattered in all directions from molecules and particulates in the atmosphere. A portion of the light is scattered back toward the lidar system. This light is collected by a telescope and focused upon a photodetector that measures the amount of back scattered light as a function of distance from the lidar [1].

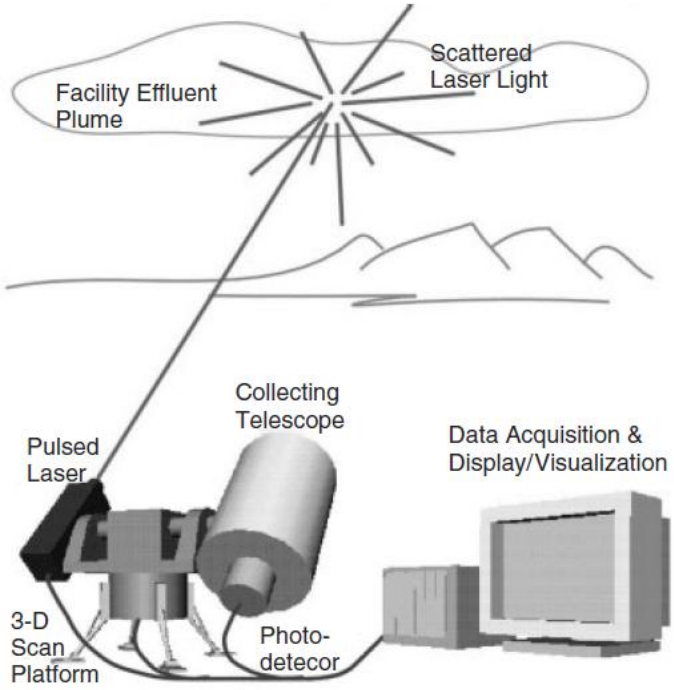

Figure 1.1 The basic setup of a lidar system.

The basic setup of a lidar system is shown in Figure 1.1. In principle, a lidar consists of a transmitter and a receiver. Short light pulses with lengths of a few to several hundred nanoseconds and specific spectral properties are generated by the laser. Many systems apply a beam expander within the transmitter unit to reduce the divergence of the light beam before it is sent out into the atmosphere. At the receiver end, a telescope collects the photons backscattered from the atmosphere. It is usually followed by an optical analyzing system which, depending on the application, selects specific wavelengths or polarization states out of the collected light. The selected radiation is directed onto a detector, where the received optical signal is converted into an electrical signal. The intensity of this signal in its dependence on the time elapsed after the transmission of the laser pulse is determined electronically and stored in a computer [6].

The first lidar instruments appeared before laser times. In the 1930's first attempts were made to measure air density profiles in the upper atmosphere by determining the scattering intensity from searchlight beams. Height information was obtained by scanning the receiver field of view of a distant telescope along the continuous light beam. In 1938, pulses of light were used for the first time to measure

cloud base heights. The rapid development of modern lidar technology started with the invention of the laser in 1960 and the giant-pulse or Q-switched laser in 1962. Fiocco and Smullin published atmospheric observations with a ruby laser in 1963. About a decade later all basic lidar techniques had been suggested and demonstrated [6].

The variety of interaction processes of the emitted radiation with the atmospheric constituents that can be used in lidar allow the determination of the basic atmospheric variables of state, i.e., temperature, pressure, humidity, and wind, as well as the measurement of trace gases, aerosols, and clouds. Lidar has largely contributed to our knowledge of the Earth's atmosphere during the past decades. It is particularly useful for the investigation of highly variable atmospheric parameters [6].

Elastic-backscatter lidars have extensively been used to investigate clouds and aerosol layers since the early 1960s when Fiocco and Grams [4] reported the first lidar-derived stratospheric aerosol profiles. Only in recent years, however, has significant progress been made toward a quantitative study of atmospheric aerosol properties solely based on lidar [6]. The atmospheric extinction coefficient rather than the backscatter coefficient is the fundamental parameter that is generally extracted from an elastic lidar signal. Unfortunately, the lidar equation contains more than one unknown value and is thus undetermined. To overcome this problem and to be able to extract the extinction coefficient from the signal, the lidar equation constant must be estimated. In addition, the relationship between backscatter and total extinction must in some way be established or assumed [1]. Klett and Fernald proposed lidar data inversions requiring assumptions of boundary extinction values, or an altitude invariant extinction to backscatter ratio [2].

Elastic-backscatter lidars detect the total atmospheric backscatter without separation of particle and molecular contributions to the backscattered signal. The main drawback of this method is that trustworthy profiles of the climate-relevant volume extinction coefficient of the particles cannot be obtained. The extinction profile must be estimated from the determined backscatter-coefficient profile. The scanning or multiangle lidar technique is a technique to derive vertical profiles of the

particle extinction coefficient. The most critical requirement here is the need for horizontally homogeneous particle backscattering and extinction at all measurement heights. This condition is often not fulfilled, at least not in the convective boundary layer [6]. An aerosol Raman lidar or a high spectral resolution lidar (HSRL) measures two signal profiles, which allow the separation of particle and molecular backscatter contributions. Using these two methods, the aerosol characteristics can be retrieved without assumptions on the aerosol extinction-to-backscatter ratio, offering both high vertical, and temporal resolution. Both Raman lidar and HSRL distinguish particle and molecular backscatter contributions by separating the backscattering spectrum. Figure 1.2 shows the various components of molecular light scattering at sequentially higher resolution [7].

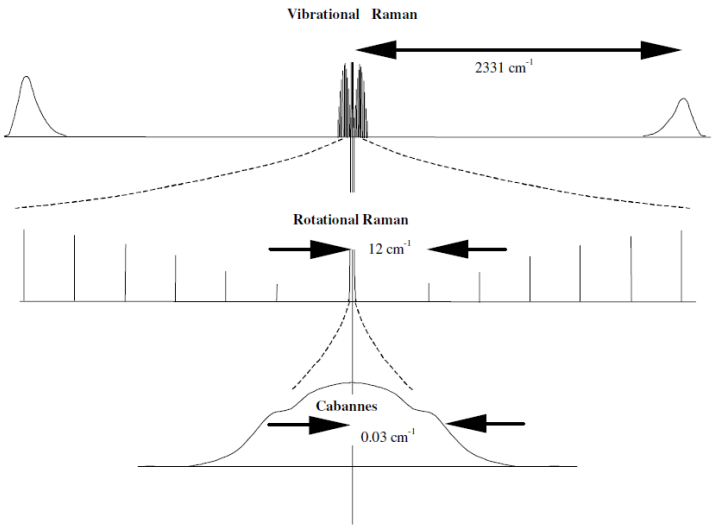

Figure 1.2 Scattering components from laser illumination of a diatomic molecular gas (e.g. nitrogen), at sequentially higher resolution.

In Figure 1.2, molecular nitrogen at 1 atm, 300 K, is used as an example. Far off resonance from the laser wavelength are the vibrational Raman bands. These are of the order of a few hundred to a few thousand wave numbers (cm−1) away (2331 cm−1 for N2). Closer to the laser lines is the rotational Raman band. The central feature is associated with elastic scattering and does not change the internal energy of the molecule. It lies closest to the laser line, and has features that reflect the translational motion.

The Raman lidar technique makes use of the weak inelastic scattering of light by

atmospheric molecules. The excitation of a variety of rotational and vibrational molecular energy levels leads to several bands of Raman scattered radiation, the frequency shifts of which are characteristic for the interacting molecule. This very robust technique makes low demands concerning spectral purity of the emitted laser light, and frequency stabilization of the receiver. However, it suffers from the low cross sections of Raman scattering, and, thus, from the comparably small signal-to-noise ratios of the measurements. The differential cross sections for Rayleigh, Cabannes, shifted rotational Raman, and total vibrational Raman scattering, excited at 532 nm, are 6.0×10^{-32}, 5.9×10^{-32}, 1.5×10^{-33}, and 5.2×10^{-35} m^2/sr, respectively. Assuming a comparable loss due to the receiving optics, we can estimate the relative signal from these cross sections for Rayleigh lidar, HSRL and Raman lidar respectively. Relative to Rayleigh scattering, the approximate cross sections of Cabannes, shifted rotational Raman scattering, and vibrational Raman scattering are 1, 0.025, and 0.001, respectively [8].

Table 1.1 Relative Signal Strength and Bandwidth Comparison between Different Scattering Lidar for Atmospheric Parameter Measurements.

Backscatter Lidar	Measured Parameters (Method)	Relative Signal Strength[a]	Receiver Bandwidth[a] Night (Day)	Comments
Mie	Aerosol and cloud	>1	5 nm (100 GHz)	Bandwidth for night (day) detection
Aerosol wind	Wind (HET or FPI)	>1	1 GHz, FSR	Filter bandwidth (resolution), ~0.1 GHz Frequency stability, 1 ms^{-1}/4 MHz
Rayleigh	Temperature (Inversion)	1	5 nm (100 GHz)	Must be aerosol free Bandwidth for night (day) detection
HSRL	Temperature (AVF; Ratio)	0.2	10 GHz	Frequency stability, 0.6 K/2 MHz Good aerosol rejection
HSRL	Aerosol and wind (AVF; Ratio)	0.4	10 GHz	Frequency stability, 1 ms^{-1}/4 MHz
Rotational Raman	Temperature (IF; Ratio)	0.005	5 nm	Filter bandwidth, ~1 nm, Frequency and filter stability, 10 GHz Filter optical density >6 at laser wavelength Daytime operation difficult
Vibrational Raman	Backscatter Extinction	0.001	3 nm (500 GHz)	No broader than 5 nm at night
Vibrational Raman	Temperature (Inversion)	0.001	5 nm (100 GHz)	Bandwidth for night (day) detection Problematic with extinction gradient
Molecular Wind	Wind and temperature (Double FPI)	0.1	10 GHz, FSR	Problematic with aerosol Filter bandwidth (resolution), ~1 GHz Frequency stability, 1 ms^{-1}/4 MHz

The Raman lidar measures lidar return signals elastically backscattered by air

molecules and particles, and inelastically (Raman) backscattered by nitrogen and/or oxygen molecules. High spectral resolution lidar (HSRL) relies on the differences in spectral distribution of light elastically backscattered by particles and air molecules. In Table 1.1, the strength of Raman signals is a factor of 80 (rotational Raman lines) to 400 (vibration-rotational Raman lines) lower than the one of HSRL signals (Aerosol and wind). So, while the HSRL lidar is operational at day and night, the Raman lidar is mainly used during nighttime, i.e., in the absence of the strong daylight sky background. Compared to Raman lidar, HSRL has the advantage of day and night measurements, so more suitable for satellite platforms.

1.3 High spectral resolution lidar (HSRL)

Due to the random thermal motion (～300 m/s) of air molecules, light that has been scattered by air molecules experiences a significant Doppler frequency shift. In contrast, aerosols, cloud particles, and other particulate matter move with velocities determined by wind (～10 m/s), or turbulence (～1 m/s), which only produce small Doppler shifts. As a result, the frequency distribution of light backscattered from the atmosphere consists of a narrow spike near the frequency of the laser transmitter, caused by particulate scattering, protruding out a much broader distribution produced by molecular scattering [6].

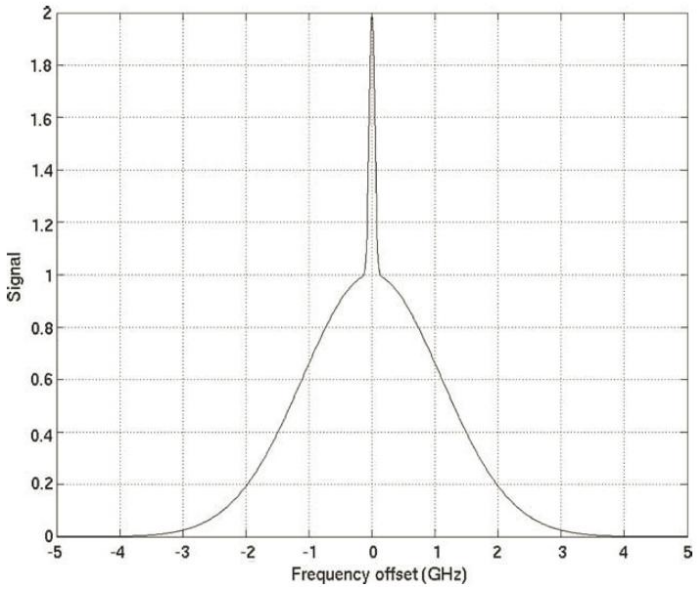

Figure 1.3 Spectral profile of backscattering from a mixture of molecules and aerosols for a temperature of 300 K. The spectral width of the narrow aerosol return is normally

determined by the line width of the transmitting laser.

High spectral resolution lidars utilize optical filters to distinguish between photons scattered from molecules and those scattered by aerosol or cloud particles. Very narrow bandwidth filters are required (～1 GHz). In addition, the transmitted laser frequency must be locked to the filter center frequency, and the linewidth must be smaller than the filter width (～100 MHz). These requirements make HSRLs more difficult to implement than Raman lidars. However, a HSRL provides much larger molecular signals, and can utilize very narrow bandwidths to block solar noise [6].

The HSRL technique was first discussed by Schweisow and Lading (1981), and demonstrated by Shipley et. al. (1983), who originally used a Fabry Perot etalon as the narrow band filter. Shimizu, Lee and She (1983) suggested the use of an atomic absorption filter in an HSRL, and She, Alvarez, Caldwell, and Krueger (1992) demonstrated a HSRL using a barium vapor filter to separate Mie and Rayleigh lidar returns. Piironen and Eloranta (1994) used an iodine atomic absorption filter in an HSRL, which had the added advantage of an absorption line almost resonant with a Nd:YAG laser wavelength [9]. In the last decade, several HSRLs have been developed, or are being developed. A ground HSRL has been built at Montana State University [2] and an airborne HSRL has been used to measure aerosol optical properties by Langley Research Center, NASA [10].

The HSRL device designed and constructed at Montana State University utilizes a confocal Fabry-Perot interferometer (CFP) to separate lidar returns from atmospheric aerosols and molecules. This HSRL transmits the fundamental and second harmonic output from an injection seeded Nd:YAG laser, and collects the backscattered return using a Schmidt-Cassegrain telescope. In the receiver, the 532 nm return is optically separated from the 1064nm return with a beam splitter. The 1064 return is then directed through a filter, and onto an avalanche photodiode. The 532 nm return is transmitted through the beam splitter, and coupled into a multi-mode optical fiber. The fiber output is coupled with a modulated 1064 nm beam produced by a 1064 nm cw seed laser. This combined beam is incident on a CFP filter. The CFP

is frequency-locked to the 1064 nm cw seed laser, and is simultaneously resonant with the first harmonic 532 nm wavelength [2]. The 532nm light backscattered by the aerosol is transmitted, while the Doppler broadened molecular signal is rejected.

NASA Langley Research Center has developed two such systems, named HSRL-1 and HSRL-2. HSRL-1 is the first airborne High Spectral Resolution Lidar instrument built and operated by NASA Langley. HSRL-1 employs the HSRL technique at 532 nm, and the standard backscatter technique at 1064 nm. It also measures depolarization at both wavelengths. The instrument is internally calibrated at 532 nm for measurements of aerosol/cloud backscatter and extinction, and at both 532 and 1064 nm for measurements of depolarization. Discrimination between aerosol/cloud and molecular returns in the HSRL-1 receiver is accomplished by splitting the returned signal into two optical channels: the molecular backscatter channel, which is equipped with an extremely narrowband iodine vapor (I_2) absorption filter to eliminate the aerosol returns and pass the wings of the molecular spectrum, and the total backscatter channel, which passes all frequencies of the returned signal. After appropriate internal calibration of the sensitivities of the two channels, the signals are used to derive profiles of extinction, backscatter coefficient, and extinction-to-backscatter ratio [10][11].

HSRL-2 is the second-generation airborne HSRL developed at the NASA Langley Research Center. It is an airborne prototype for the lidar on the future Aerosol-Cloud-Ecosystem (ACE) mission, recommended for implementation by NASA in the National Research Council's Decadal Survey for Earth Science. HSRL-2, with additional HSRL capability at 355 nm, is the first airborne system capable of providing $3\beta+2\alpha$ data. This contribution aims at showing the results of microphysical particle properties that can be obtained from this instrument. HSRL-2 operates at laser wavelengths of 355, 532, and 1064 nm. HSRL-2 measures profiles of particle backscatter coefficients, and linear particle depolarization ratios at 355, 532, and 1064 nm, and particle volume extinction coefficients at 355 and 532 nm. The extinction and backscatter coefficients at 355 and 532 nm are derived using the HSRL technique. An iodine-vapor filter is used for the extinction-coefficient measurements

at 532 nm. The new feature of HSRL-2 compared to HSRL-1 is that it measures the particle volume extinction coefficient not only at 532 nm, but also at 355 nm, using an interferometric technique [12]. A compact, robust, quasi-monolithic, tilted, field-widened Michelson interferometer (MI) is under development as the spectral discrimination filter for a second-generation HSRL (HSRL-2) at National Aeronautics and Space Administration (NASA) Langley Research Center (LaRC) [13].

In conclusion, there are two kinds of High Spectral Resolution filters that have been used in high spectral resolution lidars. They are atomic and molecular absorption filters, and interferometer filters, respectively. The interferometer filters include the Planar Fabry–Perot interferometer, the confocal Fabry–Perot interferometer, and the wide-angle Michelson interferometer.

Atomic and molecular absorption filters avoid the acceptance angle limitations of a Fabry-Perot. This makes iodine absorption cells a popular choice for separating molecular and aerosol returns in HSRL instruments. The key disadvantage of using gas absorption cells in HSRL instruments is that they severely limit the possible wavelengths at which the HSRL can be operated [2]. When using a molecular absorption filter, HSRL detector configuration is shown as Figure 1.4.

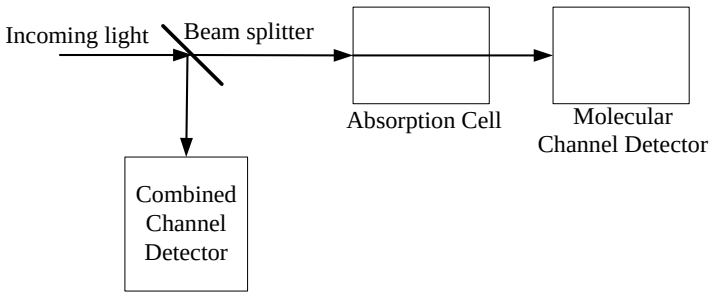

Figure 1.4 HSRL detector configuration when using a molecular absorption filter.

Discrimination between aerosol/cloud and molecular returns in the NASA Langley Research Center airborne HSRL receiver is accomplished by splitting the returned signal into two optical channels: the molecular backscatter channel, which is equipped with an extremely narrowband iodine vapor (I_2) absorption filter to eliminate the aerosol returns while passing the wings of the molecular spectrum (see Figure 1.5), and the total backscatter channel, which passes all frequencies of the

returned signal [10].

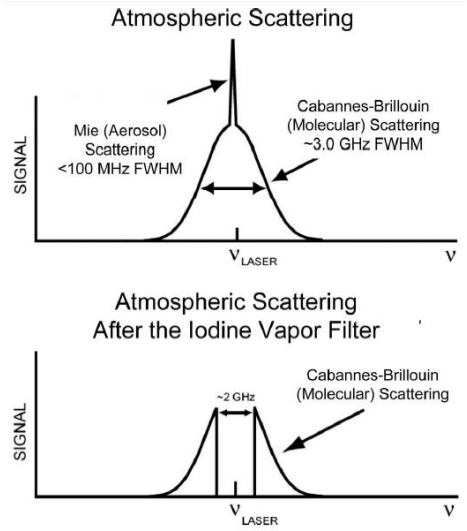

Figure 1.5 Schematic diagram for a HSRL return spectra before and after the Iodine Vapor Filter.

The interferometer filters are another way to separate the backscattering spectra due to the interaction of emitted laser light with atmospheric molecules or aerosols. According to the literature [14][15], a Fabry-Perot interferometer filter centred on the central wavelength of backscattering light (355nm) is depicted on Figure 1.6. The Mie contribution backscattered by aerosols is transmitted by the interferometer filter, while the wide broadening Rayleigh contribution backscattered by atmospheric molecules is reflected.

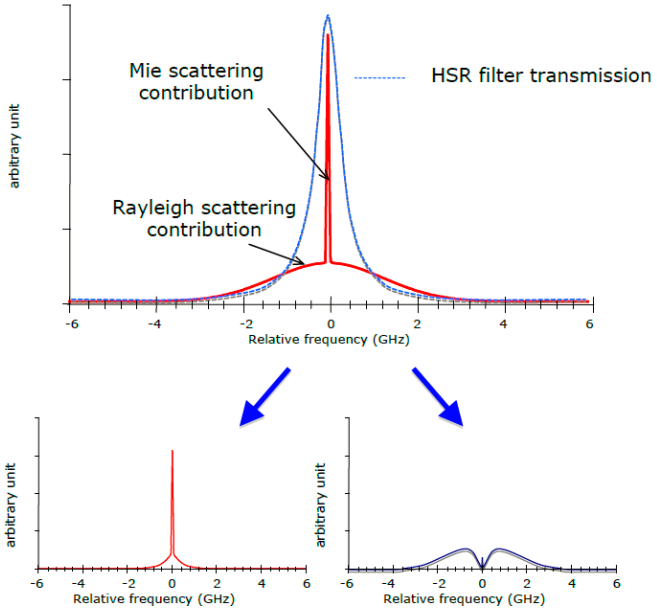

Figure 1.6 Mie / Rayleigh scattering contributions separation principle based on

interferometers. The red line represents the backscattering spectrum scattered by atmospheric aerosols and molecules at the central wavelength of 355nm. The blue dash line represents the transmission of the interferometer filter. The bottom left figure is the transmitted spectrum and the bottom right figure is the reflected spectrum.

1.4 Spaceborne HSRL

The evolution of lidar, from the early ground-based measurements to first long-duration spaceborne experiments, goes from the first, ground-based, lidars in the 1960s to the first flown systems on small aircraft in 1969, eventually followed in the late 1970s by lidars flown on large aircraft capable of long-range measurements. Starting from 1979, flights aboard high-altitude aircrafts were accomplished, and data were taken at approximately 20 km of altitude. The aerosol and cloud lidars continued their measurement campaigns aboard aircraft into the 1980s, 1990s, and up to the present, improving their capabilities, as new technologies became available. Multiple wavelengths and polarization measurement techniques were incorporated. Higher repetition rates and more efficient lasers, as well as improved and faster data capture and storage devices, helped in greatly expanding airborne lidar applications. The airborne aerosol and cloud lidars circled the globe, mapping stratospheric volcanic layers, Saharan dust, stratospheric aerosols, and polar stratospheric clouds (PSC)s, as an example.

Compared to ground and airborne lidars, spaceborne lidars are capable of mapping vertical distributions of aerosol over globe spatial regions in a short amount of time.

Lidar In-space Technology Experiment (LITE) was the first payload aboard the Space Shuttle Discovery flight STS-64 launched from NASA's Kennedy Space Center on September 9, 1994. LITE employed a three-wavelength Nd:YAG laser transmitter, a 1 m diameter telescope receiver with photomultipliers (PMTs) for the 355 nm and 532 nm channels, and an avalanche photodiode (APD) for the 1064 nm channel. A two-laser, 10 Hz flashlamp pumped design was incorporated for redundancy [6].

The first long-duration spaceborne lidar is the Geoscience Laser Altimeter

System (GLAS). GLAS is a facility instrument designed to measure ice-sheet topography and associated temporal changes, as well as cloud and atmospheric properties. GLAS is carried on the Ice, Cloud and land Elevation Satellite (ICESat), which launched 13 January 2003 at 00:45 UTC from Vandenberg Air Force Base in California. GLAS incorporates a diode-pumped Nd:YAG laser to make surface topography measurements at 1064 nm. The measurement of aerosols and other atmospheric characteristics is accomplished at the 532 nm wavelength. The return signal is collected using a 1-meter-diameter telescope. The laser transmits forty 5-ns pulses per second at the nadir, producing 70-m-diameter spots at the surface, separated by 175 meters [6].

The Cloud-Aerosol Lidar and Infrared Pathfinder Satellite Observations (CALIPSO) mission was developed to provide global profiling measurements of clouds and aerosol distributions and properties, to complement current measurements and improve our understanding of weather and climate. CALIOP, the primary instrument carried by CALIPSO satellite, which was launched on April 28, 2006, is the first satellite lidar optimized for aerosol and cloud measurements, and is also the first polarization lidar in space. CALIOP is based on a Nd:YAG laser operating at 1064 nm and 532 nm. The output laser beam is linearly polarized, and two polarization-sensitive, 532 nm receiver channels provide measurements of the degree of linear polarization of the return signal. Using the two 532 nm receiver channels, and a channel measuring the total 1064 nm return signal, CALIOP measures the detailed vertical distribution of aerosols and clouds along with their microphysical and optical properties [16].

As a standard elastic backscatter lidar operating at 532 and 1064 nm, CALIOP cannot provide direct measurement of aerosol optical properties profiles. This makes it unavailable for an accurate classification of aerosols. Spaceborne HSRL is one of the ways to solve this problem. Several spaceborne HSRLs are under development.

The ADM-Aeolus mission aims at improving the understanding of atmospheric dynamics, global atmospheric transport and global cycling of energy, water, aerosols and chemicals in the atmosphere. The ADM-Aeolus payload Atmospheric Laser

Doppler Instrument (ALADIN) is based on a direct-detection, Doppler wind lidar operating at 355 nm. The receiver consists of two spectrometers to determine the Doppler shift from the spectrally broad Rayleigh molecular return, and the spectrally narrow Mie return from aerosols and clouds. ALADIN will be the first wind lidar and the first high-spectral resolution lidar (HSRL) in space [17].

The Cloud-Aerosol Transport System (CATS) is a lidar remote sensing instrument that provides range-resolved profile measurements of atmospheric aerosols and clouds. The instrument is located on the Japanese Experiment Module – Exposed Facility (JEM-EF) on the International Space Station (ISS). The CATS payload is designed to provide a combination of long-term operational science, in-space technology demonstration, and technology risk reduction for future Earth Science missions. CATS operates in three different modes. One of these modes is the demonstration of HSRL aerosol measurements. This mode was designed to use the injection-seeded laser operating at 1064 and 532 nm to demonstrate a high spectral resolution measurement using the 532 nm wavelength. The heart of the CATS HSRL detector box is an etalon that provides the spectral resolution needed for the HSRL measurement. Backscattered light collected by the telescope is passed through the etalon, and an image of the etalon fringe pattern is created. A bandpass filter is used in tandem with the etalon to reject background sunlight, permitting daytime operation. The optical gap of the etalon is 3 cm with a plate reflectivity of 90%. It is critical to maintain the symmetry and shape of the etalon fringe pattern to avoid uncertainty in the measurement. A digital etalon controller was developed by Michigan Aerospace Corporation in which piezoelectric actuators control the etalon electronics to position and maintain the plate parallelism. A holographic circle-to-point converter optics is placed in the focal plane of the HSRL receiver to provide the spectral detection. The circle-to-point converter simplifies hardware requirements, improves efficiency of measuring the spectral content in the fringe pattern, and allows CATS to utilize photon-counting detection. The holographic optics is coupled to the 10 individual 532 nm detectors, each representing a small wavelength interval [18].

EarthCARE aims to the determination of cloud and aerosol occurrence, structure,

and physical properties, together with measurements of solar and thermal radiation at a global scale. The EarthCARE satellite shall achieve its mission through the operation, individual and in synergy, of its four instruments: ATLID, the CPR, the Multi-Spectral Imager (MSI), and the Broad-Band Radiometer (BBR). ATLID is a backscatter LIDAR instrument that uses the fact that interaction of light with molecules and aerosols leads to different spectra scattering effects. The receiver optics goes from the telescope output to the detector fiber entrances. It includes the entrance filtering optics (narrow interference filters with less than 1 nm bandwidth), the blocking filtering optics (spatial filtering with a field-stop delimiting the 65 μrad field-of-view), and two spectral filtering units: the background Fabry-Perot etalon used to finely filter the Earth background light, and the High Spectral Resolution filter (combining an optical prism assembly for the channels separation and a high resolution Fabry-Perot etalon) [19].

In these developing spaceborne HSRLs, different interferometers are used as high spectral resolution filters to separate the received light backscattered by aerosols and molecules. Compared to atomic or molecular absorption filters, the interferometers have several advantages. First, gas absorption cells in HSRL instruments can just be operate at several possible wavelengths, while the interferometers does not have this limit. Second, interferometers have no problem of leak and vapor formation, which make the gas absorption cells useless. So interferometers are more suitable for satellite application.

1.5 Goals and Contributions

HSRL technique accurately measures the vertical profile of aerosol extinction without assumptions of the aerosol extinction-to-backscatter ratio by separating the Mie scattering signal and Rayleigh scattering signal. This makes HSRL very difficult to develop and a high spectral resolution analysis system is required.

The goal of this dissertation is to develop a prototype of a spectral analysis system for a spaceborne high spectral resolution lidar in the framework of a China-Italy international cooperation project LISA (LIdar for Space study of the Atmosphere). The goal of LISA project is to develop a prototype of spaceborne HSRL.

The spaceborne HSRL uses a dual-wavelength laser (1064nm and 532nm) to detect aerosol, and has high spectral resolution ability at 532nm.

For the spaceborne HSRL, there are three difficulties: firstly, the laser source should have narrow bandwidth, high energy, and small drift of the center wavelength; secondly, the receiver should have the ability of less than 1 pm spectral resolution to separate aerosol backscattering signal and molecular backscattering signal; thirdly, the receiver must be locked to laser source with a spectral accuracy of tens of MHz.

The spectral analysis system presented in this thesis involves the last two difficulties, including a combination of interferometer filters and a frequency-locking subsystem. Contributions of this research include:

a) A comparison of spectral analysis systems for spaceborne HSRL;
b) An analysis of the spectral requirements of the spectral analysis system for spaceborne HSRL;
c) A design of the spectral analysis system for spaceborne HSRL;
d) An analysis and design of the mode matching unit;
e) An analysis and design of the frequency locking subsystem;
f) Test of the frequency-locking subsystem;
g) Test of the spectral analysis system for spaceborne HSRL;
h) An error analysis for the spectral analysis system.

2 The comparison of spectral analysis systems for the spaceborne HSRL

2.1 The requirements of the spectral analysis system for the spaceborne HSRL

Spaceborne HSRL systems use a narrow bandwidth filter to spectrally separate aerosol backscattering signal and Doppler broadened molecular backscattering signal. The crosstalk between aerosol channel and molecular channel, and the signal to noise ratio (SNR) in these two channels will affect the measurement accuracy. However, crosstalk and SNR depend on the spectral resolving power, and light gathering power of the narrow bandwidth filter. The spectral analysis system needs to meet the requirements of the spectral resolving power and light gathering power at the same time. In general, the situation of an interferometer as a filter is shown in Figure 2.1

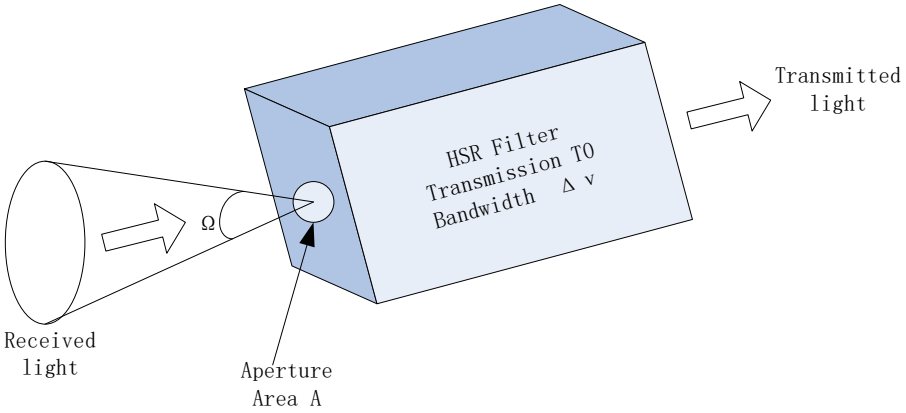

Figure 2.1 Generalized picture of a interferometer as a filter

Here, the interferometer is depicted as a bandpass filter: all of the radiation emanating from within a solid angle Ω subtended at an aperture of area A, can be transmitted within the bandpass of the interferometer. If the transmission of the interferometer at the center of the bandpass is T_0, then the radiant power per unit bandwidth transmitted by the interferometer is given by:

$$P_\nu = N_\nu A\Omega T_0$$

where, the product $A\Omega$ has come to be known as *étendue U* of the interferometer.

The basic parameters of the spaceborne HSRL are shown in Table 2.1.

Table 2.1 The main parameters of the spaceborne HSRL.

NO.	Name of parameters	Value of parameters

1	Laser wavelength	532nm
2	Laser pulse energy	110mJ
3	Pulse repetition frequency	20Hz
4	Diameter of telescope	1m
5	Field of view	200 μrad

The laser has been designed and realized by Bright Solutions Srl. In order to improve the stability in space application, a 1064nm 1kHz pulse seed laser has been used. After a two-step amplifier, and a second harmonic generator, a dual-wavelength (1064nm and 532nm), 20Hz, high energy laser has been obtained.

Due to the large field of view telescope and pulse seed laser, the requirements of the spectral analysis system are as follows:

1) The spectral analysis system has to gather the light power received by the telescope with the diameter of 1m and the field of view 200 μrad. At the same time, the spectral resolution of the spectral analysis system should reach about 1GHz.
2) The frequency-locking subsystem has to use the pulse seed laser to lock the spectral analysis system with the 20Hz, 532nm light. This is a novel requirement, which is different with the requirement of the HSRLs using continuous seed laser.

Both these two requirements bring more difficulties than the previous spaceborne HSRLs. The parameters of the telescopes and the types of the spectral analysis system in the mentioned spaceborne HSRLs [17][18][19], are shown in Table 2.2

Table 2.2 The parameters of the developing spaceborne HSRLs

Spaceborne HSRL	Diameter of Telescope (m)	Field of View (μrad)	Types of the spectral analysis system
CATS	0.6	110	Tunable piezoelectric controlled etalon and Holographic circle-to-point converter
ALADIN	1.5	19	Double-edge Fabry–Perot interferometer, Fringe-imaging Fizeau interferometer

ATLID	0.62	65	Background Fabry- Perot etalon and high resolution Fabry–Perot etalon

All the spaceborne HSRLs shown in Table 2.2 use the planar Fabry-Perot interferometer due to the requirement of a small *étendue*. Compared with this spaceborne HSRLs, the *étendue* requirement of LISA spaceborne HSRL is much bigger. There are also other two potential interferometers which can be used on a satellite platform. They are wide-angle Michelson interferometer (WAMI) [13] and Confocal Fabry–Perot Interferometer (CFPI) [2]. The comparison of these three interferometers will be performed in the next section.

2.2 Comparison of spectral analysis systems for space application

There are three kind of interferometer filters which are introduced above and can be used in HSRL. They are planar Fabry–Perot interferometer, confocal Fabry–Perot interferometer (sometimes called a spherical Fabry–Perot interferometer (SFPI)) and wide-angle Michelson interferometer (WAMI). Martha Wallis Dawsey had compared SFPI with WAMI in his thesis [9]. The criteria for the comparative analysis include the spectral, angular, and efficiency. The results show that: in all cases, the SFPI has a higher resolving power (RP) by two orders of magnitude. A narrow band filter with a very high RP can precisely eliminate the aerosol (Mie) scatter from the total lidar return, with minimal losses to the Rayleigh signal. Both the WAMI and the SFPI have a large acceptance angle. WAMI will maintain a relatively high transmission for the entire range of acceptance angles, and can be designed to have an even larger acceptance angle, if required. SFPI and WAMI have the same order of magnitude of the acceptance angle, and theoretically WAMI can collect a little more energy than the SFPI. The transmission is dependent on laser wavelength. WAMI has higher transmission in 355 nm wavelength and SFPI has higher transmission in 532 nm wavelength. For 532 nm spaceborne HSRL, SFPI has higher resolving power and transmission compared to WAMI.

Spaceborne HSRL systems use a narrow band filter to spectrally separate Doppler broadened aerosol and molecular back-scattered return signals. The crosstalk between

these aerosol channel and molecular channel and the signal to noise (SNR) in these two channels will affect the measurement accuracy. However, crosstalk and SNR depend on the spectral resolving power and light gathering power of the narrow band filter. Here planar Fabry–Perot interferometer (PFPI) and confocal Fabry–Perot interferometer (CFPI) will be compared by spectral resolving power and light gathering power. From above introduction, the *product* of the resolving power and *étendue* for PFPI is [20]

$$(U\mathcal{R})_{\mathrm{PFPI}} = U \cdot \frac{\nu}{\Delta\nu} = \pi \frac{D^2}{4} \frac{\lambda}{d \cdot F^*} \frac{2dF^*}{\lambda} = \pi \frac{D^2}{2} \tag{2.1}$$

where *D* is the plate diameter of PFPI. From the above formula, the product is only dependent on the diameter of the PFPI and regardless of the gap between the two PFPI mirrors. Figure 2.2 shows the relations between the *étendue*, resolving power and the diameter of PFPI.

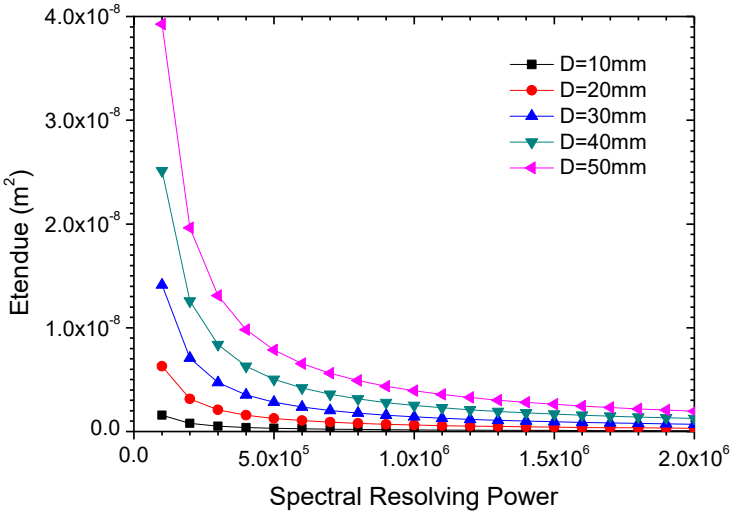

Figure 2.2 The relations between the *étendue*, resolving power and the diameter of PFPI.

However, the product of the resolving power and *étendue* for CFPI is [20]

$$(U\mathcal{R})_{\mathrm{CFPI}} = \mathrm{U} \cdot \frac{\nu}{\Delta\nu} = \frac{\pi^2 r\lambda}{F^*} \frac{4rF^*}{\lambda} = 4\pi^2 r^2 \tag{2.2}$$

where *r* is the mirror separation of the CFPI. This formula shows that the product of the resolving power and *étendue* for CFPI is only dependent on the distance between two CFPI mirrors without regard of the diameter of the CFPI. The relations between the *étendue*, resolving power and the diameter of CFPI are as follows.

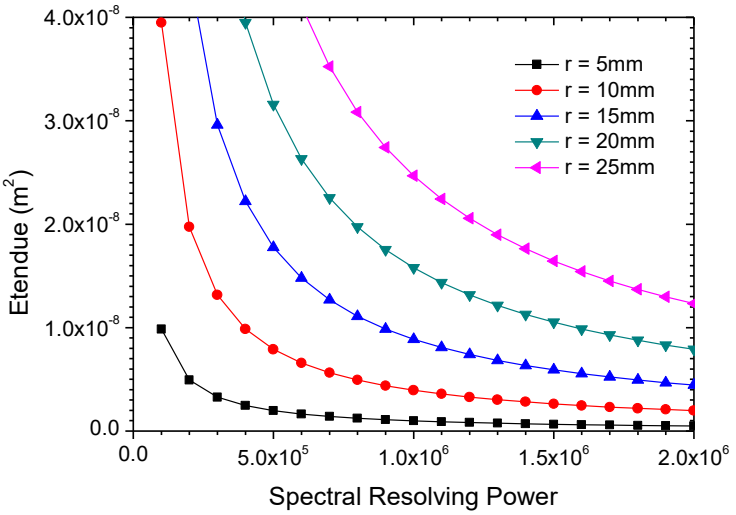

Figure 2.3 The relations between the *étendue*, resolving power and the diameter of CFPI.

Figure 2.2 and Figure 2.3 show that if the mirror separation *r* of CFPI is larger than 10 mm, the *étendue* of CFPI will be larger than the *étendue* of PFPI on all the spectral resolving powers. Due to the regardless of mirror separation *d*, PFPI will have larger *étendue* when the mirror separations of PFPI and CFPI are very small.

For our future spaceborne HSRL, the diameter of telescope will be 1 meter and the received angle will be 200 μrad. The solid angle subtended by the telescope is $\Omega_T=(2\pi[1-\cos(\theta_T)])$, where θ_T is the angular field-of-view of the telescope [9]. When θ_T is a small angle,

$$\Omega_T = \pi \sin^2(\theta_T/2) \approx \pi(\theta_T/2)^2 \tag{2.3}$$

This means that the *étendue* U of the receiver should be larger than $A_T\Omega_T = \pi\left(\frac{D}{2}\right)^2 \cdot \pi\left(\frac{\theta_T}{2}\right)^2$ =2.47E-8m^{2}sr.

Because the bandwidth (FWHM) of molecular scattering signal is about 3GHz and the bandwidth of aerosol scattering signal is dependent on the linewidth of laser transmitter (usually less than 100 MHz). Very narrow bandwidth filters are required (～1 GHz) [6]. For 532 nm wavelength HSRL, the comparison of *étendue* between PFPI and CFPI on 5.64×10^5 (FWHM = 1 GHz) resolving power is as follows.

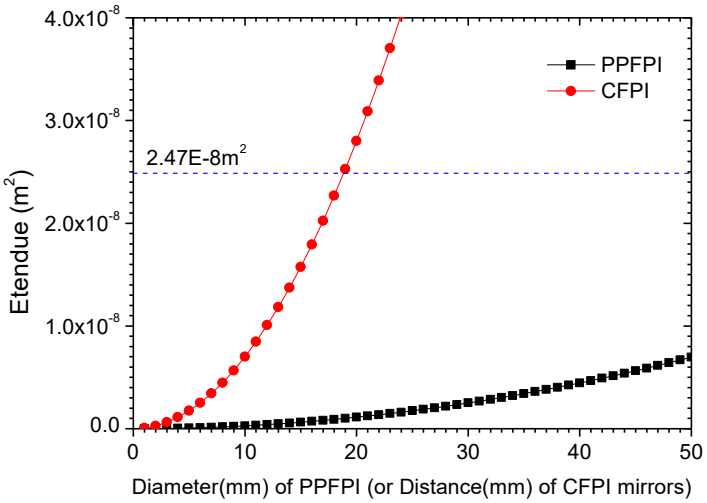

Figure 2.4 The comparison of *étendue* between PFPI and CFPI on 5.64×10^5 resolving power.

Figure 2.4 shows that PFPI can't satisfy the requirement of *étendue* even if the diameter equals to 50 mm. But the CFPI can satisfy the requirement of *étendue* when the distance is larger than 11 mm. So CFPI is adopted to separate the molecular backscattering light and aerosol backscattering light in our spaceborne HSRL.

3 Analysis and design of the spectral analysis system based on confocal Fabry–Perot interferometer (CFPI)

The principle of a spaceborne HSRL and it's spectral analysis system is shown in Figure 3.1

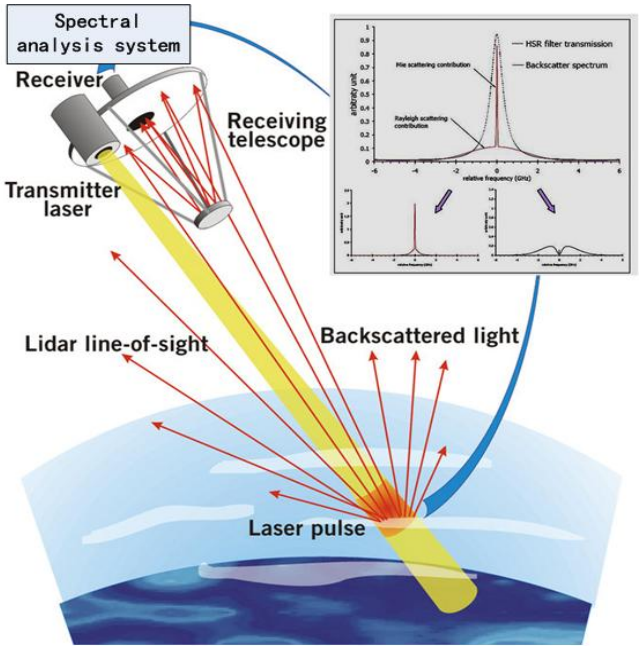

Figure 3.1 The principle of a spaceborne HSRL and it's spectral analysis system.

According to the analysis in chapter 2, confocal Fabry–Perot interferometer (CFPI) has been adopted as the narrow-band optical filter to separate backscattering light. But the distance r of the two CFPI mirrors should be larger than 11mm when the *étendue* of spaceborne HSRL is satisfied. According to the multi-mode free spectral range of CFPI [2]

$$FSR_{CFPI,multi\text{-}mode} = c/4r \tag{3.1}$$

where, c is the speed of light. So the $FSR_{CFPI,multi\text{-}mode}$ of selected CFPI should be less than 6.8GHz. But it is impossible to find an interference filter with 6.8GHz bandwidth. Another filter should be used to transfer the bandwidth of the interference filter (～0.2nm) to less than 6.8GHz bandwidth. According to the analysis in chapter 2, planar Fabry–Perot interferometer (PFPI) can do this. So the spaceborne HSRL introduced in this thesis combines an interference filter, a PFPI and a CFPI to separate the received light backscattered by atmospheric aerosol and molecules. The schematic diagram of the spaceborne HSRL is shown in Figure 3.2.

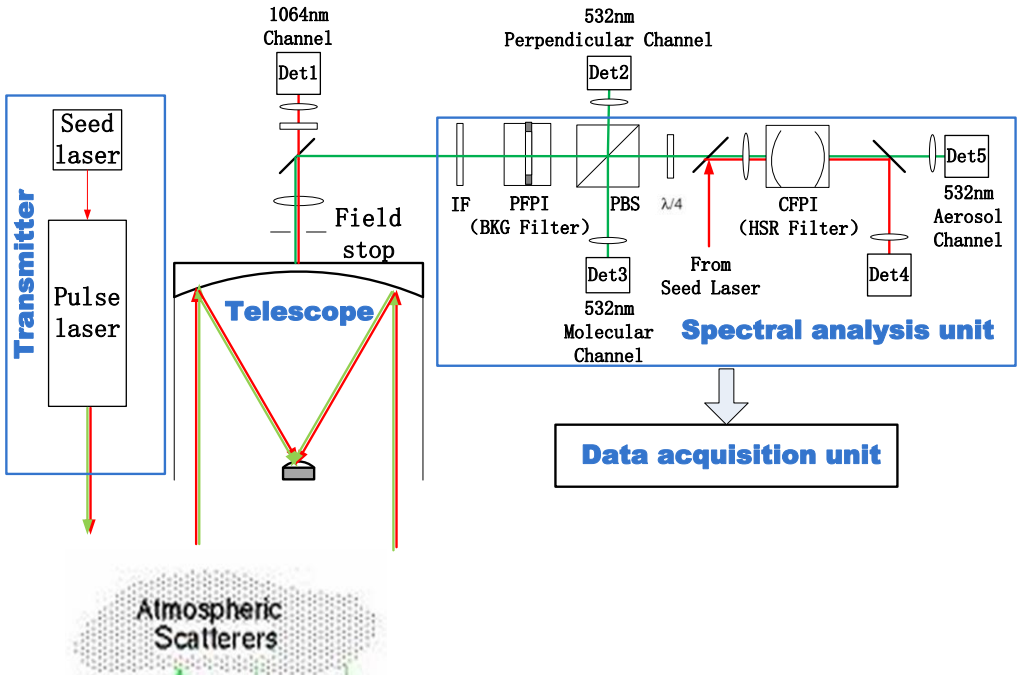

Figure 3.2 Schematic diagram of high spectral resolution lidar.

Figure 3.2 shows that a narrow linewidth laser beam with the wavelength of 1064nm and 532nm is emitted to the atmosphere and a telescope receives the backscattering light scattered by atmospheric molecules and aerosols. After the telescope, light is separated to two beams by a dichroic mirror. The IR beam with 1064nm wavelength is detected by a normal way and the HSRL technique is applied to 532 nm wavelength signal. The 532nm backscatter signal is firstly split to two polarization channels, and then the parallel channel is separated to aerosol channel and molecular channel by a CFPI filter. A frequency-locking subsystem is used to lock the center wavelength of the receiver with the wavelength of the laser source.

Three kinds of measurement results can be achieved by the spaceborne HSRL. Firstly, aerosol backscatter coefficients and extinction coefficients can be directly retrieved without the assumption of lidar ratio. The molecular channel is used to retrieve the profile of extinction coefficients and both molecular and aerosol channels are used to retrieve the profile of aerosol backscatter coefficients. Secondly, aerosol linear depolarization ratio of 532nm wavelength can be retrieved by combining all 532nm channels. Thirdly, by combining 1064nm channel and 532nm channels, color index can be obtained. All these measured parameters can be used to obtain aerosol

concentrations and distinguish aerosol types.

This thesis is focused on the spectral analysis system of the spaceborne HSRL. The spectral analysis system includes two 532nm high spectral resolution channels (molecular channel and aerosol channel) and a 1064nm frequency-locking subsystem.

3.1 The basic theory of high spectral resolution lidar

3.1.1 The spectrum distribution of the light backscattered by atmosphere

Molecular Doppler broadening spectrum

Due to the random thermal motion (～300m/s) of the air molecules, the light that has been scattered by air molecules experiences a significant Doppler frequency shift. In contrast, aerosols, cloud particles, and other particulate matter move with velocities determined by the wind (～10m/s) and turbulence (～1m/s) only produces a small Doppler shift [6]. This Doppler broadening due to thermal motion of air molecules is given by the following function [21],

$$W(\lambda) = \frac{1}{\sqrt{2\pi\sigma_R^{\,2}}} \mathrm{e}^{-\frac{\lambda^2}{2\sigma_R^{\,2}}} \tag{3.2}$$

where, σ_R (m) is the standard deviation of the Rayleigh spectrum and is given by:

$$\sigma_R = \frac{2\lambda_L}{c}\sqrt{\frac{kTN_A}{m_{air}}} \tag{3.3}$$

where, m_{air} is the molecular air mass (2.9×10^{-2} kg/mol), λ_L is the wavelength of the laser, k is the Boltzmann constant (1.38×10^{-23} J/K), c is the speed of light, and N_A is the Avogadro constant (6.023×10^{23} mol^{-1}).

In the above formula, the Brillouin effect is neglected. Numerical model (Tenti S6 model) is currently the best model for describing Rayleigh–Brillouin spectra in air. Alternative analytical model for describing spontaneous Rayleigh–Brillouin spectra in air at atmospheric conditions have been also introduced [22]. The Rayleigh–Brillouin spectrum $W_m(x,y)$ is normalized to unity integrated intensity and can be written as

$$\mathrm{w_m}(x,y)=\frac{1}{\sqrt{2\pi}\sigma_R}A\exp\left[-\frac{1}{2}\left(\frac{x}{\sigma_R}\right)^2\right]+\frac{1-A}{2\sqrt{2\pi}\sigma_B}\exp\left[-\frac{1}{2}\left(\frac{x+x_B}{\sigma_B}\right)^2\right]+\frac{1-A}{2\sqrt{2\pi}\sigma_B}\exp\left[-\frac{1}{2}\left(\frac{x-x_B}{\sigma_B}\right)^2\right] \tag{3.4}$$

where, the two non-dimensional parameters x and y are expressed as following functions

$$x=\frac{\omega}{\sqrt{2}kv_0},\ y=\frac{nk_BT}{\sqrt{2}kv_0\eta}=\frac{p}{\sqrt{2}kv_0\eta} \tag{3.5}$$

where, ω is the angular frequency shift between scattered and incident light, n is the number density, p and T are the gas pressure and temperature, respectively, η is the shear viscosity, $k=k_s-k_0=4\pi/\lambda\sin(\theta/2)$ is the magnitude of the interacting wave vector (k_0 and k_s are the wave vectors of the incident and scattered light, respectively), λ is the wavelength of the incident light, θ is the scattering angle, and $v_0=(k_BT/m)^{(1/2)}$ is the thermal velocity (k_B is the Boltzmann constant and m is the molecular mass).

The spectra are fitted with Tenti spectra in a least square fit procedure to find the best fit values for A, σ_R, σ_B, and x_B. And the result is

$$A(y)=0.18526\cdot\exp[-1.31255y]+0.07103\cdot\exp[-18.26117y]+0.74421, \tag{3.6}$$

$$\sigma_R(y)=0.70813-0.16366y^2+0.19132y^3-0.07217y^4, \tag{3.7}$$

$$\sigma_B(y)=0.07845\cdot\exp[-4.88663y]+0.80400\cdot\exp[-0.15003y]-0.45142, \tag{3.8}$$

$$x_B(y)=0.80893-0.30208\cdot0.10898^y \tag{3.9}$$

Aerosol Doppler broadening spectrum

Unlike the broad Rayleigh spectrum, the spectral width of the Mie backscatter signal is very close to the transmitted laser spectrum, due to the fact that the thermal motion of aerosols is much smaller compared to that of molecules, because of their size and mass. Due to the relative motion between spaceborne lidar and atmosphere

aerosol, Doppler frequency shift and frequency broadening will occur. According to the relativistic Doppler effect, the observer and the source are moving away from each other with a relative velocity *v*, at an angle θ_s related to the direction from the source to the observer, the corresponding observed frequency is

$$f_o = \gamma(1 - \frac{v\cos\theta_s}{c})f_s \tag{3.10}$$

where f_s is the frequency of the wave the source emitted and *c* is the speed of light. γ is defined as follows

$$\gamma = \frac{1}{\sqrt{1 - v^2/c^2}} \tag{3.11}$$

when $\theta_s = \pi/2$, the transverse Doppler frequency shift is

$$\Delta f = (\gamma - 1)f_s = (\frac{1}{\sqrt{1 - \frac{v^2}{c^2}}} - 1)\frac{c}{\lambda} \tag{3.12}$$

where λ is the wavelength of the wave the source emitted.

For the longitudinal Doppler effect, the Doppler frequency shift is from the pointing angle of satellite and the speed of wind. And the Doppler frequency broadening is from pointing stability of satellite and turbulence of wind speed. Here, a Gaussian distribution is used to describe the speed distribution, and the standard deviation of speed is

$$\sigma_v = \sqrt{[v_s \sin(\delta_\theta)]^2 + (\delta v_w)^2} \tag{3.13}$$

where, v_s(m/s) is the speed of satellite, δ_θ（%s） is pointing stability of satellite and δv_w(m/s) is the turbulence of vertical wind speed.

Due to $\sigma_v \ll c$, we ignore relativistic effects, then the standard deviation of Doppler frequency shift is

$$\sigma_{Doppler} = \frac{2\sigma_v}{\lambda} \tag{3.14}$$

When the full width at half maximum of laser is *FWHM*, then the standard deviation of laser linewidth is

$$\sigma_{laser} = \frac{FWHM}{2\sqrt{2\ln 2}} \tag{3.15}$$

By using Gaussian distribution to present aerosol scattering Doppler broadening

spectra, the standard deviation of this spectra is

$$\sigma_{aer} = \sqrt{{\sigma_{laser}}^2 + {\sigma_{Doppler}}^2} \tag{3.16}$$

So the probability density function of aerosol scattering Doppler broadening spectra is as follows

$$W_a(\nu) = \frac{1}{\sigma_{aer}\sqrt{2\pi}} e^{-(\nu-\nu_0)^2/(2{\sigma_{aer}}^2)} \tag{3.17}$$

where ν_0 is the frequency of the wave the source emitted. $\sigma_{Doppler}$ is usually far less than σ_{laser}, so $\sigma_{aer} \approx \sigma_{laser}$.

The total spectral intensity distribution of backscattering light

The scattering ratio (also called backscatter ratio) is defined as the ratio of the sum of aerosol and molecular backscatter to molecular backscatter. The scattering ratio is determined from aerosol and molecular backscatter coefficients and can be written as:

$$R_\beta = \frac{\beta_a + \beta_m}{\beta_m} \tag{3.18}$$

where, β_a, β_m are aerosol and molecular backscatter coefficients, respectively.

The total spectral intensity distribution of backscattering light W_{Total} is calculated by linearly combining the normalized Rayleigh return spectral distribution W_m ,the normalized Mie return spectral distribution W_a , and the backscatter ratio R_β , so that

$$W_{Total} = \frac{1}{R_\beta} W_m + \frac{R_\beta - 1}{R_\beta} W_a \tag{3.19}$$

3.1.2 Spectral characteristics of CFPI

3.1.2.1 Modes in CFPI

As shown by Boyd and Gordon, the eigenmodes TEM_{mnq} of a confocal resonator are closely approximated by Gaussian-Hermite functions [23]. For a CFPI with concave mirrors of equal radius of curvature R and spacing d between the mirrors, the resonant frequencies are given by [24]

$$\nu / \nu_0 = (q+1) + \frac{1}{\pi}(m+n+1)\arccos(1-d/R) \tag{3.20}$$

where q is the number of longitudinal nodes in the standing wave (therefore a large non-negative integer), m and n are the mode numbers for Hermite-Gaussian modes.

For the special case of a confocal, or near confocal resonator, the resonant frequencies are [25]

$$v_{mnq} = [c/4(r+\varepsilon)][2q+(1+m+n)], \tag{3.21}$$

and

$$r+\varepsilon \approx (c/4v_0)[2q+(1+m+n)], \tag{3.22}$$

where the mirrors have radii r and they are separated by $r+\varepsilon \approx r$.

Thus, all transverse modes will resonate at cavity lengths of either,

$$r+\varepsilon = (c/4v_0)(2l+1);\ l : \text{an integer},(m+n) : \text{even}, \tag{3.23}$$

or

$$r+\varepsilon = (c/4v_0)(2l);(m+n) : \text{odd}. \tag{3.24}$$

If we assume that an arbitrary input field of frequency v is made up of an approximately equal number of even and odd transverse modes (a good approximation in any instance where mode-matching is not intentionally accomplished), then the cavity will be resonant for:

$$r+\varepsilon = cl/4v_0;\ l : \text{an integer}, \tag{3.25}$$

and the multimode free spectral range will be

$$\Delta v_f(\text{multimode}) = c/4r \tag{3.26}$$

On the other hand, if the input field exactly matches a single mode of the cavity, the free spectral range is

$$\Delta v_f(\text{single transverse mode}) = c/2r. \tag{3.27}$$

3.1.2.2 Spectral transmission and reflection

A spherical mirror Fabry-Perot interferometer is comprised of two identical spherical mirrors separated by a distance very nearly equal to their common radius of curvature. When light from a source lying close to the axis is incident on the interferometer, a multiple beam interference pattern is produced near the central plane

of the interferometer. According to paraxial optics, each mirror serves to image the other mirror back upon itself, so that a paraxial ray is reentrant, i.e., falls back upon itself, after traversing the interferometer four times. Owing to aberration, however, a general ray is not reentrant but follows a path such as shown in the following figure.

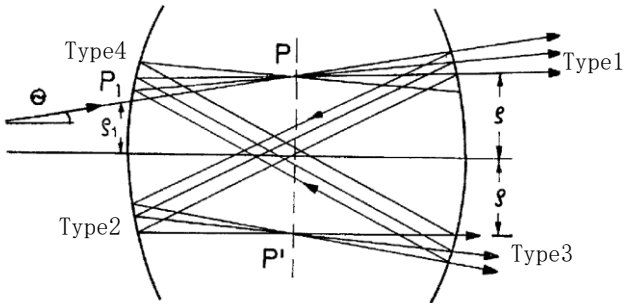

Figure 3.3 Aberrated ray path in an confocal Fabry-Perot interferometer.

The interference patterns produced in the central plane of the interferometer are described as [25]

Type 1:

$$I_1(\rho,\lambda) = I_0[T/(1-R^2)]^2\{1+[2R/(1-R^2)]^2\sin^2[\delta(\rho,\lambda)/2]\}^{-1} \quad (3.28)$$

Or,

Type 3:

$$I_3(\rho,\lambda) = R^2 I_1(\rho,\lambda) \quad (3.29)$$

where

$$\delta(\rho,\lambda) = (2\pi/\lambda)(4(r\ +\varepsilon) + \rho^4/r^3) \quad (3.30)$$

where T is the transmittance of one reflecting surface, R is the reflectivity of one reflecting surface and λ is the wavelength of incident light. ρ is the height at which an entering ray crosses the central plane of the CFPI. ε is the difference between CFPI mirror separation and confocal spacing r.

If the two beams are incoherent, then the transmission is

$$\begin{aligned} T_{multi}(\rho,\lambda) &= \frac{I_1(\rho,\lambda) + I_3(\rho,\lambda)}{I_0} \\ &= \frac{(1+R^2)[T/(1-R^2)]^2}{1+[2R/(1-R^2)]^2\sin^2[\delta(\rho,\lambda)/2]} \end{aligned} \quad (3.31)$$

If we define A to be the sum of the absorption and scattering at the mirrors, then $(1 - R) = (T + A)$. When the interferometer is set at the confocal spacing ($|\varepsilon| \leqq \lambda$), and

neglecting all but transmission losses at the mirrors (A=0), the transmission and reflection of the interferometer are

$$T_{multi}(\rho,\nu)=\frac{(1+R^2)/(1+R)^2}{1+[2\mathcal{F}^*/\pi]^2\sin^2\{(\pi\nu/c)[4(r+\varepsilon)\ +\rho^4/r^3]\}} \quad (3.32)$$

$$R_{multi}(\rho,\nu)=1-T_{multi}(\rho,\nu) \quad (3.33)$$

where ν is the frequency of incident light, the finesse of the confocal Fabry − Perot interferometer in multimode resonant condition is

$$\mathcal{F}^*=\pi R/(1-R^2) \quad (3.34)$$

If the type 1 and type 3 beams are coherent, the transmission and reflection are similar to the plate plane Fabry Perot interferometer. That is

$$T_{single}(\rho,\nu)=\frac{1}{1+[2\mathcal{F}^*/\pi]^2\sin^2\left(\frac{2r\pi\nu}{c}\right)} \quad (3.35)$$

$$R_{single}(\rho,\nu)=1-T_{single}(\rho,\nu) \quad (3.36)$$

where the finesse of the confocal Fabry-Perot interferometer in single mode resonant condition is

$$\mathcal{F}^*=\pi\sqrt{R}/(1-R) \quad (3.37)$$

3.1.3 The received signals in molecular and aerosol channels

Atmosphere mode

U.S. Standard Atmosphere (1976) has been used for the vertical profiles of temperature, pressure and number density [1]. The temperature $T(h)$, in degrees Kelvin and pressure $P(h)$, in pascals, as a function of the altitude h, in meters, for the first 11 km of the atmosphere can be determined from the expressions below:

$$T(h)=288.15-0.006545*h \quad (3.38)$$

$$P(h)=1.013\times10^5*\left[\frac{288.15}{T(h)}\right]^{\left(-\frac{0.034164}{0.006545}\right)} \quad (3.39)$$

The temperature and pressure from 11 to 20 km in the atmosphere can be determined by:

$$T(h)=216.65 \quad (3.40)$$

$$P(h)=2.269\times10^4*\mathrm{e}^{\left(-\frac{0.034164(h-11000)}{216.65}\right)} \quad (3.41)$$

The temperature and pressure from 20 to 32 km in the atmosphere can be determined by:

$$T(h) = 216.65 + 0.0010 * (h - 20,000) \tag{3.42}$$

$$P(h) = 5528.0 * \left[\frac{216.65}{T(h)} \right]^{\left(\frac{0.034164}{0.0010} \right)} \tag{3.43}$$

The temperature and pressure from 32 to 47 km in the atmosphere can be determined by:

$$T(h) = 228.65 + 0.0028 * (h - 32,000) \tag{3.44}$$

$$P(h) = 888.8 * \left[\frac{228.65}{T(h)} \right]^{\left(\frac{0.034164}{0.0028} \right)} \tag{3.45}$$

$P(h)$ and $T(h)$ having been determined, the number density of molecules can be found from:

$$N(h) = \left(\frac{28.964 \text{kg / kmol}}{8314 \text{J / kmol} - \text{K}} \right) \frac{P(h)}{T(h)} = 0.003484 * \frac{P(h)}{T(h)} \text{kg / m}^3 \tag{3.46}$$

The molecular backscatter coefficient can be computed using its relationship to atmospheric temperature and pressure through the equation [18]:

$$\beta_m = \frac{p}{KT} (5.45 \times 10^{-32}) \left(\frac{\lambda_0}{550} \right)^{-4.09} \tag{3.47}$$

where, T is the atmospheric temperature in units of Kelvin, p is the atmospheric pressure in units of kPa and K is the Boltzmann constant (1.38×10^{-23} J K^{-1}).

Furthermore, the molecular extinction coefficient α_m is calculated from the molecular backscatter coefficient though the relationship:

$$\alpha_m = \beta_m \left(\frac{8}{3} \right) \pi \tag{3.48}$$

The received backscattering signals

The received backscattering photons $N_a(z)$ and $N_m(z)$ relate to the total energy of the return signal (in number of photons) from aerosol and molecular scattering, respectively, from an atmospheric layer at altitude z. They are quantified by [26]

$$N_x(\lambda_0, z) = \frac{E\lambda_0}{hc}\frac{\pi D^2}{4}\frac{\beta_x(\lambda_0, z)}{R(z)^2}\tau(\lambda_0, z)^2 \Delta z_{LOS} T_{RX} T_{TX} \tag{3.49}$$

where the subscript *x* denotes the type of scattering particle, i.e. *a* for aerosol and *m* for molecule. The number of scattering particles in the illuminated volume, $\beta(\lambda_0, z)$, and one-way atmospheric transmission, $\tau(\lambda_0, z)$. Instrumental properties include laser energy *E*, the telescope diameter *D*, the range from the atmospheric layer to the instrument at altitude z_{sat}, $R(z) = (z_{sat} - z)/\cos(\Phi)$, and the depth of the illuminated layer, $\Delta z_{LOS} = \Delta z/\cos(\Phi)$, with Δz the range gate resolution and Φ the line-of-sight or laser beam incidence angle. In the simulations, we assume a uniform distribution of aerosols within a range gate. System optics are described with T_{TX} and T_{RX} that denote transmit and receive optics transmission, respectively, *c* is the speed of light and *h* is Planck's constant.

The spectral distribution of atmospheric scattering particles at altitude *z* is a superposition of the Mie and Rayleigh spectra as follows

$$N(\lambda_0, z, \nu) = N_a(\lambda_0, z)W_a(\nu) + N_m(\lambda_0, z)W_m(\nu) \tag{3.50}$$

Besides backscattered light from atmospheric particles, part of the earth radiance is directed towards the telescope receiver. The daytime earth radiance $L_{BKG}(W/(\mathrm{m}^2\mathrm{sr}\,\mu\mathrm{m}))$ and the corresponding number of photons at receiver input per micron of bandwidth for one range gate [26]

$$N_{BKG}(\lambda_0, z) = L_{BKG}(\lambda_0)\frac{\lambda_0}{hc}\frac{2\Delta z_{LOS}}{c}\left[\frac{\pi \Delta\theta_r D}{4}\right]^2 T_{RX} \tag{3.51}$$

where $\Delta\theta_r$ is the receiver field of view.

The signals detected in the aerosol channel and molecular channel are

$$\begin{aligned} S_{tot\_T} &= \eta_T \int_{-\infty}^{\infty} N(\lambda_0, z, \nu) T_{CFPI}(\nu)\, d\nu \\ &= \eta_T N_a(\lambda_0, z) \int_{-\infty}^{\infty} W_a(\nu) T_{CFPI}(\nu) d\nu \\ &\quad + \eta_T N_m(\lambda_0, z) \int_{-\infty}^{\infty} W_m(\nu) T_{CFPI}(\nu) d\nu \end{aligned} \tag{3.52}$$

$$S_{tot\_R} = \eta_R \int_{-\infty}^{\infty} N(\lambda_0, z, \nu) R_{CFPI}(\nu)\, d\nu$$
$$= \eta_R N_a(\lambda_0, z) \int_{-\infty}^{\infty} W_a(\nu) R_{CFPI}(\nu) d\nu \quad (3.53)$$
$$+ \eta_R N_m(\lambda_0, z) \int_{-\infty}^{\infty} W_m(\nu) R_{CFPI}(\nu) d\nu$$

where η_T and η_R are the quantum efficiency of transmitted channel detector (aerosol channel) and reflected channel detector (molecular channel), respectively. S_{tot_T} and S_{tot_R} are the numbers of received photo-electrons in the transmitted channel and reflected channel, respectively. $T_{CFPI}(\nu)$ and $R_{CFPI}(\nu)$ are the spectral transmission and reflection of CFPI, respectively.

By using the expressions of $N_a(\lambda_0, z)$ and $N_m(\lambda_0, z)$, the detected signals become

$$S_{tot\_T}$$
$$= \frac{E\lambda_0}{hc} \frac{\pi D^2}{4} \frac{\kappa_{AA}\beta_a(\lambda_0, z) + \kappa_{MA}\beta_m(\lambda_0, z)}{R(z)^2} \exp\left\{\frac{-2}{\cos(\Phi)} \int_z^{z_{sat}} [\alpha_a(\lambda_0, z') \quad (3.54)$$
$$+ \alpha_m(\lambda_0, z')] dz'\right\} \Delta z_{LOS} T_{RX} T_{TX} \eta_T$$

$$S_{tot\_R}$$
$$= \frac{E\lambda_0}{hc} \frac{\pi D^2}{4} \frac{\kappa_{AM}\beta_a(\lambda_0, z) + \kappa_{MM}\beta_m(\lambda_0, z)}{R(z)^2} \exp\left\{\frac{-2}{\cos(\Phi)} \int_z^{z_{sat}} [\alpha_a(\lambda_0, z') \quad (3.55)$$
$$+ \alpha_m(\lambda_0, z')] dz'\right\} \Delta z_{LOS} T_{RX} T_{TX} \eta_R$$

Where $\alpha_a(\lambda_0, z)$ and $\alpha_m(\lambda_0, z)$ are the extinction coefficients of aerosol and molecules, respectively. κ_{MM} is the fraction of molecular light detected by the molecular channel, κ_{AM} is the fraction of aerosol light detected by the molecular channel, κ_{MA} is the fraction of molecular light detected by the aerosol channel, and κ_{AA} is the fraction of aerosol light detected by the aerosol channel. And the expressions of these coefficients are

$$\kappa_{AA} = \int_{-\infty}^{\infty} W_a(\nu) T_{CFPI}(\nu) d\nu \quad (3.56)$$

$$\kappa_{AM} = \int_{-\infty}^{\infty} W_a(\nu) R_{CFPI}(\nu) d\nu \quad (3.57)$$

$$\kappa_{MA} = \int_{-\infty}^{\infty} W_m(\nu) T_{CFPI}(\nu) d\nu \tag{3.58}$$

$$\kappa_{MM} = \int_{-\infty}^{\infty} W_m(\nu) R_{CFPI}(\nu) d\nu \tag{3.59}$$

The background signal in aerosol channel S_{BKG_T} and the background signal in molecular channel S_{BKG_R} are

$$S_{BKG\_T} = \eta_T N_{BKG}(\lambda_0, z) T_{pk} \Delta\lambda_{FWHM\_CFPI} \tag{3.60}$$

$$S_{BKG\_R} = \eta_R N_{BKG}(\lambda_0, z)(\Delta\lambda_{FWHM\_FPFPI} - T_{pk}\Delta\lambda_{FWHM\_CFPI}) \tag{3.61}$$

Where T_{pk} is the peak transmission of the CFPI. $\Delta\lambda_{FWHM\_CFPI}$ is the FWHM of CFPI transmission profile and $\Delta\lambda_{FWHM\_FPFPI}$ is the FWHM of PFPI transmission profile.

3.1.4 Inversion algorithm

An inversion algorithm is used to retrieve aerosol optical properties, including aerosol extinction coefficient, backscattering coefficient, etc. The retrieved extinction coefficient and backscattering coefficient are

$$\alpha_a(\lambda_0, z) = \frac{1}{2}\frac{\partial}{\partial z}\ln\left(\frac{N_m(\lambda_0, z)R^2(z)}{\beta_m(\lambda_0, z)}\right) - \alpha_m(\lambda_0, z) \tag{3.62}$$

$$\beta_a(\lambda_0, z) = \frac{N_a(\lambda_0, z)}{N_m(\lambda_0, z)}\beta_m(\lambda_0, z) \tag{3.63}$$

where, the backscattering photons $N_m(\lambda_0, z)$ and $N_a(\lambda_0, z)$ are as follows

$$N_m(\lambda_0, z) = \frac{\frac{S_{tot\_R}}{\eta_R} - \frac{\kappa_{AM}}{\kappa_{AA}}\frac{S_{tot\_T}}{\eta_T}}{\kappa_{MM} - \frac{\kappa_{AM}\kappa_{MA}}{\kappa_{AA}}} \tag{3.64}$$

$$N_a(\lambda_0, z) = \frac{\frac{S_{tot\_T}}{\eta_T} - \frac{\kappa_{MA}}{\kappa_{MM}}\frac{S_{tot\_R}}{\eta_R}}{\kappa_{AA} - \frac{\kappa_{MA}\kappa_{AM}}{\kappa_{MM}}} \tag{3.65}$$

3.2 Parameter requirements of the spectral analysis system

The high spectral filter unit comprises a narrowband interference filter, a planar Fabry-Perot background filter (PFPI), and a confocal Fabry-Perot high spectral resolution filter (CFPI). In order to reduce the effect of background light, the free spectral range of the following filter should be greater than or equal to the bandwidth of the preceding filter. By the superposition of the three filters, the high spectral

resolution and the large receiving angle of the spaceborne HSRL for the spectral resolution system are achieved.

According to the equations (3.26), (3.27), (3.34), (3.37), the bandwidth (Full Width at Half Maximum) of CFPI is

$$FWHM_{single} = \left(\frac{c}{2r}\right)(1-R)/\pi R^{1/2} \tag{3.66}$$

$$FWHM_{multi} = \left(\frac{c}{4r}\right)(1-R^2)/\pi R \tag{3.67}$$

The ratio of the widths between the input field exactly matched to single mode of the cavity and multimode of the cavity which is [27]

$$\frac{FWHM_{single}}{FWHM_{multi}} = 1 - \frac{(1-R)^2}{8} + \cdots \tag{3.68}$$

Thus, for high reflectivity mirrors, there is no change in bandwidth of the CFPI. Only the spacing between adjacent resonances is different. So the single mode matching condition will be used to simulate the requirements of spectral resolution system. And then the influence of mode matching will be analyzed.

In order to meet the requirements of aerosol microphysical parameters inversion, the requirements of the accuracy and resolution of aerosol optical parameters are as follows [28]:

Table 3.1 The requirements of the accuracy and resolution of aerosol optical parameters.

Parameter	Resolution	Relative Error
Backscattering coefficient	Horizontal Resolution：≦50km	≦15%
	Vertical Resolution：≦150m	
Extinction coefficient	Horizontal Resolution：≦50km	≦15%
	Vertical Resolution：≦1km	

The input parameters of the simulation are as follows:

a) Lidar parameters

Table 3.2 The input parameters of the spaceborne HSRL.

NO.	Name of parameters	Value of

		parameters
1	Laser wavelength	532nm
2	Laser pulse energy	110mJ
3	Pulse repetition frequency	20Hz
4	Diameter of telescope	1m
5	Field of view	200μrad
6	Transmit optics transmission	0.9
7	Receive optics transmission	0.6
8	Quantum efficiency of detector	0.14

b) Platform parameters

Table 3.3 The parameters of the satellite platform.

NO.	Name of parameters	Value of parameters
1	Satellite altitude	500km
2	Satellite velocity	7km/s
3	Laser off-nadir angle	0 °
4	Pointing accuracy	0.02 °（3σ）
5	Pointing stability	2×10^{-4}（3σ）

c) Aerosol parameters

Table 3.4 The parameters of atmospheric aerosols.

NO.	Name of parameters	Value of parameters
1	Backscattering coefficient and lidar ratio (LR) of aerosol in low PBL layer	low：β=2E-6 middle：β=1E-5 high：β=2E-5 LR=50
2	Backscattering coefficient and lidar ratio of dust aerosol	β=3E-6 LR=40
3	Backscattering coefficient and lidar	β=8E-6

	ratio of cirrus	LR=30

Aerosol model considers three cases: clean sky, normal pollution and heavy pollution. The input profile of aerosol extinction coefficients in these three air conditions is shown in the following figure.

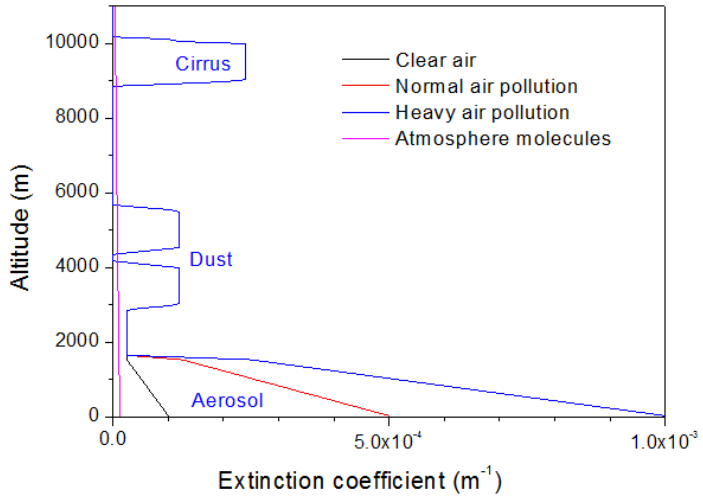

Figure 3.4 The input aerosol profiles for simulation.

In order to evaluate the effect of system parameters and to obtain their optimal values, a system simulation has been done. The flow diagram of the system simulation process is as follows:

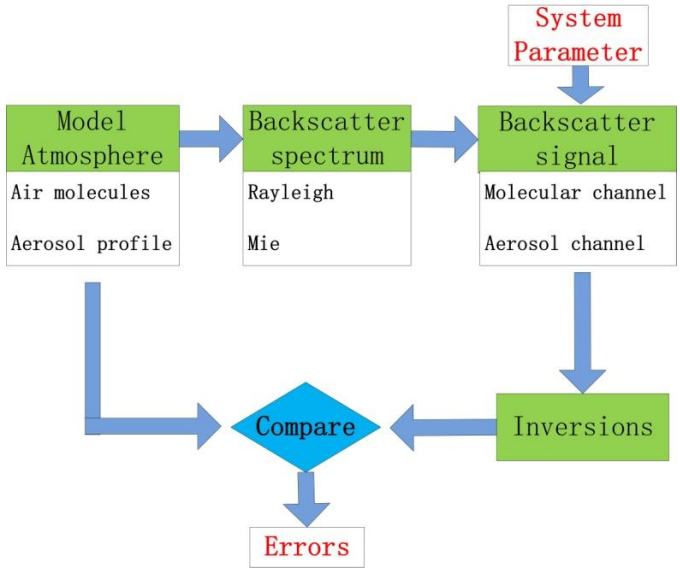

Figure 3.5 The flow diagram of the system simulation process.

Figure 3.5 shows the system simulation consisting of five steps: modeling atmosphere, Doppler broadening spectrum, backscatter signal calculation, inversion and comparison. Monte Carlo method is used to simulate the lidar return signals.

The selection of the spectral resolution of the spectral analysis system will affect the signal of the molecular and aerosol channels, and ultimately affect the measurement accuracy of the aerosol optical properties. The separated signals in aerosol channel and molecular channel are shown below [29]

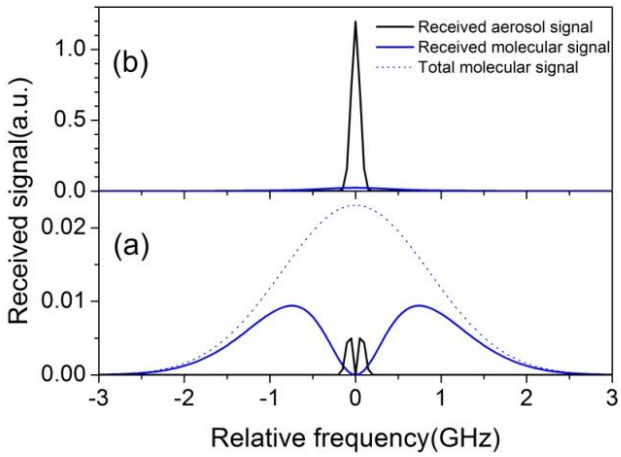

Figure 3.6 The spectrum of the transmitted signal and the reflected signal separated by the spectral analysis system of HSRL. (a) Signal spectrum in aerosol channel; and (b) signal spectrum in molecular channel.

It can be seen from the above figure that there are signals backscattered by atmospheric molecules in the aerosol channel, and there are also signals backscattered by aerosol in the molecular channel. That is to say, the crosstalk will occur after the separation of aerosol and atmospheric molecular signals by spectral filters. The quantity of crosstalk, which is related to the spectral resolution of spectral analysis system, will ultimately affect the measurement accuracy of the aerosol optical properties. On the other hand, the measurement accuracy of the aerosol optical properties is correlated with the signal-to-noise ratio of aerosol and molecular channels. The signal-to-noise ratio, especially in the molecular channel, is directly related to the resolution of the spectral analysis system. The influence of the spectral resolution of the high spectral resolution filter (CFPI) on crosstalk and signal-to-noise ratio is simulated, and then the influence of crosstalk and SNR on the measurement

accuracy of aerosol extinction coefficient is derived. The relationship between the spectral bandwidth of the high spectral resolution filter (CFPI) and the measurement accuracy of extinction coefficient of aerosol at 150m altitude is shown as the following figure [30]

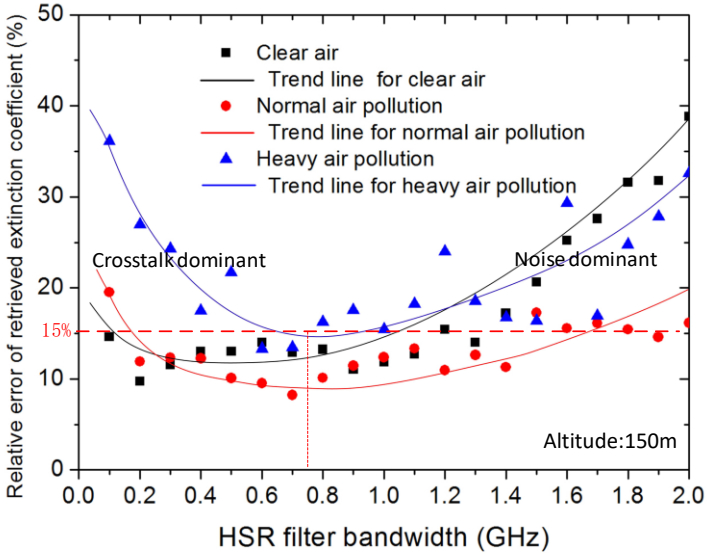

Figure 3.7 The influence of the bandwidth of the high spectral resolution filter on the relative error of retrieved aerosol extinction coefficient.

In Figure 3.7, the colors represent the different atmospheric conditions. From the figure, we can see that under the same spectral resolution, the different atmospheric conditions will affect the measurement accuracy of the aerosol extinction coefficients. The results show that the influence of crosstalk on the measurement accuracy is dominant when the spectral resolution bandwidth of the CFPI filter is small, and the effect of the signal-to-noise ratio on the measurement accuracy is larger when the spectral resolution bandwidth of the CFPI filter is larger. The relative measurement error of aerosol extinction coefficient under the three atmospheric conditions is less than 15%, which satisfies the requirements of measurement accuracy. To meet the requirements in all atmospheric conditions, the spectral resolution bandwidth of the CFPI filter should be more than 0.6GHz and less than 1GHz. In this case, the relative error of the retrieved molecular and aerosol signals caused by the uncertainties of the CFPI transmission should be lower than 10%. According to the equation (2.2), the radius of the CFPI mirrors is

$$r = \left(\frac{(U\mathcal{R})_{CFPI}}{4\pi^2}\right)^{1/2} = \left(\frac{cU}{4\pi^2\lambda_0\Delta\nu}\right)^{1/2} \tag{3.69}$$

When U=2.47E-8m^{2}sr and $\lambda_0 = 532\text{nm}$, Figure 3.8 shows the relation between r and $\Delta\nu$

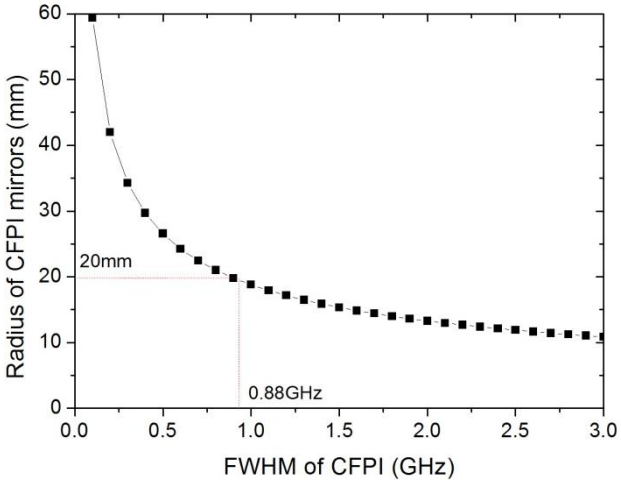

Figure 3.8 The relation between the radius and bandwidth of the CFPI.

In this spaceborne HSRL system, 0.88GHz has been selected as the bandwidth of the CFPI at 532nm, and the corresponding radius of CFPI is 20mm.

Laser linewidth is another factor that affects the measurement accuracy of aerosol optical properties. The relationship between laser linewidth and the retrieved aerosol extinction coefficient is shown in Figure 3.9 [30].

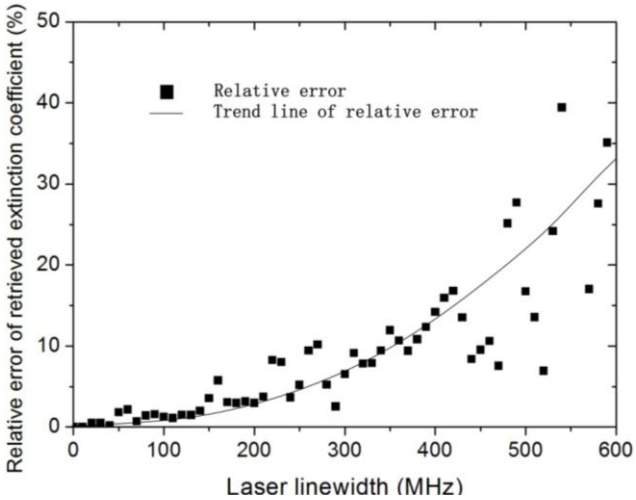

Figure 3.9 The influence of laser linewidth on the relative error of retrieved aerosol extinction coefficient.

Figure 3.9 shows that the relative error of retrieved aerosol extinction coefficient

is dependent on the laser linewidth. Laser linewidths larger than 100MHz will have a significant impact on the measurement accuracy of aerosol extinction coefficient. So the laser linewidth should be smaller than 100MHz.

The frequency-locking error between the center transmission wavelength of high spectral resolution filter of the receiver and the wavelength of laser transmitter also causes an error on retrieved extinction coefficient. The influence of frequency locking error on the measurement accuracy of aerosol extinction coefficient is shown in Figure 3.10 [30]:

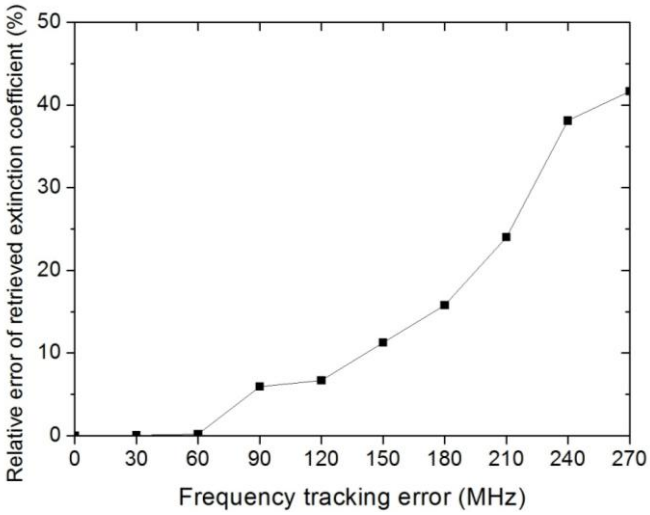

Figure 3.10 The influence of the frequency-locking error on the relative error of retrieved aerosol extinction coefficient.

Figure 3.10 shows that the frequency-locking error has significant impact on the relative error of retrieved aerosol extinction coefficient. But if it is lower than 60MHz, it has little influence on the measurement accuracy of aerosol extinction coefficient.

In order to assess the measurement accuracy of the profile of extinction coefficient and backscattering coefficient of PBL aerosol, simulations have been done in the different atmospheric conditions, including or excluding cloud or dust at night time.

1) Simulation results under the aerosol condition excluding cloud and dust layers

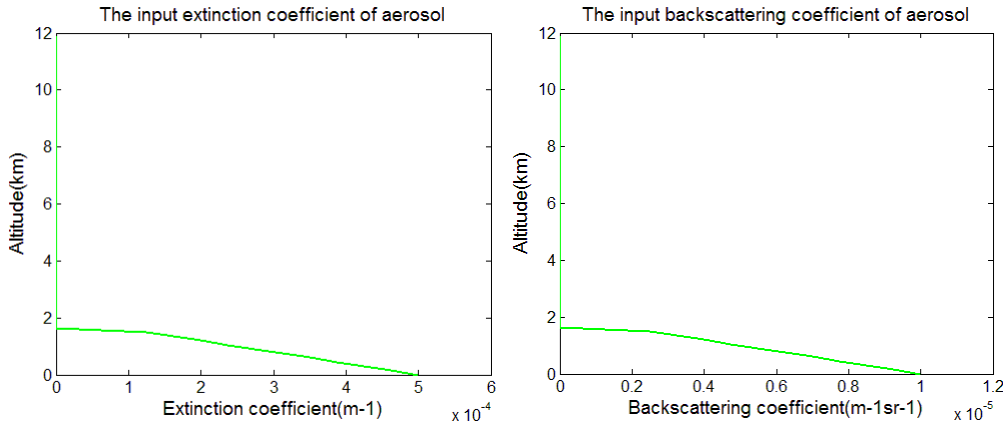

Figure 3.11 The input aerosol extinction coefficient and backscattering coefficient for simulation.

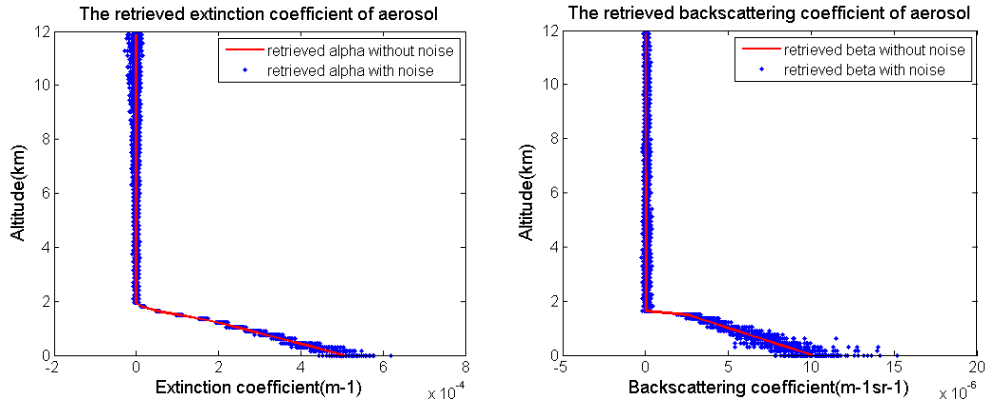

Figure 3.12 The aerosol extinction coefficient and the backscattering coefficient retrieved from the simulated signal.

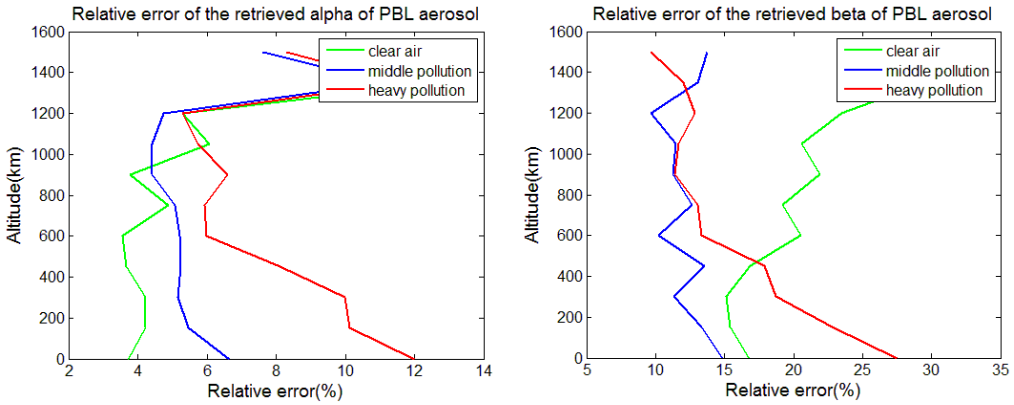

Figure 3.13 The relative measurement error of retrieved extinction coefficient and backscattering coefficient of PBL aerosol.

Figure 3.13 shows that the relative measurement error of the aerosol extinction coefficient satisfies the requirements of measurement accuracy. The relative measurement error of aerosol backscattering coefficient also meets the requirements

except the heavy pollution in low altitude and the low pollution in high altitude.

2) Simulation results under cloud and dust aerosol conditions

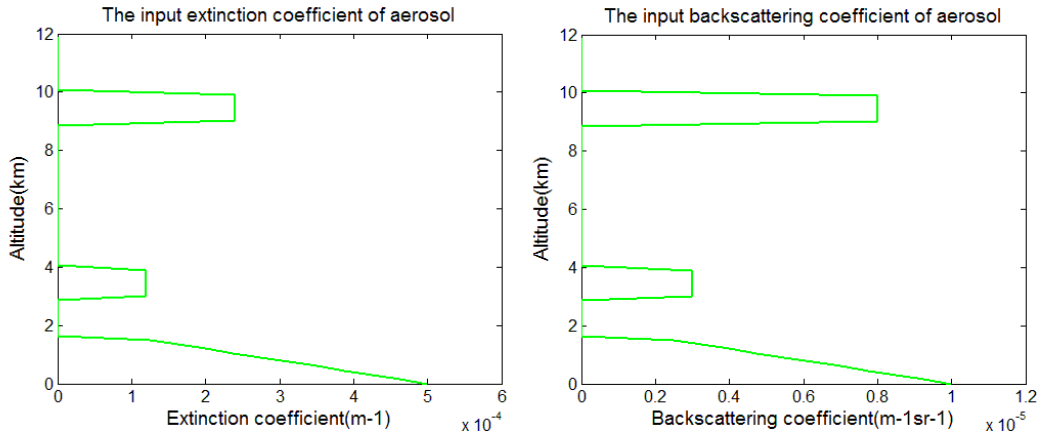

Figure 3.14 The input aerosol extinction coefficient and backscattering coefficient for simulation.

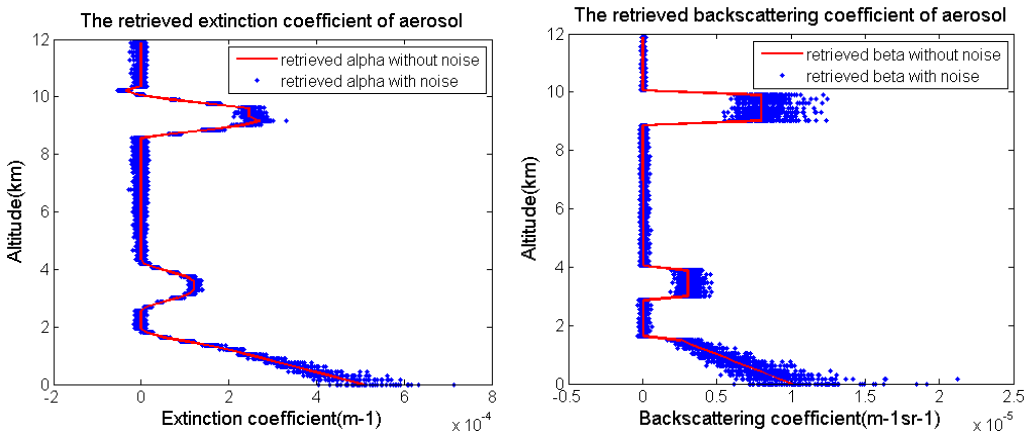

Figure 3.15 The aerosol extinction coefficient and the backscattering coefficient retrieved from the simulated signal.

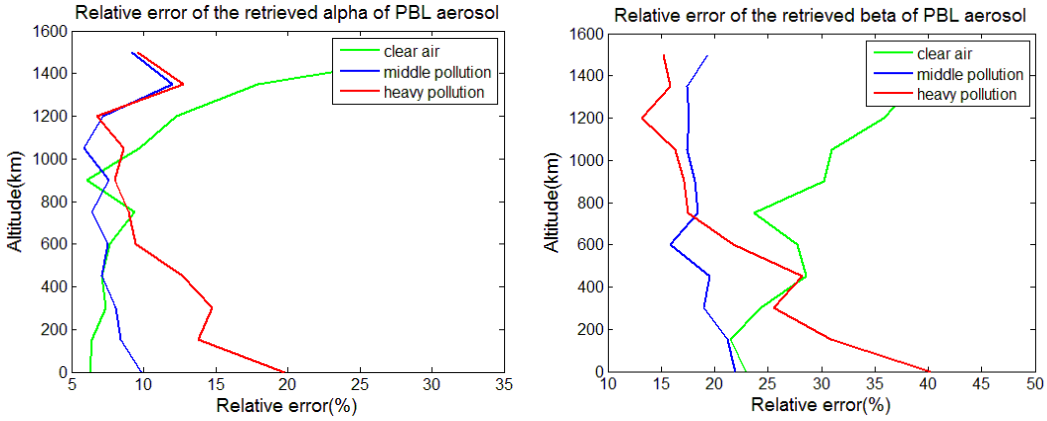

Figure 3.16 The relative measurement error of retrieved extinction coefficient and

backscattering coefficient of PBL aerosol.

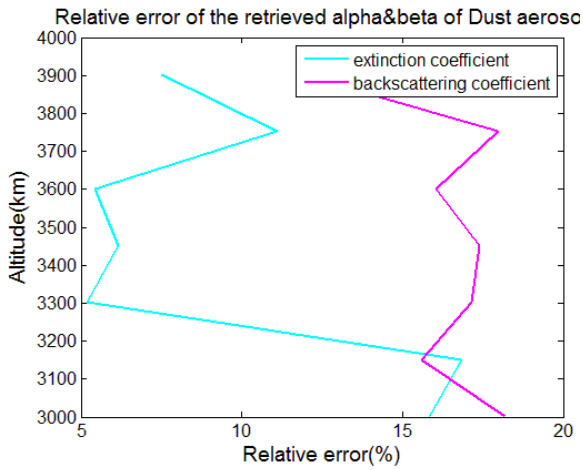

Figure 3.17 The relative measurement error of retrieved extinction coefficient and backscattering coefficient of dust aerosol.

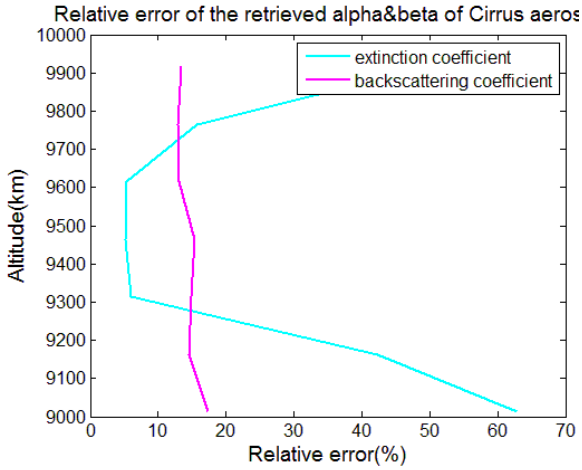

Figure 3.18 The relative measurement error of retrieved extinction coefficient and backscattering coefficient of cirrus aerosol.

Figure 3.11~Figure 3.18 show that the error of retrieved aerosol extinction coefficient in the low aerosol layer (PBL layer) meets the requirements of measurement accuracy even in the presence of cloud and dust aerosol. But the relative error of retrieved aerosol backscattering coefficient is a little higher. For the cirrus and dust, the accuracy of retrieved extinction coefficient and backscattering coefficient meets the requirements in some conditions.

3.3 Analysis and design of the spectral combination of the spectral analysis system

The spectral analysis system for the spaceborne HSRL includes a high spectral resolution combination and a frequency-locking subsystem. The high spectral resolution combination contains an interference filter, a planar Fabry-Perot interferometer (PFPI) and a confocal Fabry-Perot interferometer (CFPI). The schematic diagram of the spectral analysis system of this spaceborne HSRL is shown in Figure 3.19.

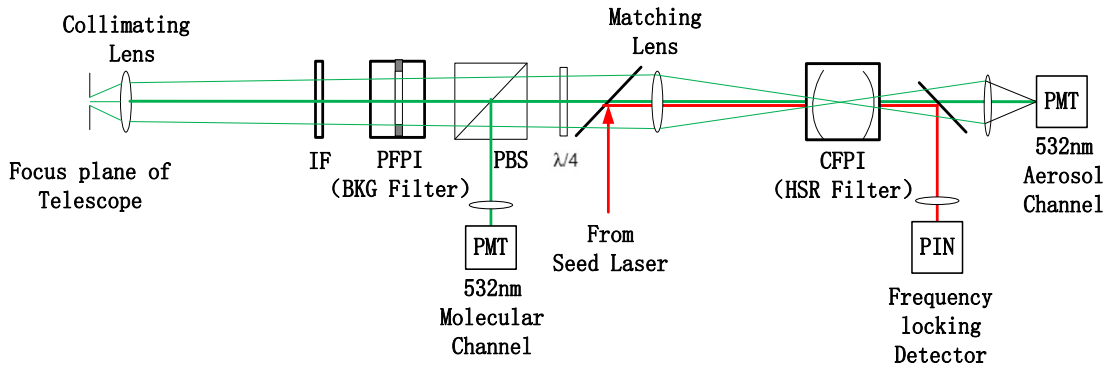

Figure 3.19 The schematic diagram of the spectral analysis system of the spaceborne HSRL.

Firstly, the telescope receives the light backscattered by atmospheric molecules and aerosols and focuses it to the focal plane. A collimating lens expands and collimates the beam to a low divergence beam. Secondly, the interference filter and the PFPI block the background light and pass through the backscattering light. Thirdly, the light with parallel polarization passes the polarization beam splitter and the quarter-wave plate, and then is focused to the CFPI by the matching lens. The light scattered by aerosols is transmitted and focused to the detector in aerosol channel. The light scattered by atmospheric molecules is reflected by the CFPI and passed the quarter-wave plate again, and then is reflected by the polarization beam splitter to the detector in molecular channel. Fourthly, a infrared beam from seed laser is introduced to the spectral analysis system and pass through the CFPI, then is focused to a detector in frequency-locking channel. The function of the infrared beam is to lock the center transmission wavelength with the wavelength of the seed laser (1064nm). Since the working 532nm light is the second harmonic light, so if the light from the seed laser is locked to the CFPI, the 532nm light also will be locked to the CFPI.

Due to the field of view of 200 μrad and the diameter 1m of the telescope, there is a divergence angle after the collimating lens. In order to make the light pass all the optical components (the optical path length between the collimating lens and the matching lens is 1.5m) and the divergence angle of the light is lower, the focal length of the collimating lens is optimally selected. The diameters of the beam on the collimating lens and the matching lens depending on the focal length of the collimating lens (F number is 5,the same with the telescope) is shown in Figure 3.20.

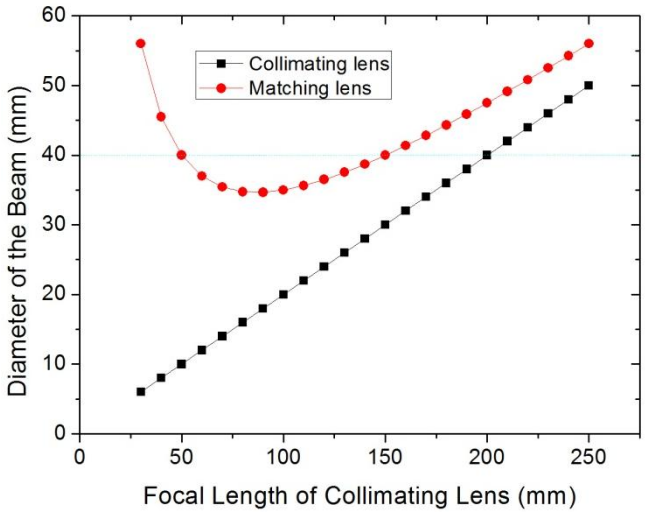

Figure 3.20 The diameters of the beam on the collimating lens and the matching lens depending on the focal length of the collimating lens.

In order to make the beam diameter on all the optical components less than 40mm, the focal length of collimating lens should be between 50mm and 150mm. The focal length of 100mm has been selected and the corresponding beam diameter on collimating lens and matching lens are 20mm and 35mm, respectively. And the divergence angle of the beam between these two lenses is 10mrad.

3.3.1 The analysis and design of the CFPI

3.3.1.1 The design of the CFPI mirrors

If the *étendue* of CFPI is larger than the *étendue* of beam, all the energy received by the telescope is used. In this case,

$$U = \frac{\pi^2 \rho^4}{r^2} = \frac{\pi^2 r \lambda_0}{\mathcal{F}_E} \geq 2.47 \times 10^{-8} \tag{3.70}$$

So the effective finesse

$$\mathcal{F}_E \leq 4.256 \tag{3.71}$$

And the radius of the beam on the center plane of the CFPI is

$$\rho \geq 1\text{mm} \tag{3.72}$$

As the beam waist of the fundamental Gaussian mode in the center of CFPI is

$$w_0 = \sqrt{\frac{\lambda_0 r}{2\pi}} = 41\text{um} \ll \rho \tag{3.73}$$

Therefore, it's impossible to match all the backscattering light to the fundamental Gaussian mode and the backscattering light is matched to the multimode of the CFPI.

The effective finesse of CFPI has a number of contributing factors: the mirror reflectivity finesse $\mathcal{F}_R$, the mirror surface quality finesse $\mathcal{F}_q$, and the finesse due to the illumination conditions (beam alignment and diameter) of the mirrors $\mathcal{F}_i$. Therefore, the effective finesse $\mathcal{F}_E$ can be written as [31]

$$\mathcal{F}_E = \left(\frac{1}{\mathcal{F}_R^2} + \frac{1}{\mathcal{F}_q^2} + \frac{1}{\mathcal{F}_i^2}\right)^{-\frac{1}{2}} \tag{3.74}$$

Surface quality finesse $\mathcal{F}_q$ involves mirror irregularities that cause a symmetric broadening of the line shape. The effect of these irregularities is a random position-dependent path length difference that blurs the line shape. The manufacturing process that is used to produce the cavity mirrors ensures that the contribution from $\mathcal{F}_q$ is negligible in comparison to specified total finesse.

The illumination finesse $\mathcal{F}_i$ will reduce the resolution as the beam diameter is increased or as the input beam is offset. When the finesse is limited by the $\mathcal{F}_i$ term, the measured line shape will appear asymmetric. The asymmetry is due to the path length difference between an on-axis beam and an off-axis beam, resulting in different mirror spaces to satisfy the maximum transmission criteria. The approximate decrease in path length for a beam at a distance ρ off axis is given by ρ^4/r^3.

To quantify the effects of the variable path length on $\mathcal{F}_i$, consider an ideal monochromatic input, a delta function in wavelength with unit amplitude, entering the Fabry-Perot cavity coaxial to the optic axis and having a beam radius a. The light entering the interferometer at ρ=+e, where e is infinitesimally small but not zero, will negligibly contribute to a deviation in the transmitted spectrum. Light entering the

cavity at ρ=+a will cause a shift in the transmitted output spectrum, since the optical path length of the cavity will be less than an approximate distance of $a^4/4r^3$. Assuming the input beam has a uniform intensity distribution, the transmitted spectrum will appear uniform in intensity and broader due to the shifts in the optical path length. As a result, the bandwidth is [31]

$$FWHM_i = \rho^4/4r^3 \tag{3.75}$$

Using λ/2 for the FSR, yields [32]

$$\mathcal{F}_i = (\lambda/2)/(\rho^4/4r^3) \tag{3.76}$$

The effective finesse, which includes significant contributions from both reflectivity finesse and illumination finesse $\mathcal{F}_i$, can be found (Note: $\mathcal{F}_q$ is still considered to have a negligible effect on $\mathcal{F}_E$):

$$\mathcal{F}_E = \left(\frac{1}{\mathcal{F}_R^2} + \frac{1}{\mathcal{F}_i^2}\right)^{-\frac{1}{2}} = \left(\left(\frac{1-\mathrm{R}^2}{\pi R}\right)^2 + \left(\frac{\rho^4}{2\lambda \mathrm{r}^3}\right)^2\right)^{-\frac{1}{2}} \tag{3.77}$$

Then the reflectivity of mirrors is

$$R = 73.1\%$$

And the reflective finesse is

$$\mathcal{F}_R = \frac{\pi R}{1-R^2} = 4.93$$

According to section 3.2, the gap of the CFPI cavity mirrors is designed to 20mm, so the radius of the cavity mirror is 20mm.

In this case, the free spectral range is

$$\mathrm{FSR} = c/4r = 3.75\mathrm{GHz}$$

The bandwidth of the CFPI at 532nm is

$$\mathrm{FWHM} = \mathrm{FSR}/\mathcal{F}_R = 0.76\mathrm{GHz}$$

3.3.1.2 The mode matching between backscattering light and the CFPI

Description of backscattering light

The backscattering light can be depicted as a fundamental mode Gaussian beam. The fundamental mode Gaussian beam has a Gaussian amplitude profile in the transverse direction and a hyperbolic profile in the longitudinal direction. The electric field of fundamental mode Gaussian beam $E_{beam}(x,y,z)$ is [33]

$$E(x,y,z) = E_0 \frac{w_0}{w(z)} \exp\left(-i\left[kz - \tan^{-1}\left(\frac{z}{z_0} \right) \right] - i\frac{kr^2}{2q(z)} \right) \tag{3.78}$$

For a given wavelength λ, the properties of a beam along its direction of propagation (denoted as the z-axis) can be characterized by a single complex parameter *q(z)*. For convenience, two real beam parameters *R* and *w* can be introduced [24]:

$$\frac{1}{q(z)} = \frac{1}{R(z)} - j\frac{\lambda}{\pi w^2(z)} \tag{3.79}$$

where, *R(z)* represents the radius of curvature of the wave front at *z*, and *w* represents the beam radius, i.e. the distance from the axis where the amplitude of the electric field drops to *1/e* times that one on the axis.

At the beam waist, *q* is purely imaginary, and the beam radius attains its minimum value w_0. The Rayleigh range z_0 and the divergence angle θ are as follows [34]:

$$z_0 = \pi w_0^{\,2} / \lambda \quad \text{(Rayleigh range)} \tag{3.80}$$

$$\theta = \lambda / \pi w_0 \quad \text{(divergence angle)} \tag{3.81}$$

Then, the expression for the beam radius at any position in terms of the waist radius is:

$$w^2(z) = w_0^{\,2}\left[1 + \left(\frac{\lambda z}{\pi w_0^{\,2}} \right)^2 \right] \tag{3.82}$$

And the radius of curvature of the wave front of the beam is as follows:

$$R(z) = z\left[1 + \left(\frac{\pi w_0^{\,2}}{z\lambda} \right)^2 \right] \tag{3.83}$$

According to the equations (3.81), (3.82), (3.83), radius of curvature of the wave front becomes

$$R(z) = -\frac{w^2(z)}{\sqrt{w^2(z)\theta^2 - \left(\frac{\lambda}{\pi}\right)^2}} \tag{3.84}$$

ABCD transfer matrixes

The transformation of Gaussian beams by optical elements such as lenses can be

expressed in terms of the same ABCD ray transfer matrix used in ray optics, but the transformation rule is different. For a given optical element, the beam parameter just after the element is related to that just before it by:

$$q_{out} = \frac{Aq_{in} + B}{Cq_{in} + D} \tag{3.85}$$

The mode matching configures are shown in Figure 3.21

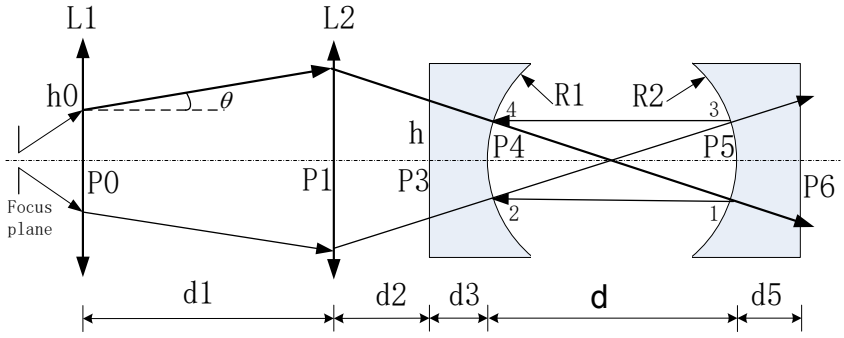

Figure 3.21 The schematic diagram of mode matching configures. L represents the lens, P represents the plane and d represents the distance. R1,R2 are the radius of the cavity mirrors, respectively. f1 and f2 are the focus length of L1 and L2, respectively.

The transfer matrix M_{xy} represents the transfer matrix from plane x to plane y. The subscript M means the center plane of the cavity. M_{cavity} is the ABCD matrix of the cavity. The expressions of the matrices are

$$M_{03} = \begin{bmatrix} 1 & \mathrm{d2} \\ 0 & 1 \end{bmatrix} \begin{bmatrix} 1 & 0 \\ -/\mathrm{f1} & 1 \end{bmatrix} \begin{bmatrix} 1 & \mathrm{d1} \\ 0 & 1 \end{bmatrix} \tag{3.86}$$

$$M_{34} = \begin{bmatrix} 1 & 0 \\ \frac{\mathrm{n}-1}{-\mathrm{R1}} & \mathrm{n} \end{bmatrix} \begin{bmatrix} 1 & \mathrm{d3} \\ 0 & 1 \end{bmatrix} \begin{bmatrix} 1 & 0 \\ 0 & \frac{1}{\mathrm{n}} \end{bmatrix} \tag{3.87}$$

$$M_{4M} = \begin{bmatrix} 1 & \mathrm{d}/2 \\ 0 & 1 \end{bmatrix} \tag{3.88}$$

$$\begin{aligned} M_{cavity} &= \begin{bmatrix} 1 & 0 \\ -\frac{2}{R_1} & 1 \end{bmatrix} \begin{bmatrix} 1 & d \\ 0 & 1 \end{bmatrix} \begin{bmatrix} 1 & 0 \\ -\frac{2}{R_2} & 1 \end{bmatrix} \begin{bmatrix} 1 & d \\ 0 & 1 \end{bmatrix} \\ &= \begin{bmatrix} 1-\frac{2d}{R_2} & 2d-\frac{2d^2}{R_2} \\ \frac{4d}{R_1R_2}-\frac{2}{R_1}-\frac{2}{R_2} & 1+\frac{4d^2}{R_1R_2}-\frac{4d}{R_1}-\frac{2d}{R_2} \end{bmatrix} \end{aligned} \tag{3.89}$$

The ABCD matrix of transmitted electric fields in the center plane of CFPI is

$$M_M = \begin{bmatrix} A_M & B_M \\ C_M & D_M \end{bmatrix} = M_{4M} * M_{34} * M_{03} \tag{3.90}$$

Description of CFPI

As shown by Boyd and Gordon, the eigenmodes TEM_{mnq} of a confocal resonator are closely approximated by Gaussian-Hermite functions [23]. The electric field $E_{CFPI}(x,y,z)$ is [33]

$$\begin{aligned} E_{l,m}(r) = E_0 \frac{w_0}{w(z)} H_l\left(\sqrt{2}\frac{x}{w(z)}\right) H_m\left(\sqrt{2}\frac{y}{w(z)}\right) \\ \times \exp\left(-\frac{x^2+y^2}{w^2(z)} - ik\frac{x^2+y^2}{2R(z)} - ikz + i(m+n+1)\tan^{-1}\left(\frac{z}{z_0}\right)\right) \end{aligned} \tag{3.91}$$

where, the spot size is

$$w(z) = w_0\left[1+\left(\frac{z}{z_0}\right)^2\right]^{1/2}, \quad z_0 = \frac{\pi w_0^{\,2}}{\lambda} \tag{3.92}$$

Mode matching between the backscattering beam and the CFPI

Only the light that matches the parameters given in the resonators inside a cavity and transmits through; light that does not match is reflected. In order to couple as much light into the cavity as possible, the incoming laser beam must have parameters matching those of a resonating mode [24]. The process of modifying the parameters of a laser beam to match that of a cavity is called mode matching. The quality of mode matching can be quantified with an overlap integral [35]:

$$\begin{aligned} &\eta(d1, f1, d2) \\ &= \frac{\left|\iint_{-\infty}^{+\infty} E_{beam}(x,y,d1,f1,d2) * E^*_{CFPI}(x,y,m,n)dxdy\right|^2}{\iint_{-\infty}^{+\infty} |E_{beam}(x,y,d1,f1,d2)|^2 dxdy \iint_{-\infty}^{+\infty} |E_{CFPI}(x,y,m,n)|^2 dxdy} \end{aligned} \tag{3.93}$$

where, $E_{beam}(x,y,d1,f1,d2)$ and $E_{CFPI}(x,y,m,n)$ is the amplitude distribution of the input beam and the CFPI cavity.

The expressions of these two amplitude distributions are

$$E_{beam}(x,y,d1,f1,d2) = E_0 \frac{w_0}{w_M(d1,f1,d2)} \exp\left(-\frac{i\pi(x^2+y^2)}{\lambda q_M(d1,f1,d2)}\right)$$

$$= E_0 \frac{w_0}{w_M(d1,f1,d2)} \exp\left(-\frac{(x^2+y^2)}{w_M(d1,f1,d2)} - \frac{i\pi(x^2+y^2)}{\lambda R_M(d1,f1,d2)}\right) \quad (3.94)$$

$$E_{CFPI}(x,y,m,n)$$

$$= E_0' \frac{w_0'}{w(0)} H_l(\sqrt{2}\frac{x}{w(0)}) H_m(\sqrt{2}\frac{y}{w(0)}) \exp\left(-\frac{(x^2+y^2)}{w^2(0)}\right) \quad (3.95)$$

where,

$$q_M(d1,f1,d2) = \frac{1}{R_M(d1,f1,d2)} - i\frac{\lambda}{\pi w_M^2(d1,f1,d2)} = \frac{q_{in}A_M(d1,f1,d2) + B_M(d1,f1,d2)}{q_{in}C_M(d1,f1,d2) + D_M(d1,f1,d2)} \quad (3.96)$$

Assume the incoming beam is a single Gaussian TEM00 mode beam, then

$$q_{in} = \frac{1}{R_{in}} - i\frac{\lambda}{\pi w_{in}^2} = -\frac{\sqrt{w_{in}^2\theta^2 - \left(\frac{\lambda}{\pi}\right)^2}}{w_{in}^2} - i\frac{\lambda}{\pi w_{in}^2} \quad (3.97)$$

where w_{in} is the radius of the input beam and θ is the divergence angle.

When w_{in}, θ and $w(0)$, the beam radius in the center of CFPI cavity, are given, the optimal d1, f1 and d2 are obtained when $\eta(d1,f1,d2)$ gets the maximum value. When the beam diameter in the center plane of the CFPI equals to the value ρ (=1mm), the required d1, f1 and d2 is obtained.

According to the input beam and the beam in the center of CFPI cavity introduced in section 3.3, w_{in}=10mm, θ=5mrad and $w(0)$=41um. Then the optimal focal length of the matching lens *f1* equals to 250mm. In this case, *d1* =1.3m and *d2* = 231mm.

3.3.2 The selection of interference filter and the requirements of planar Fabry–Perot interferometer (PFPI)

There are many ways in which optical filtering can be accomplished, only a few of which are commonly found in lidars. The amount of scattered light collected by the telescope is normally small, so the receiving optics must have a high transmission at

the laser wavelength. Most elastic lidars operate during the day, so that a narrow transmission band is required along with strong rejection of light outside the transmission band. These requirements limit the practical filters to interference filters and spectrometers [1] . In the high spectral resolution system of spaceborne HSRL, the combination of interference filter and planar Fabry-Perot interferometer is used to block the background light.

Interference filters are relatively inexpensive wavelength selectors that transmit light of a predetermined wavelength while rejecting or blocking other wavelengths. They consist of two or more layers of dielectric material separated by a number of coatings with well-defined thickness. A complete filter will consist of a substrate with the coatings bonded to other filters and colored glass used to block light outside the desired transmission band. An interference filter with a width less than 0.2nm is available from several companies. To reach the spectral bandwidth, the interference filter requires illumination with collimated light perpendicular to the surface of the filter. The central wavelength of an interference filter will shift to a shorter wavelength if the illuminating light is not perpendicular to the filter. The amount of shift with angle is determined as [1]

$$\frac{\lambda_{\theta}}{\lambda_{\text{normal}}} = \left(\frac{n^2 - \sin^2 \theta}{n^2} \right)^{\frac{1}{2}} \tag{3.98}$$

where, λ_{normal} is the center wavelength at normal incidence, λ_{θ} is the wavelength at an angle θ from the normal, and n is the index of refraction of the filter material.

Changing the angle of incidence can be used to “tune” an interference filter to a desired wavelength within a limited wavelength range. The central wavelength of an interference filter may also shift with increasing or decreasing temperatures. This effect is caused by the expansion or contraction of the spacer layers and by changes in their refractive indices. The changes are small over normal operating ranges (about 0.01nm/°C). When non collimated light falls on the filter, the results are similar to those non zero angle and depend on the details of the cone angle of the incoming light. When using the fused silicon material, the shift of the center wavelength with angle is shown in Figure 3.22

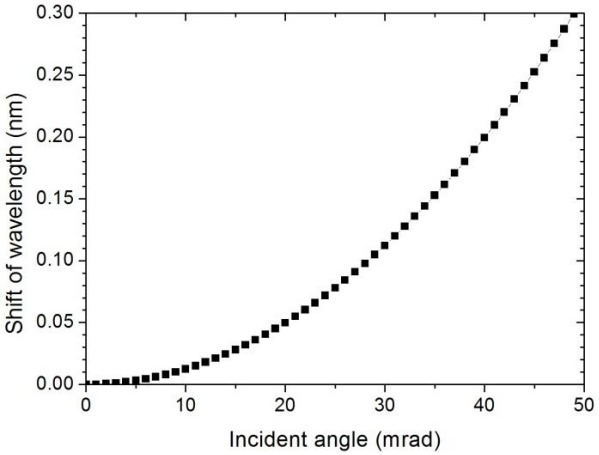

Figure 3.22 The shift of the center wavelength with an incident angle.

In Figure 3.22, when the incident angle is 10mrad, the shift of the wavelength is 0.013nm. Therefore, considering the influence of 1℃ temperature and 10mrad incident angle, the total shift of center wavelength will be 0.023nm. This means the free spectral range of planar Fabry-Perot interferometer should be larger than 0.223nm. In this spectral analysis system, the free spectral range of PFPI is 330GHz (～0.33nm).

In addition, the bandwidth of PFPI should be larger than the free spectral range of CFPI. For blocking the background light, the small bandwidth of PFPI is better, but if the bandwidth of PFPI is close to the free spectral range of CFPI, the slight shift of center wavelength between the PFPI and the CFPI will change the transmission and reflection of the spectral analysis system. This means a compromise is needed. The bandwidth of 7.5GHz is selected for planar Fabry-Perot interferometer and a temperature controller of PFPI with very high accuracy of is employed.

3.3.3 The analysis and design of the PFPI

Since the signal-to-noise ratio (SNR) of the 532 nm channel in HSRL is background limited during daytime operation, the basic requirements of the spectral filtering system are to match the laser wavelength, have a bandpass which is close to free spectral range of CFPI and block all other radiation over the PMT response region. The parameter requirements have been introduced in section 3.3.3. For space application, the PFPI and its housing must survive the launch vibration environment, space survival temperatures and the space radiation environment.

Different with ideal plate-plane Fabry-Perot interferometers, the PFPI used in HSRL have to receive divergent light. Due to the slight difference of laser wavelength between ground and in-orbit operation, wavelength tuning of PFPI is required.

3.3.3.1 The type selection of PFPI

There are several types of planar Fabry-Perot interferometer (etalon): bare solid etalon, solid etalon sandwiched between two thick fused silica windows ("sandwich etalon"), air-gap etalon, tunable piezoelectric controlled etalon, and pressure tunable etalon. The tunable piezoelectric controlled etalon and pressure tunable etalon both require more weight and cost to implement as a space qualified unit than other approaches, as well as introduce higher risk because of complexity (including a feedback control system). The simple solid design vastly simplified the electronics and optical requirements making space qualification much easier. Since the exact laser wavelength of the laser was not known when the etalon was being developed and there is a slight manufacturing error in the etalon thickness it was decided that tilt tuning would be used to match the laser wavelength on the ground. In space, wavelength-matching adjustment would be accomplished by temperature tuning the etalon [36].

The solid etalon and air-gap etalon are two of simple selections. They are shown in Figure 3.23.

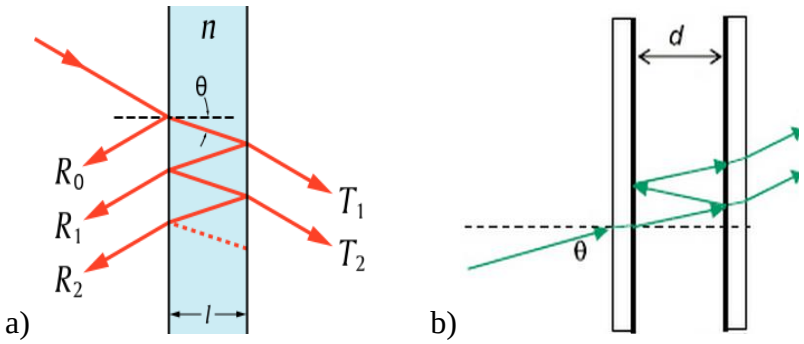

Figure 3.23 Two optional solutions for PFPI. a) Solid etalon; b) air-gap etalon.

The bare solid etalon was found hard to mount for launch vibration survivability and still maintain the required optical performance. When the required forces were exerted on the bare solid etalon, distortions in the etalon caused an unacceptable

increase in the bandwidth. And the air-gap etalon is more susceptible to performance degradation with tilt tuning than the solid etalon. Therefore the "sandwich etalon" was selected and proved to be very mechanically stable and ideal for space use were only a small amount of wavelength tuning is required.

For this HSRL, bare solid etalon and a mount with a temperature controller is used as background planar Fabry-Perot interferometer filter (PFPI).

3.3.3.2 The theory of PFPI

Effective Finesse

The concept of "finesse" was introduced as a figure of merit for the sharpness of a peak in Airy function compared with its inter-order spacing. In the ideal case, the angular width of a peak depends only on the quality of the reflective coating of the etalon cavity, called reflective finesse. The reflective finesse $\mathcal{F}_R$ has been discussed in chapter 2, and the formula is

$$\mathcal{F}_R = \frac{\pi\sqrt{R}}{1-R} \tag{3.99}$$

The defects of real PFPI cause a broadening of the spectral profile which can be taken into account as another term of finesse. There are three types of defects contributing to the total defect finesse $\mathcal{F}_D$, which is shown in Figure 3.24 [37].

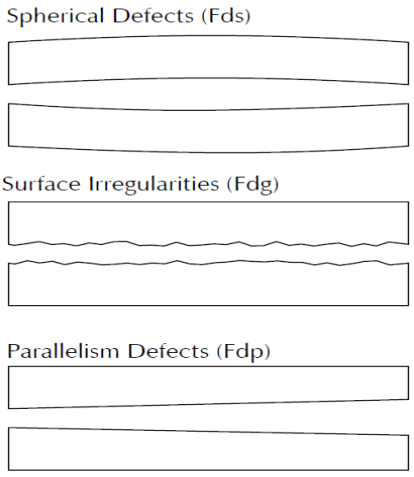

Figure 3.24 Three types of defects contributing to the total defect finesse.

The effect of a non-planar plate is modeled by the spherical defect finesse $\mathcal{F}_{DS}$, where δ_{DS} is the peak to valley value of deviation from the plane surface [38].

$$\mathcal{F}_{DS} = \frac{\lambda_0}{2\delta_{DS}} = \frac{K_S}{2} \tag{3.100}$$

Aside from systematic surface defects, a surface noise is always present after the plate has been polished. It can be described with the root mean square (RMS) of the difference between the measured and the ideal surface. It is called δ_{DG}, where the G stands for Gaussian as the remaining noise, after eliminating all systematic, is Gaussian. The Gaussian defect finesse is then

$$\mathcal{F}_{DG} = \frac{\lambda_0}{4.7\delta_{DG}} = \frac{K_G}{4.7} \tag{3.101}$$

Another problem is related to the fact that the internal gap of the interferometer can be wedged. In this case the nominal gap distance *d* is a mean of the value over the aperture of the instrument, since *d* vary linearly over the diameter of the etalon. The parallelism defect finesse $\mathcal{F}_{DP}$ takes into account the effects of a not parallel couple of plates. δ_{DP} is the spatial value corresponding to the difference between the maximum and minimum *d*.

$$\mathcal{F}_{DP} = \frac{\lambda_0}{\sqrt{3}\delta_{DG}} = \frac{K_P}{\sqrt{3}} \tag{3.102}$$

So the total defect finesse $\mathcal{F}_{\mathrm{D}}$ is calculated by the following formula

$$\frac{1}{\mathcal{F}_D^2} = \frac{1}{\mathcal{F}_{DS}^2} + \frac{1}{\mathcal{F}_{DG}^2} + \frac{1}{\mathcal{F}_{DP}^2} \tag{3.103}$$

And then

$$\mathcal{F}_D = \frac{\lambda_0}{(4\delta_{DS}^2 + 22\delta_{DG}^2 + 3\delta_{DP}^2)^{1/2}} \tag{3.104}$$

The beam divergence also influences the actual finesse of a real PFPI. The incident beam has a certain amount of divergence resulting in a different angle of incidence for the outer rays of the beam, broadening the transmission profile. Given the solid angle of the beam Ω or the divergence angle of the beam θ_{DIV}, the divergence finesse is then defined as

$$\mathcal{F}_{DIV} = \frac{\lambda_0}{d\theta^2_{DIV}} = \frac{2\pi}{m\Omega} \tag{3.105}$$

It is also called the aperture finesse, since the aperture of the instrument limits the

range of possible angles of the diverging beam. All previous definitions of finesse are now included in an effective finesse $\mathcal{F}_E$ which now describes a real PFPI.

$$\frac{1}{\mathcal{F}_E^2} = \frac{1}{\mathcal{F}_R^2} + \frac{1}{\mathcal{F}_D^2} + \frac{1}{\mathcal{F}_{DIV}^2} \tag{3.106}$$

Then

$$\mathcal{F}_E = \left(\frac{1}{\mathcal{F}_R^2} + \frac{1}{\mathcal{F}_D^2} + \frac{1}{\mathcal{F}_{DIV}^2} \right)^{-\frac{1}{2}} \tag{3.107}$$

$$\mathcal{F}_E = \frac{1}{\sqrt{\frac{(1-R)^2}{\pi^2 R} + \frac{4\delta_{\mathrm{DS}}^2 + 22\delta_{\mathrm{DG}}^2 + 3\delta_{\mathrm{DP}}^2}{\lambda_0^2} + \frac{d^2\theta_{DIV}^4}{\lambda_0^2}}} \tag{3.108}$$

***Étendue*, Bandwidth (FWHM) and Transmission**

The ultimate instrumental resolution $\mathcal{R}_0$ could be obtained only with an infinitesimally small axial aperture. In this case, of course, the *étendue* is also infinitesimal. A reasonable compromise between spectral resolving power and *étendue* can be reached by increasing the mirror aperture until the resolving power $\mathcal{R}$ is reduced to a value of approximately $0.7\mathcal{R}_0$ [25]. According with the introduction of ideal PFPI, the resolving power $\mathcal{R}$ of real PFPI is

$$\mathcal{R} = \frac{\lambda_0}{\Delta\lambda} = 0.7\mathcal{R}_0 = 0.7 * \frac{2d\mathcal{F}^*}{\lambda_0} = 1.4d\mathcal{F}^*/\lambda_0 \tag{3.109}$$

So the bandwidth $\Delta\lambda$ is

$$\Delta\lambda = \frac{\lambda_0^2}{1.4d\mathcal{F}^*} \tag{3.110}$$

In this case, the *étendue* is

$$U = \pi \frac{D^2}{4} \frac{\lambda_0}{d \cdot \mathcal{F}^*} \tag{3.111}$$

So the *product* of the resolving power and *étendue* is

$$(U\mathcal{R})_{\mathrm{PFPI}} = 0.7\pi \frac{D^2}{2} \tag{3.112}$$

If A is defined as the sum of the absorption and scattering at the mirrors, then (1 - *R*) = (*T* + *A*). Using the effective finesse, then the transmission is

$$T = \left(1 - \frac{A}{1-R}\right)^2 \frac{1}{1 + \left(\frac{2\mathcal{F}_E}{\pi}\right)^2 \sin^2\frac{\delta}{2}} \tag{3.113}$$

According to the equation (3.113), there is also an additional reduction in the

maximum transmission intensity. The maximum transmission is [38]

$$T_{pk} \approx \left(1 - \frac{A}{1-R}\right)^2 \left[1 - \frac{1+R}{2}\left(1 - \frac{\mathcal{F}_E}{\mathcal{F}_R}\right)\right] \tag{3.114}$$

Wavelength tuning by Tilting and Temperature tuning

Since the exact wavelength of the laser was not known when the etalon was being developed and there is a slight manufacturing error in the etalon thickness it was decided that tilt tuning would be used to match the laser wavelength at the ground. In space, wavelength-matching adjustment would be accomplished by temperature tuning the etalon [36].

The effect of tilting can be estimated simply from the knowledge of the index of the interferometer and the angle of incidence. For small angles of incidence, the spectral shift $\Delta\lambda_0$ is given by [39]

$$\Delta\lambda_0 = \lambda_0 \frac{\theta^2}{2n'^2} \tag{3.115}$$

where θ is the tilted angle, n' is the refraction index inside the Fabry-Perot interferometer, and λ_0 is the wavelength at normal incidence.

Tilt tuning of the etalon can only be used over a limited range since tilting the etalon increases the bandwidth and decreases the peak transmission. This occurs because the etalon is operating in a divergent beam rather than a collimated beam. The new bandwidth $\Delta\lambda_{new}$ and the relative peak transmission τ_{pk} are functions of tilt angle.

$$\Delta\lambda_{new} = \sqrt{\Delta\lambda^2 + [(2 \times X \times \Theta \times \lambda_0)/n_g^{\,2}]^2} \tag{3.116}$$

$$\tau_{pk} = \frac{\Delta\lambda}{(2 \times X \times \Theta \times \lambda_0)/n_g^{\,2}} \times \arctan\left[\frac{(2 \times X \times \Theta \times \lambda_0)/n_g^{\,2}}{\Delta\lambda}\right] \tag{3.117}$$

where $\Delta\lambda$ is the bandwidth with no tilt, X is the tilt angle, Θ is the half divergent angle, λ_0 is the wavelength at normal incidence, and $n_g = n'$ is the refraction index inside the Fabry-Perot interferometer.

Temperature tuning is primarily used for solid etalons. Temperature-tuning changes both the actual spacing of the reflective surfaces via expansion and the index of refraction of the material, which changes the optical spacing. The tuning result can

be given by [31]

$$\frac{\partial(\mathrm{FSR})}{\partial T} = -(\mathrm{FSR})\left(\frac{1}{n}\frac{\partial \eta}{\partial T} + \frac{1}{d}\frac{\partial d}{\partial T}\right) \tag{3.118}$$

The transmission of the etalon, T, for collimated light as a function of the temperature change,ΔT, and the incident angle θ, is given by

$$T(\theta, \Delta T) = \frac{T_{pk}\tau_{pk}}{1 + \left(\frac{2\mathcal{F}_E}{\pi}\right)^2 \sin^2\left[\frac{4\pi}{\lambda_0} n_0(1 + \beta\Delta T n_0^{-1}) L_0(1 + \alpha\Delta T)\cos\theta\right]} \tag{3.119}$$

Where L_0 is the etalon thickness at a reference temperature, $\beta = \partial n/\partial T$ is temperature coefficient of refractive index, $\alpha = L^{-1} \cdot \partial L/\partial T$ is the coefficient of thermal expansion, and the rest of the parameters are defined earlier.

3.3.3.3 The design of the PFPI

Fused silica was chosen as a material for the spacer layer of PFPI because of its thermo-optical characteristics. The refractive index of fused silica n = 1.461. According to the parameter requirement presented in section 3.3.3, the free spectral range is *FSR* = 330GHz and the bandwidth is *FWHM*=7.5GHz. So the finesse is 44. The thickness of the solid PFPI L_0 is

$$L_0 = \frac{c}{2nFSR} = 0.311mm \tag{3.120}$$

Considering only the reflective finesse, the reflectivity of the mirrors is

$$\mathrm{R} = \frac{\left(\frac{\pi^2}{\mathcal{F}^2} + 2\right) - \sqrt{\left(\frac{\pi^2}{\mathcal{F}^2} + 2\right)^2 - 4}}{2} = 93.1\% \tag{3.121}$$

In practice, when the residual micro-roughness of the etalon surfaces is 1nm, the flatness figures is about $\lambda_0/100$ across the clear aperture, and the parallelism error across the clear aperture is $\lambda_0/50$, the effective finesse becomes one half of the reflective finesse. In this condition, the bandwidth of PFPI becomes to 15GHz.

3.4 Analysis and design of the frequency-locking subsystem

3.4.1 The introduction of frequency-locking methods

Frequency stabilization, or frequency “locking,” involves concepts such as error signals and feedback that are part of control theory. There is another, widely used and

very effective frequency stabilization method that makes use of a Fabry-Perot etalon rather than an absorption resonance to produce an error signal. An advantage of the Fabry-Perot is that it offers a wide range of possible resonance frequencies to choose from, whereas Lamb-dip stabilization requires a saturable molecular transition close to the laser frequency [34].

When light from a laser is incident on a Fabry-Perot etalon, the transmitted (or reflected) intensity can provide the error signal needed to stabilize the laser frequency. For instance, if the intensity reflected by the Fabry-Perot is zero, the laser frequency must be a resonance frequency of the cavity. A deviation of the laser frequency from this cavity resonance will result in some reflected intensity that can serve as the error signal for a feedback loop that locks the laser frequency to the cavity resonance. An attractive feature of this approach is that the frequency locking is not affected by intensity fluctuations of the laser: as long as the reflected intensity is zero the laser frequency is locked to the cavity resonance.

However, the variation of the reflected (and transmitted) intensity is symmetric about a cavity resonance. This means that a nonzero reflected intensity (error signal) cannot tell us whether the laser frequency should be increased or decreased in order to bring it back to the locking frequency. In an old frequency stabilization technique the laser is locked to one side of a cavity resonance, so that a change in the reflected intensity provides information about the sign of the laser frequency fluctuation. The disadvantage of this "side-locking" technique is that a change in the reflected intensity can arise not only from a fluctuation in the laser frequency but also from a fluctuation in the laser intensity. Improving frequency stability by side locking, therefore, requires that the laser intensity be separately stabilized. The essence of the "Pound–Drever–Hall" (PDH) frequency stabilization method is to get around this problem by producing an error signal that depends on the sign of the deviation of the laser frequency from the cavity resonance frequency. Such an error signal, which is obtained by modulating (or "dithering") the laser output to generate sideband frequencies, provides information as to whether the laser frequency is above or below the frequency, to which we wish to lock. The degree of frequency stability that is

possible with the Pound– Drever–Hall method increases with increasing cavity finesse.

Another approach, which can be used to lock the laser frequency to the center of a cavity or atomic resonance, is to dither the laser frequency slowly compared to the linewidth of the resonance. A disadvantage of slow dithering is that the available servo bandwidth is limited by the (slow) modulation frequency. The Pound–Drever–Hall method, however, can be shown to allow for much larger modulation frequencies and servo bandwidths.

Single-frequency laser oscillation can also be obtained by injection locking with a "seed laser." In this technique the output of a single-mode, low-noise, usually low power laser is injected through a resonator mirror of a "slave laser" having nearly the same oscillation frequency. Together with locking electronics controlling the length of the slave laser resonator, this acts to force the slave laser to oscillate at the seed laser frequency with much less noise than would be the case if it ran freely. Injection locking is used to reduce the noise of a high-power (slave) laser.

There are several possible implementations to realize the frequency locking [40]

AOM tuning locking

A common method is to stabilize the laser to a fixed frequency reference such as a cavity or a molecular reference and shift the frequency of the stabilized laser with an AOM. Due to the Doppler effect, the diffracted beam is shifted in frequency by the magnitude of the sound wave frequency, which is adjustable. The tuning range is limited to a few ten MHz. AOMs are usually avoided in space missions, due to the large RF power consumption and the low operating power efficiency.

Sideband locking

Sideband locking uses a fixed frequency reference and a modified Pound Drever Hall (PDH) locking scheme. The easiest realization of sideband locking is that not the carrier, but the sideband is stabilized to the reference line (single sideband locking). Thus, when changing the modulation frequency the sideband stays locked to the reference line and the carrier frequency is shifted relative to the reference frequency. If the sideband is additionally modulated (dual sideband locking), the second

modulation frequency can be used for demodulation of the signal. This brings the advantage of an unchanging demodulation frequency, which is not the case for the single sideband approach.

The disadvantage of this method is the complex modulation spectrum of the laser carrying the risk that the carrier or higher order sidebands couple into higher order modes of the cavity. Furthermore, in order to obtain a large tuning range, a frequency synthesizer which provides GHz frequencies is required.

Piezo tuning locking

Tuning of a cavity stabilized laser can easily be achieved by changing the cavity length. The resonance frequencies of a cavity are given by

$$\nu_q = q\frac{c}{2L} \tag{3.122}$$

Where, L is the cavity length, c the speed of light and q an integer. A cavity laser lock is usually performed by using one of those resonance lines as frequency reference. Changing the cavity length, tunes the resonance frequency and thus the laser frequency. The cavity length can be changed slowly by temperature: $\delta_\nu/\nu = \alpha T$, where α is the coefficient of thermal expansion (CTE) of the cavity spacer material. With a piezoelectric actuator, the cavity length can be manipulated in a fast and defined way. Piezo-tunable cavities are already commonly used for laser resonators or as transfer cavities. A piezo-tunable cavity where the cavity spacer is compressed with an extrinsic actuator has been implemented with stabilities in the 10^{-13} range, allowing however only a few 10 kHz tuning range. Furthermore, it has been demonstrated that a laser system including stabilization to a cavity with an intrinsic piezo actuator can be realized with a few kHz linewidth.

3.4.2 The parameter requirements of the frequency-locking subsystem

The range of scanning distance

The great advantage of the CFPI over a general curved mirror resonator is the freedom from the necessity to mode-match in order to observe a clean spectrum. This, as we have just seen, is due to the frequency degeneracy of even and odd transverse modes of a confocal cavity. It can readily be shown from mode equation of CFPI that

the maximum value of $|\epsilon|$, the departure from exact confocal mirror spacing, which can be tolerated without allowing the TEM_{mn} transverse mode to resonate at an observably different mirror spacing from that at which the TEM_{00} mode is resonant, is given by [25]:

$$|\epsilon|_{max} = \pi r/2(1+m+n)\mathcal{F} \tag{3.123}$$

Thus the CFPI with r = 20mm and a finesse of 4.256 will begin to suffer a loss in effective finesse for (m + n) =100 when $|\epsilon|$ becomes greater than about 73um. Thus the variation in the mirror separation which occurs during direct scanning (less than a wavelength) is too small to affect the transverse mode degeneracy. In this frequency-locking subsystem, the scanning range is less than one wavelength of the locking light (1.064um) since just one transmitted peak is needed.

The locking precision of CFPI cavity length

According to the equation (3.31), the transmission of CFPI is

$$T_{multi}(\rho,\lambda,\varepsilon) = (1 + R^2)[T/(1-R^2)]^2\left\{1+\left[\frac{2\mathcal{F}^*}{\pi}\right]^2 \sin^2[\delta(\rho,\lambda)/2]\right\}^{-1} \tag{3.124}$$

where,

$$\mathcal{F}^* = \pi R/(1-R^2) \tag{3.125}$$

$$\delta(\rho,\lambda) = (2\pi/\lambda)\Delta s = (2\pi/\lambda)(4(r+\varepsilon)+\rho^4/r^3) \tag{3.126}$$

When the maximum transmission is reached, $\delta(\rho,\lambda)$ should be an integer multiple of 2π, so

$$(2\pi/\lambda)(4(r+\varepsilon)+\rho^4/r^3) = 2m\pi, \; m \text{ is an integer} \tag{3.127}$$

Then

$$\varepsilon = m\lambda/4 - r - \rho^4/4r^3 \tag{3.128}$$

In the confocal condition, $m\lambda/4 = r$, in order to keep maximum transmission, the relationship between the change of cavity length $\Delta\varepsilon$ and the change of the center transmission frequency is

$$\Delta\varepsilon = m\frac{\Delta\lambda}{4} = m\frac{\lambda_0^2}{4c}\Delta\nu = r\frac{\lambda_0}{c}\Delta\nu \tag{3.129}$$

According to the requirement of frequency tracking error presented in section 3.2,

$\Delta\nu$ should be less than 60MHz. So the tracking error of CFPI cavity length should be less than 2.1nm.

3.4.3 The method of frequency-locking used in high spectral resolution system

In order to keep the center frequency of the spectral resolution system following the frequency of laser transmitter in a HSRL, several methods can be used. First, both the wavelength of the laser transmitter and the center transmitted wavelength of the receiver is stabilized to a saturable molecular absorption line. Second, the frequency of the laser transmitter is stabilized to a saturable molecular absorption line and the spectral resolution receiver is locked to the laser frequency by a feedback control system. Third, the spectral resolution receiver is locked to the laser frequency by tracking the change of laser frequency directly. As introduced in chapter 2, saturable molecular absorption is not well suitable to space conditions. So the third solution is selected in this spaceborne HSRL.

The laser used in this spaceborne HSRL employs a 1kHz pulsed seed laser for amplifying to high power 20Hz pulse laser in order to enhance the stability. The narrow bandwidth seeder has been fully characterized in terms of output power and stability, temporal behavior, spectral bandwidth and tunability. The chosen 1 kHz repetition rate allows for single pulse amplification with no need of pulse picking. The laser system comprises 5 different stages: a narrow bandwidth oscillator (1 kHz), a CW pre-amplifier (1 kHz), a pulsed amplifier (20 Hz) followed by a booster (20 Hz) and a final second harmonic generation stage [41].

Two different laser output ports are available: a seed laser output port and the main laser output port. The 1064 nm radiation from the seed laser port has 1 kHz repetition rate with a 1 mm diameter beam, 5mW power and horizontal polarization. The main laser output provides radiation at two wavelengths, 1064 nm and 532 nm, at 20 Hz repetition rate. Both the beams are expected to have 20 mm diameter, 110mJ pulse energy and linear polarization.

Due to the 1kHz pulse seed laser frequency, sideband locking method is not well suitable due to the complex frequency modulation of the pulse laser. Therefore, piezoelectrical tuning method has been used in this HSRL. A frequency locking servo

has been developed to control the length of the CFPI based on the 1064 nm seed laser such that it is resonant at the desired second harmonic wavelengths of 532nm. Because 532 nm light have double the frequency of 1064 nm light, if the CFPI cavity is resonant at 1064 nm, it will also be resonant at 532nm assuming the use of ideal mirrors. The basic layout for the frequency- locking is as follows

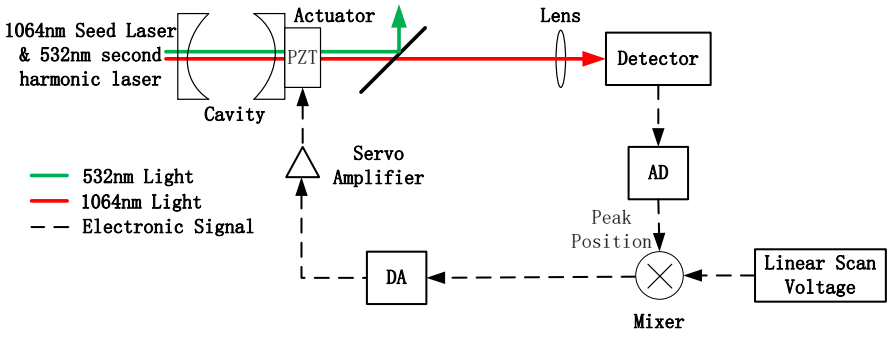

Figure 3.25 The basic layout for locking a cavity to a laser. 1064nm is the 1kHz locking pulse light and 532nm is the 20Hz second harmonic pulse light. In the interval of two adjacent 532nm pulses, 1064nm pulse is used to find the peak position by scanning the piezo actuator. When the next 532nm pulse is coming, the cavity length is set to the voltage at the transmitted peak.

3.4.4 The design of frequency-locking subsystem

3.4.4.1 The design of the reflectivity of CFPI mirrors

In order to improve the frequency-locking accuracy at 532nm, the finesse at 1064nm is designed 5 times higher than the finesse at 532nm. So the reflectivity of the cavity mirrors at 1064nm is 93.9%. This means that the reflectivity is different with the reflectivity at 532nm. The transmission of the CFPI mirrors is shown in Figure 3.26

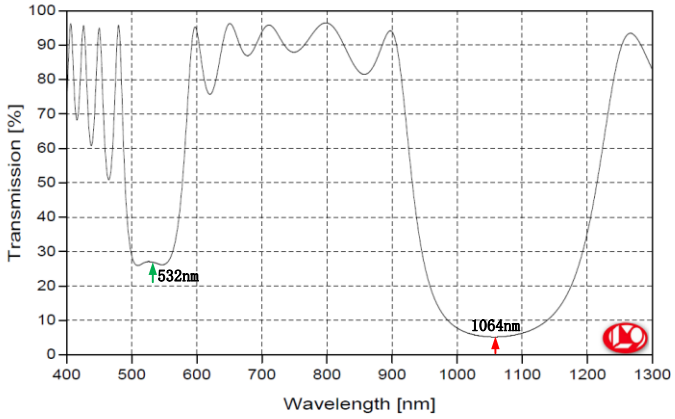

Figure 3.26 The transmission of the CFPI mirror's coating.

When ideal mirrors are used, the transmission and reflection of the CFPI at 532nm and the transmission of the CFPI at 1064nm for the fundamental mode TEM_{00} are shown in Figure 3.27

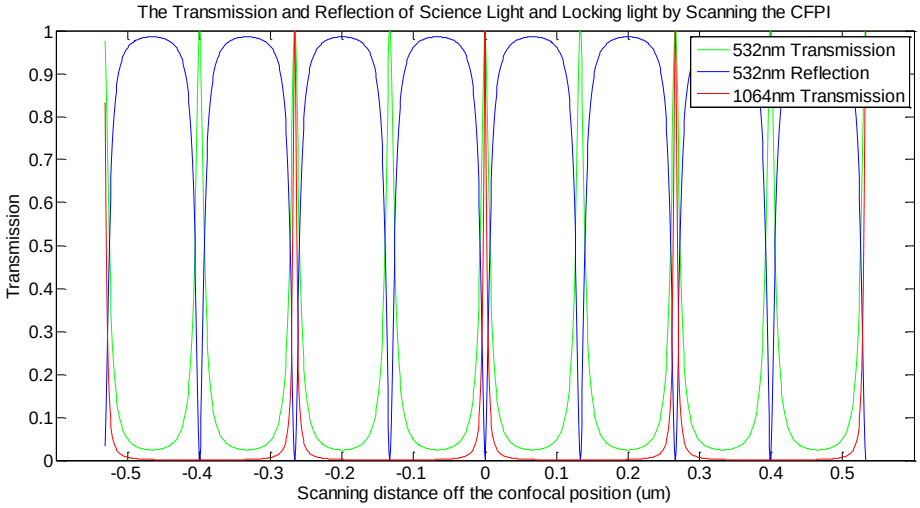

Figure 3.27 The transmission and reflection of the CFPI at the wavelength of 532nm and the transmission at the wavelength of 1064nm for the fundamental mode TEM_{00}.

3.4.4.2 The selection of piezo actuator, controller and frequency locking electronics

According to the requirements of frequency-locking subsystem presented in section 3.4.2, the model of piezo actuator S-310.10 from Physik Instrumente (PI) GmbH has been selected. The main parameters of S-310.10 is introduced in Table 3.5

Table 3.5 The Specifications of S-310.10 Piezo Actuator

Parameters	Value	Units
Active axes	Z	
Open-loop linear travel@0 to 100V	6	um ±20%
Open-loop linear resolution	0.1	nm
Diameter (max.) of mounted mirrors	25	mm
Clear Aperture	10	mm
Unloaded resonant frequency (f_0)	9.5	kHz ±20%
Resonant frequency w/Ø15 x 4 mm glass mirror	6.5	kHz ±20%
Resonant frequency w/Ø 20 x 4 mm glass mirror	6.1	kHz ±20%

Distance, pivot point to platform surface (T)	0	mm
Material (case/platform)	N-S/N-S	
Length (L)	19.5	mm
Weight (w/o cables)	45	g ±5%

Table 3.5 shows that: the resolution is 0.1nm (about 1/20 of the resolution requirement); the travel range is 6um (about six times of the required scanning range). So the resolution and the range of piezo actuator meet the requirements of frequency-locking subsystem.

The maximum operating frequency of a piezo actuator depends on its mechanical resonant frequency. To estimate the effective resonance frequency of a piezo actuator (platform + payload), the moment of inertia of the payload must also be considered. Moment of inertia of a rotationally symmetric payload (e.g. round mirror) is as follows [42]:

$$I_M = m\left[\frac{3R^2 + H^2}{12} + \left(\frac{H}{2} + T\right)^2\right] \tag{3.130}$$

where,

m = Payload Mass [g]

I_M = Moment of inertia of the payload [g ٠mm^2]

H = Payload thickness [mm]

T = Distance, pivot point to platform surface [mm]

R = Payload radius [mm]

Using the resonant frequency of the unloaded platform and the moment of inertia of the payload, the system resonant frequency is calculated according to the following equation:

$$\mathrm{f}' = \frac{\mathrm{f}_0}{\sqrt{1 + \mathrm{I_M}/\mathrm{I_0}}} \tag{3.131}$$

where,

f' = Resonant frequency of platform with payload [Hz]

f_0 = Resonant frequency of unloaded platform [Hz]

I_0 = Moment of inertia of the unloaded platform [g·mm^2]

I_M= Moment of inertia of the payload [g·mm^2]

The dimension of the plano-concave CFPI mirror is Ø25×9.5mm (r = -20 mm) and the density of Suprasil material is 2.201 g/cm^3. The resonant frequency of the piezo actuator and CFPI mirror meets the requirement of 1kHz.

Analog Devices EVAL-ADUC7126QSPZ has been selected for the frequency locking electronics. The specifications of EVAL-ADUC7126QSPZ is introduced in the following table:

Table 3.6 The Specifications of EVAL-ADUC7126QSPZ

Parameters	Value
Chip	ADuC7126
Core Processor	ARM7TDMI, 32-bit
Core clock	41.78 MHz
ADC	
Resolution	12-bit
Input Voltage Range	0-2.5V
Sampling Rate	1 MSPS
DAC	
Resolution	12-bit
Output Voltage Range	0-2.5V
Relative Accuracy	±2 LSB (LSB = 2.5V/2^{12}=0.61mV)
Memory	126 kB Flash, 32 kB SRAM
Vectored interrupt controller	Interrupt on edge or level external pin inputs
On-chip peripherals	2×I2C, 2×UART, Up to 40 GPIO, 4× general-purpose timers

Since the DAC output voltage range (0 - 2.5V) is smaller than the input voltage range of the piezo actuator (0 - 100V), a piezo amplifier module has been used. The piezo amplifier module has ten times magnification. So the piezo position precision depending on the DAC relative accuracy is 0.73nm and meets the precision

requirement of the CFPI cavity length.

3.4.4.3 The algorithm design for the frequency locking subsystem

In order to obtain high stability and accuracy, a two-stage (searching stage and tracking stage) frequency-locking method has been used. The timing diagram of this method is shown in Figure 3.28.

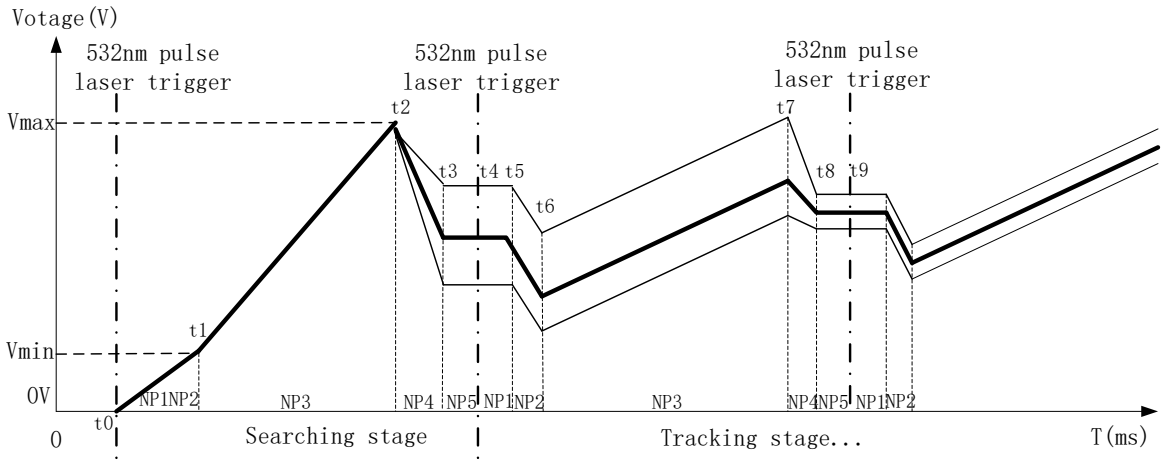

Figure 3.28 The timing diagram of two-stage frequency-locking method. The 532nm pulse trigger from the 532nm 20Hz science pulse laser and the NP1, NP2, NP3, NP4, NP5 are the pulse numbers of the 1064nm 1kHz locking laser. NP1+NP2+NP3+NP4+ NP5 = 50.

The time is set to t_0 when the 532nm laser trigger output pulse is generated. Then it starts the searching stage and the output voltage from the DAC output port of frequency-locking electronic board goes to the minimum value of the scanning voltage V_{min}. The time interval from t_0 (0 V) to t_1 (V_{min}) equals to NP1+NP2 milliseconds. Then the linear scan of the cavity length starts and the voltage is scanned from V_{min} to V_{max} and in NP3 milliseconds. During this period, the peak position of the transmitted signal in the 1064nm locking channel is calculated and the peak near the middle of the scanning range is selected. Then the DAC output voltage is transferred to the voltage where there is the selected transmission peak in NP4 milliseconds. In the next NP5+NP1 milliseconds, the voltage is maintained constant and the tracking stage is started at the arrival of the next 532nm laser trigger pulse.

In the tracking stage, the scanning voltage range becomes 1/4 of the searching voltage range and the duration is the same with searching stage to improve the accuracy of peak positions. The center value of the scanning voltage is the voltage

which is maintained for NP5+NP1 milliseconds in the previous cycle. During the scanning period, the peak position of the transmitted signal in 1064nm locking channel is calculated again and the DAC output voltage goes to the voltage corresponding to the transmission peak. Then the voltage is maintained for NP5+NP1 milliseconds and this period is used for collecting the 532nm light backscattered by atmospheric molecules and aerosols. Then the tracking cycle is repeated until the tracking voltage is lower than V_{min} or higher than V_{max} .

The flow chart of frequency-locking algorithm is shown in Figure 3.29.

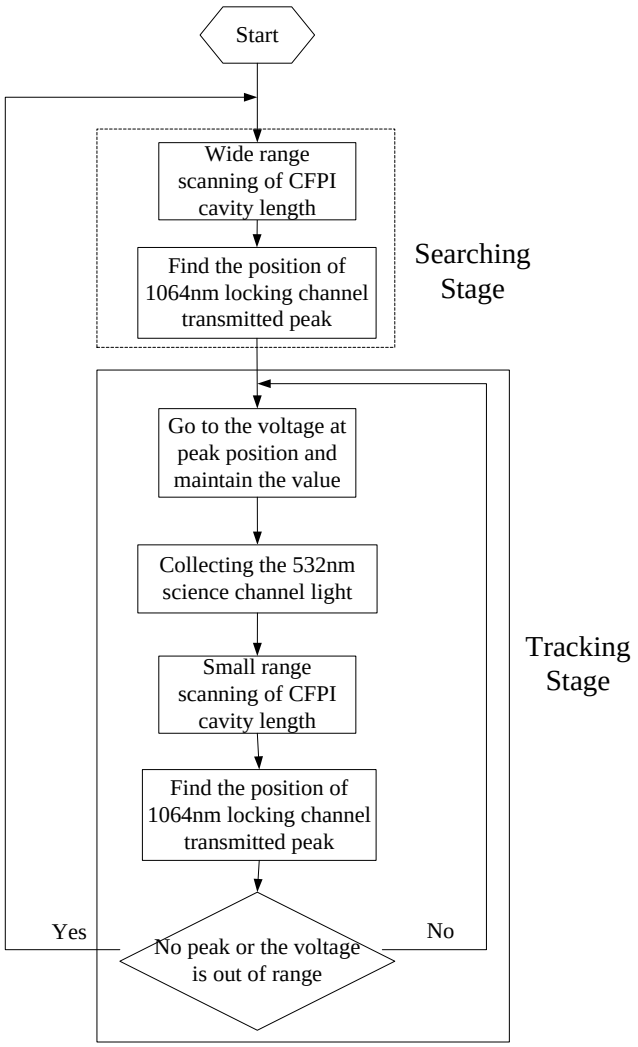

Figure 3.29 The flow chart of the frequency-locking algorithm.

The values NP1, NP2, NP3, NP4, NP5 are set as 3, 6, 32, 6, 3. The scanning voltage range in searching stage is 1.25V (V_{max} - V_{min}) and the scanning voltage range in tracking stage is 0.3125V.

4 Realization and test of the spectral analysis system

4.1 The realized spectral analysis system

The main components of the spectral analysis system, including the mirrors and mounts of background Fabry-Perot interferometer filter (PFPI) and high spectral resolution Fabry-Perot interferometer filter (CFPI), had been manufactured and assembled. Photographs of the PFPI and CFPI are shown in Figure 4.1 and Figure 4.2, respectively.

a) 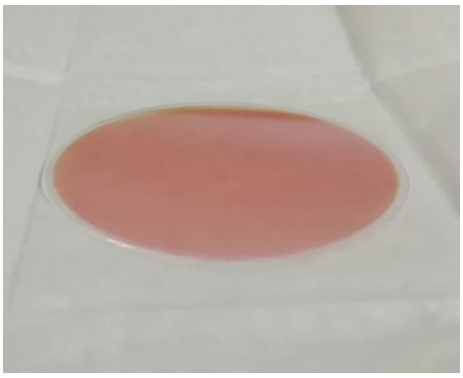 b) 

Figure 4.1 The PFPI mirror and it's mount with a temperature controller. a) The unmounted PFPI mirror; b) the mount with a temperature controller.

a) 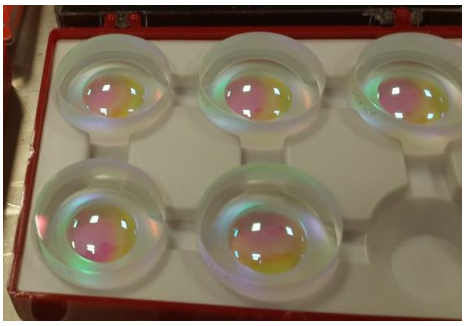 b) 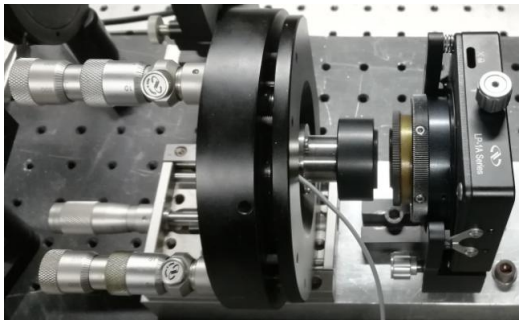

Figure 4.2 CFPI cavity mirrors and mount with a piezo actuator. a) Concave reflective mirrors with dual-wavelength reflective coating; b) CFPI cavity. One mirror mounted on a piezo actuator and the combination is mounted on a two-axis gimbal optical mount. The gimbal mount is mounted on a linear translation stage with rear-mounted micrometer. The other mirror is mounted on a 5-axis XYZ $\theta_X \theta_Y$ lens positioner.

The optical train of the spectral analysis system includes both the 532nm science train and the 1064nm frequency-locking train. The optical trains are shown in Figure 4.3

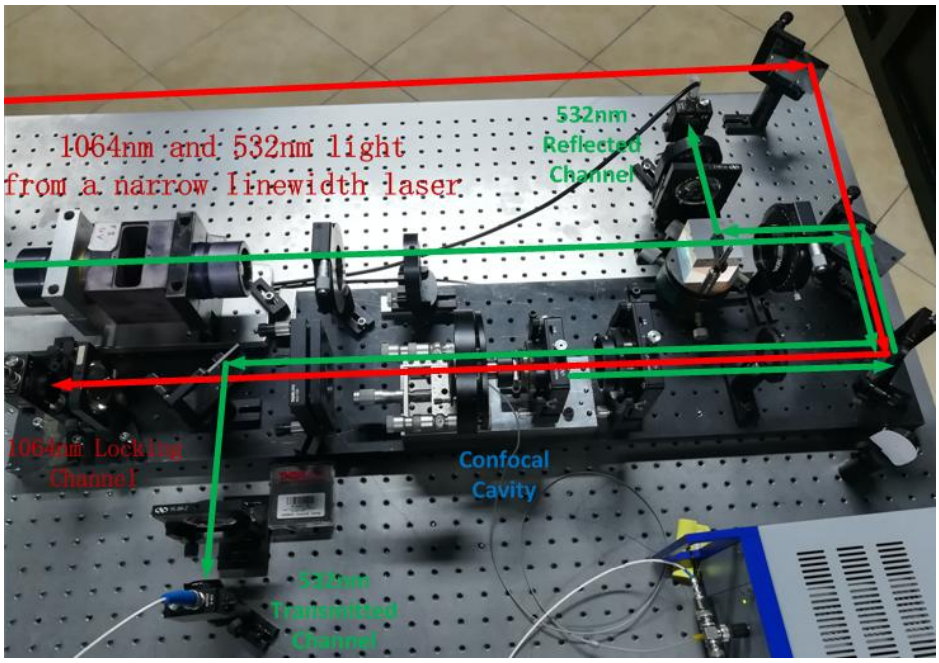

Figure 4.3 Optical trains of the spectral analysis system. The green lines represent the optical train of 532nm science channels, while the red lines represent the optical train of the 1064 nm frequency-locking channel. The PIN detectors in 532nm science channels will be replaced with PMTs in the prototype of spaceborne HSRL.

The 532nm optical train includes a half-wave plate, a narrowband interference filter, a planar Fabry-Perot interferometer (PFPI, not mounted on the optical bench in Figure 4.3), a polarizing cube beamsplitter, a quarter-wave plate, a matching lens and a confocal Fabry-Perot interferometer (CFPI). The 532nm backscattered light is separated to the transmitted channel and reflected channel by the 532nm optical train. The 1064nm optical train is used to lock the center transmission wavelength of CFPI to the wavelength of the 1064nm seed laser source.

4.2 The performance measurement of the CFPI

4.2.1 The setup for the performance measurement

The setup of the performance measurement of CFPI is shown in Figure 4.4.

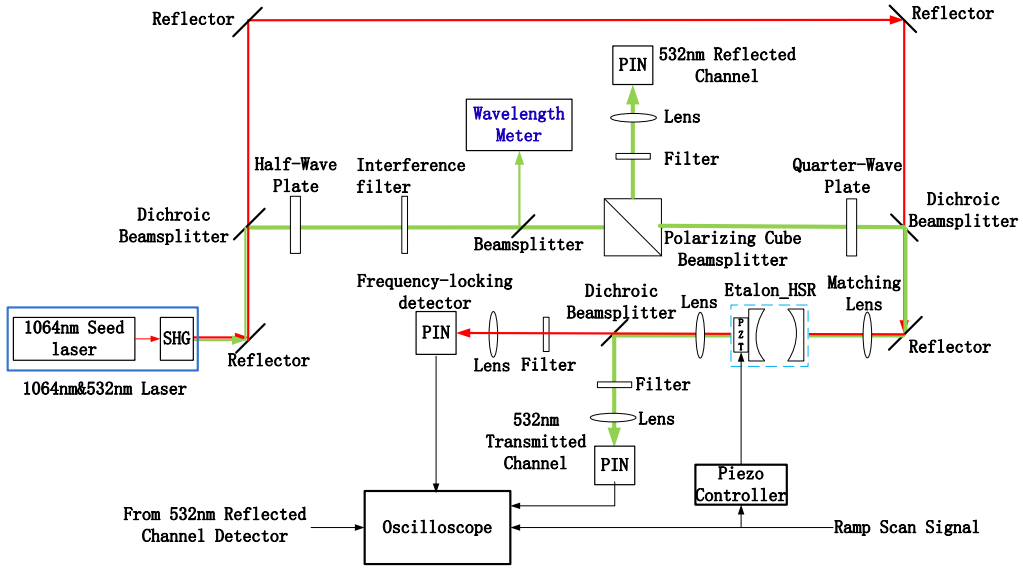

Figure 4.4 The setup of the performance measurement. A 1064nm narrow linewidth laser and a second harmonic generator are used to generate dual-wavelength laser. The 1064nm light is used to lock the CFPI and the 532nm light is used to test the transmission and reflection of the CFPI at 532nm working wavelength. The signal generator has been used to generate a ramp signal for piezo controller to scan the CFPI cavity distance. The oscilloscope is used to monitor the scan signal and the signals detected by the 532nm transmitted channel and reflected channel detectors, and also the signal detected by the 1064nm frequency-locking channel detector.

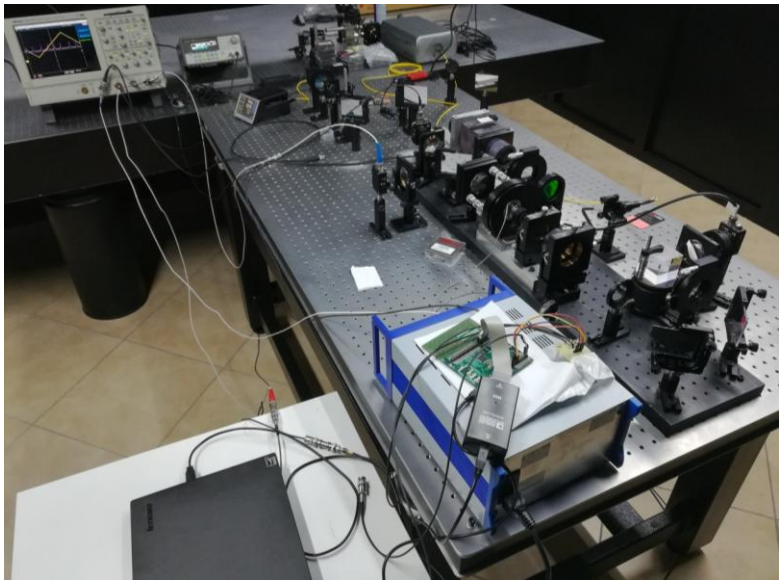

Figure 4.5 The optical bench test setup of the realized spectral analysis system.

The laser used for the tests of spectral analysis system was a narrow linewidth 1064nm continuous semiconductor laser diode with a second harmonic generator (KTP crystal). The schematic diagram of the laser is shown in Figure 4.6.

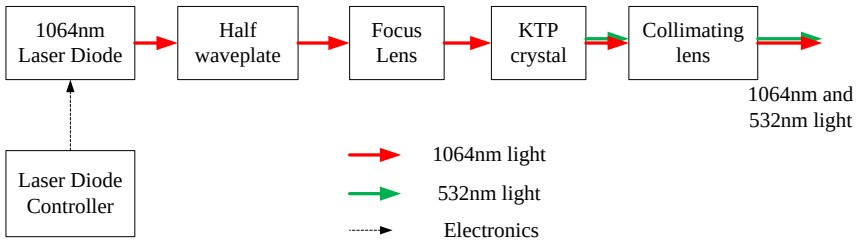

Figure 4.6 The schematic diagram of the laser used for CFPI tests.

The model of the 1064nm laser diode in Figure 4.6 was QFBGLD-1060-30PM from QPHOTONICS, LLC and the specifications are shown in Table 4.1.

Table 4.1 The specifications of 1064nm laser diode.

Parameter	Value	Units
Internal Temperature	25	℃
Thermistor Resistance	10.0	kΩ
Optical Output Power	30	mW
Threshold Current	60	mA
Operating Current	220	mA
Operating Voltage	1.9	V
Monitor Current	0.17	mA
Monitor Dark Current	0	nA
Center Wavelength	1064.26	nm
Spectral Width	<0.01	nm

The Laser Diode Controller (LDC 1300) used for the 1064nm laser diode is from Covega Corporation. It is based around a small-form-factor current source and thermo-electric controller designed to drive the laser diode. The wavelength of the laser diode can be tuned by temperature and drive current. In the tests of the spectral analysis system, the temperature had been set to 23.7℃ and drive current had been set to 144mA. In these cases, the output power of the 1064nm laser diode is 27.4mW and the wavelength after second harmonic generator is 531.99676nm, which was

measured by a WS7 wavelength meter from HighFinesse GmbH. The diameter of output laser beam was 5mm at 532nm and 20mm at 1064nm.

The model of PIN detectors used in the tests was DET36A/M from Thorlabs. The TDS 5054 digital oscilloscope from Tektronix was used to monitor the scanning signal and the output signal from 532nm transmitted channel detector, 532nm reflected channel detector and 1064nm frequency-locking channel detector. The 33250A signal generator from Agilent was used to generate a ramp scan signal.

4.2.2 The performance measurement of the CFPI

1) The peak transmission and reflection of the CFPI at 532nm

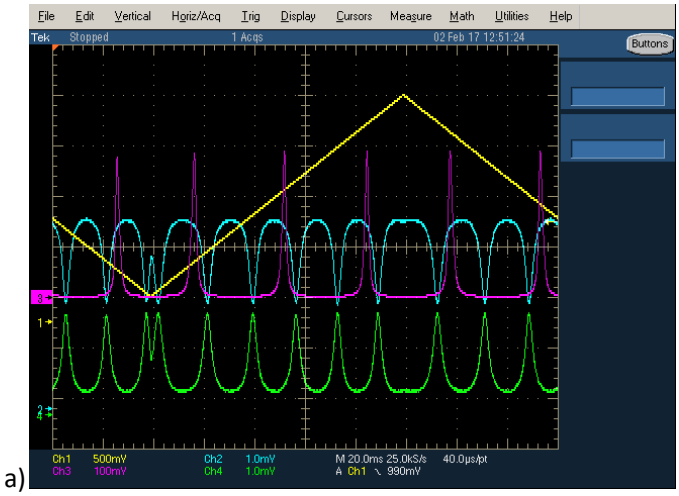

a)

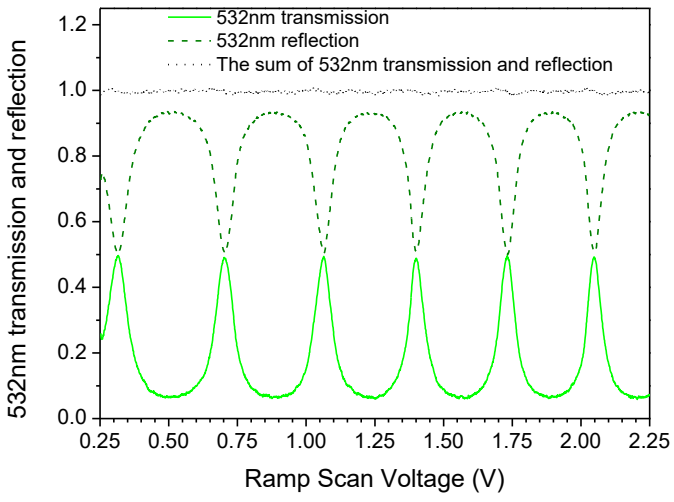

b)

Figure 4.7 Transmitted and reflected signals when the length of CFPI cavity is scanned. a) The transmitted and reflected signals displayed on the oscilloscope when the CFPI cavity length is scanned. The yellow line is the ramp scan signal from signal generator; the purple line is the transmitted signal from 1064 frequency-locking

channel PIN detector; the green line and the cyan line are the transmitted and reflected 532nm science channel signals, respectively. b) A plot of CFPI transmission and reflection at 532nm while the cavity length is scanned by a ramp scan voltage.

The peak transmission is measured by the transmission profile shown in Figure 4.7. The measured value of the peak transmission is 0.492.

2) The bandwidth of the CFPI transmission at 532nm

a)

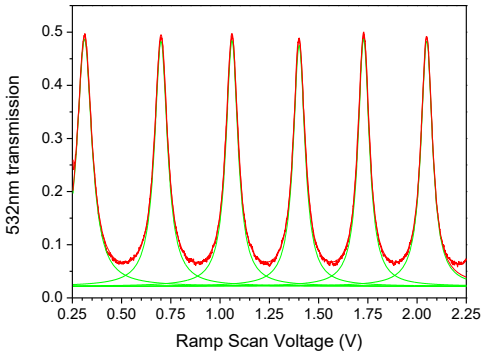

b)

Peaks

	Area	Center	Width	Height
1	0.06606	0.31124	0.09045	0.5827
2	0.05658	0.70011	0.07819	0.57736
3	0.05295	1.06032	0.07291	0.57949
4	0.05039	1.4013	0.07076	0.56829
5	0.04983	1.72888	0.06817	0.58322
6	0.05096	2.04916	0.07038	0.57779

Statistics

DF	2481
COD (R^2)	0.99806
ReducedChiSq	3.47099E-5

Figure 4.8 A plot of 532nm transmission (red) and it's Lorentzian fitting curve (green) while CFPI is scanned. a) 532nm transmission (red) and Lorentzian fitting curve (green); b) The Lorentzian fitting result.

The results of the Lorentzian fitting show that the R-Square (COD) is 0.99806, so the transmission profile of the CFPI at 532nm is consistent with multi-peak Lorentzian curve. The measured results of the distance between adjacent peaks, the width of the transmission profile and the finesse are shown in Table 4.2.

Table 4.2 The Lorentzian fitting results and the calculated finesses of the CFPI.

	Distance between adjacent peaks (V)	Width of the peak (V)	Finesse
1	0.38887	0.07819	4.97
2	0.36021	0.07291	4.94
3	0.34098	0.07076	4.82
4	0.32758	0.06817	4.80
5	0.32028	0.07038	4.55

The average value of the finesse $\mathcal{F}^*$ is 4.82 and the standard deviation is 0.16. According to the free spectral range

$$FSR = c/4r = 3.75\text{GHz}$$

The bandwidth (FWHM) of the CFPI is calculated by

$$W_{FWHM} = \frac{FSR}{\mathcal{F}^*} = 0.78\text{GHz}$$

And the standard deviation of the bandwidth is 0.041GHz according to the standard deviation of the finesse.

3) The bandwith of the CFPI transmission at 1064nm

a)

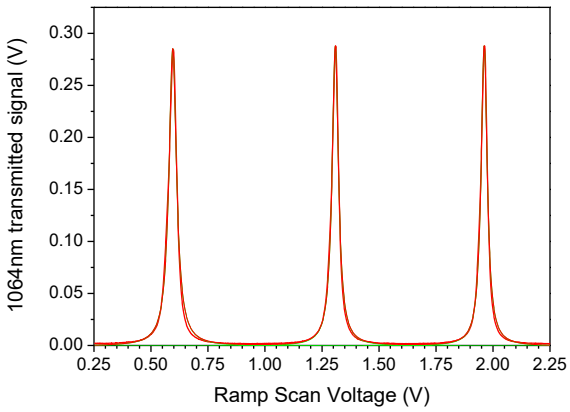

b)

Parameters

	Value	Error
y0	-7.27581E-4	8.89564E-5
xc1	0.59554	5.85185E-5
w1	0.0401	1.71778E-4
A1	0.01802	5.66921E-5
xc2	1.30845	5.31726E-5
w2	0.03369	1.55426E-4
A2	0.01527	5.14757E-5
xc3	1.96138	5.21758E-5
w3	0.03248	1.52151E-4
A3	0.01473	5.03504E-5

Peaks

	Area	Center	Width	Height
1	0.01802	0.59554	0.0401	0.35849
2	0.01527	1.30845	0.03369	0.36165
3	0.01473	1.96138	0.03248	0.36184

Statistics

DF	2490
COD (R^2)	0.99533
ReducedChiSq	1.37341E-5

Figure 4.9 A plot of 1064nm transmission (red) and it's Lorentzian fitting curve (green) while CFPI is scanned. a) 1064nm transmission (red) and Lorentzian fitting curve (green); b) The Lorentzian fitting results.

Fitting results show that the distance between adjacent peaks is 0.713V and the width of the peak is 0.0337V, so the finesse of the CFPI at 1064nm is 0.713V/0.033V = 21.2. Therefore, the bandwidth of the CFPI transmission at 1064nm is

$$\Delta\nu = c\frac{\Delta\varepsilon}{2r\lambda_0} = 0.28\text{GHz}$$

4) The shift of the transmission peak between 532nm and 1064nm

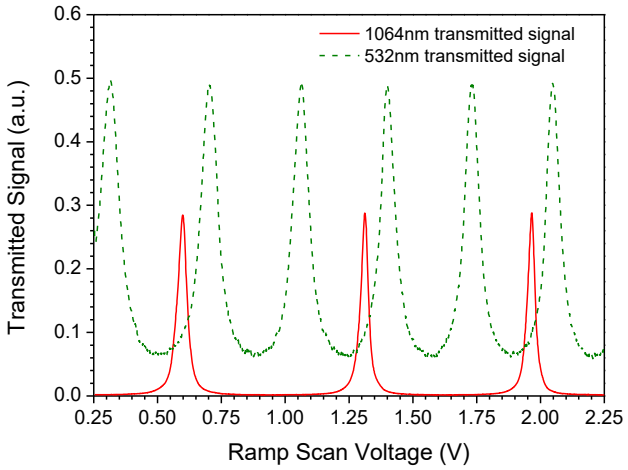

Figure 4.10 A plot of the shift between the 532nm and 1064nm transmission peaks when CFPI is scanned.

The value of the observed shift between 1064nm transmitted peak and 532nm transmitted peak is 0.093V. According to the relation between the measured distance of adjacent peaks and the multimode free spectral range at 1064nm, the length difference of CFPI between 532nm and 1064nm is 34.7nm. This length difference is used as an offset in the frequency-locking subsystem.

4.3 The measurement of the CFPI dispersion for analyzing the stability of the peak shift between 532nm and 1064nm transmitted signals

When ideal mirrors are used, if the CFPI cavity is resonant at 1064 nm, it should be also resonant at 532nm because 532 nm light is the second harmonic light of the 1064nm light. However, dispersions caused by the reflective coatings of the CFPI cavity mirrors and the non-vacuum conditions in the cavity make the cavity length different for the 532nm light and the 1064nm light. The transmission peaks at the different wavelengths therefore do not line up exactly. The stability of the transmission peak shift between 532nm and 1064nm signals transmitted by the CFPI will affect the frequency-locking accuracy at 532nm due to the use of 1064nm seed laser for locking the CFPI. In order to verify the influencing factors of the peak shift and evaluate the stability of the peak shift, an experiment has been performed. The experiment employs planar cavity mirrors to replace the CFPI concave mirrors in order to measure the peak shifts at different cavity separations. The planar mirrors

have the same coating with CFPI mirrors. The setup of the dispersion measurement is shown in Figure 4.11.

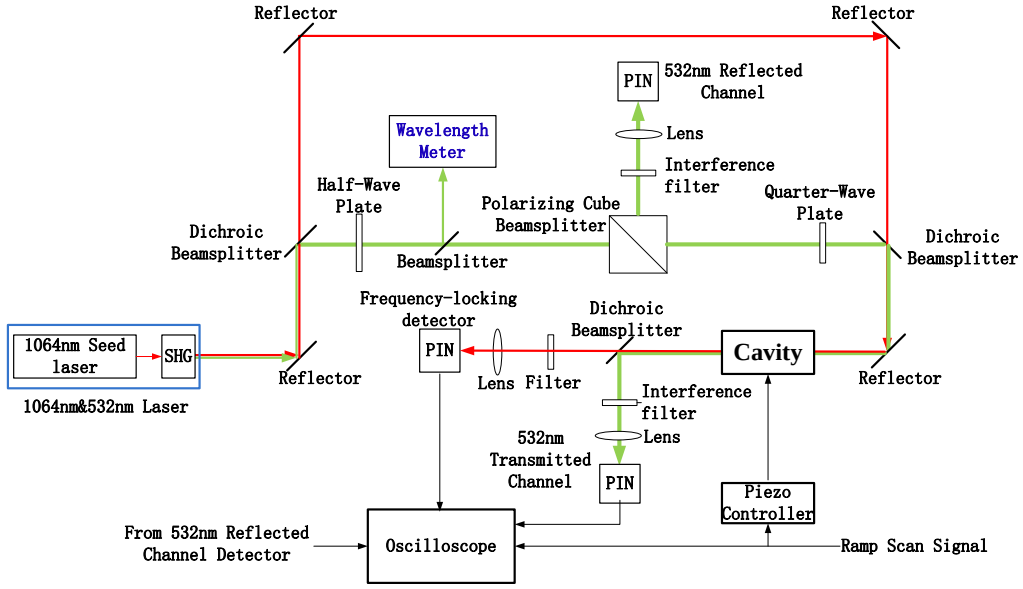

Figure 4.11 The setup of the dispersion measurement. The setup is the same with Figure 4.4 except the cavity mirrors which is replaced by planar mirrors with the same coating.

In the above figure, planar cavity mirrors are used to replace the CFPI concave mirrors in Figure 4.4. The other part is the same with Figure 4.4. A 1064nm narrow linewidth laser and a second harmonic generator are used to generate a dual-wavelength laser. The distance of the two cavity mirrors can be changed by a linear translation stage with a rear-mounted micrometer. A signal generator has been used to generate a ramp signal for piezo controller to scan the cavity distance with sub-nanometer precision in several micrometers range. In this experiment, the shift between the 1064nm transmission peak and the adjacent 532nm transmission peak had been measured at six cavity lengths. The signals at the biggest length and the peak shifts at the six separation distances are shown in Figure 4.12.

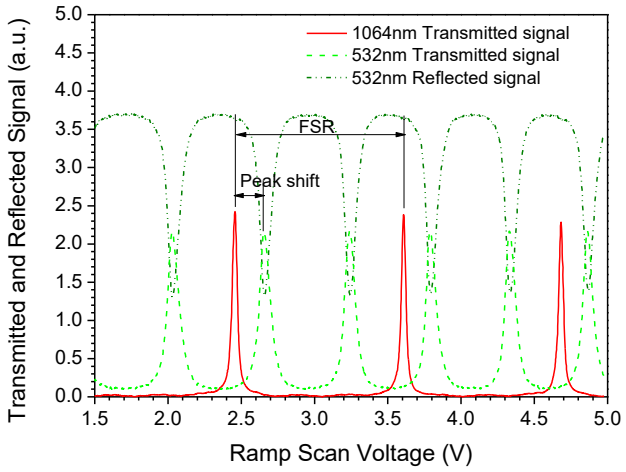

a)

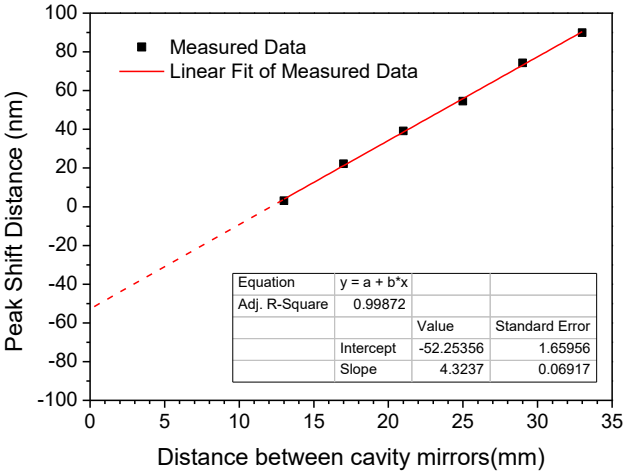

b)

Figure 4.12 The results of the dispersion measurement. a) The signal at the biggest separation of the cavity mirrors when the cavity distance is scanned. The voltage differences corresponding to the peak shift and FSR at 1064nm line are measured by the 1064nm transmitted signal and 532nm transmitted signal. b) The peak shifts at the six separation distances of the planar cavity.

Figure 4.12b shows that the peak shift distance has a linear relation with the planar cavity distance. The slope of the fit line is 4.3237×10^{-6}. According to the updated Edlén equation [43], the refractive-index difference between 532nm and 1064nm is 4.2202×10^{-6} for air at an ambient temperature of 15℃ and a pressure of 101.325 kPa. Therefore, the measured result is consistent with the theoretical calculation of air dispersion. This means that the air dispersion is one of the influencing factors of the peak shift. The non-zero value of the intercept of fit line

proves that the coating dispersion is another influencing factor of the peak shift. According to the fit line, the peak shift at the planar cavity distance of 20mm is 34.2nm. This is consistent with the measured peak shift when using CFPI concave mirrors, which is presented in section 4.2.2. Therefore, both the air and coating dispersion are the influencing factors of the peak shift between 532nm and 1064nm transmitted signals in the spectral analysis system. As the air dispersion is dependent on the air temperature and pressure, the peak shift is also dependent on the air temperature and pressure. The peak shift error caused by the change of the air temperature and pressure will make CFPI cavity be locked to a position that deviates from the 532nm transmission peak. Therefore, the control or measurement of the air temperature and pressure in the CFPI must be done for eliminating or compensating the effect of air temperature and pressure changes in order to maintain the measurement accuracy of the HSRL.

4.4 Test of the frequency-locking subsystem

4.4.1 Test setup of the frequency-locking subsystem

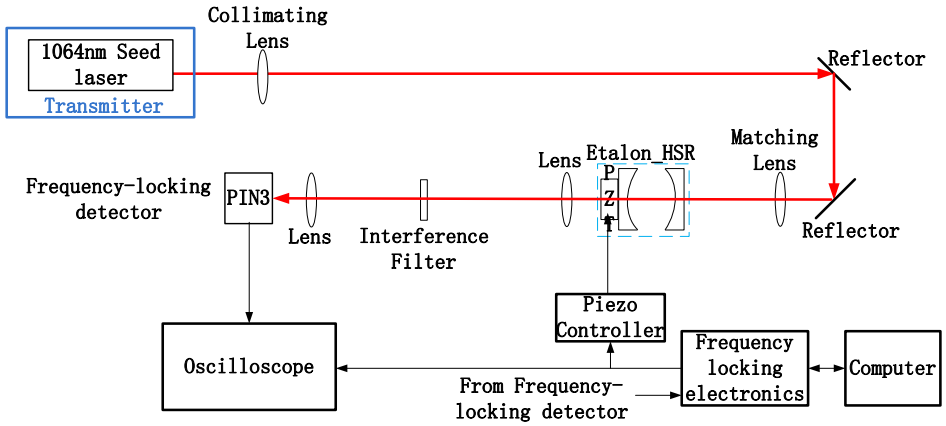

Figure 4.13 The test setup of frequency-locking subsystem.

Figure 4.13 shows the test setup of frequency-locking subsystem. Compared to Figure 4.4, the signal generator is replaced by the frequency-locking electronics. The functions of the frequency-locking electronics include the generation of the ram scan signal, the acquisition of the signal from detector PIN3 and the computing platform for the frequency-locking algorithm. The computer is used to record the data from the frequency-locking electronics.

4.4.2 The test of the switch between the searching and tracking stages

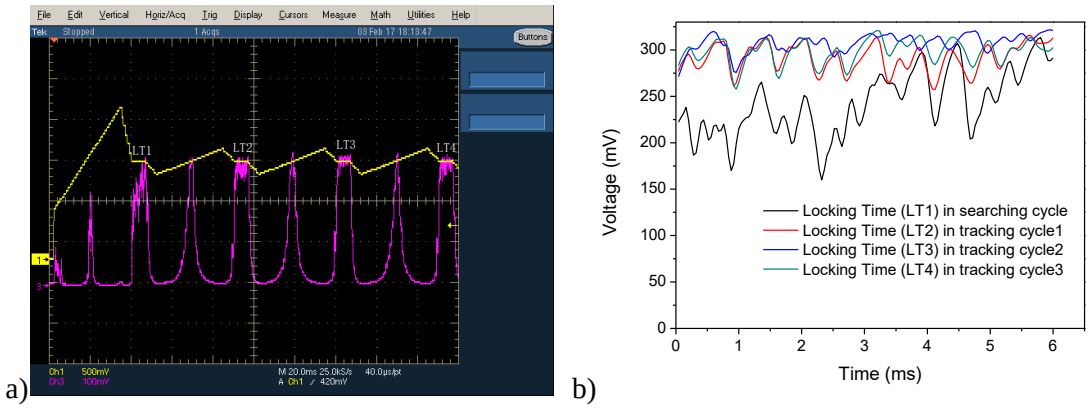

a) b)

Figure 4.14 The signals in the searching and tracking stage of the frequency-locking subsystem. a) The switch from the searching stage to the tracking stage. Yellow signal represents the scan voltages from the frequency-locking electronic board to the piezo controller. The first cycle is the searching cycle and the next three cycles are tracking cycles. The purple signal is the 1064nm transmitted signal for frequency-locking. b) The 1064nm transmitted signal during the locking period. The colors represent the four cycles displayed in the left figure.

The mean value and standard deviation of the transmitted signal during the locking time in searching stage is 0.242 and 0.035, respectively. So, the relative error of the transmission in searching stage is 14%. The mean value and standard deviation of the transmitted signal during the locking time in the tracking stage are 0.299 and 0.01, respectively. So, the relative error of the transmission in tracking stage is 3.3%. By using the two-stage method, the frequency-locking precision is 4.2-fold improved compared to only use searching stage method.

4.4.3 The test of tracking accuracy at 1064nm

Figure 4.15 The 1064nm transmitted signals in the tracking stage when the CFPI is

locked to the 1064nm laser. Yellow signal represents the scan voltages from the frequency-locking electronic board to the piezo controller. The purple signal is the 1064nm transmitted signal of the CFPI.

The mean value of the transmitted signal during the locking period (the plateau of the purple signal) is 211mV and the standard deviation is 3.1mV. So, the relative error of transmission is 1.47%. According to the transmission expression (3.124) and the measured finesse of the CFPI at the wavelength of 1064nm, the displacement between the position at the transmission peak and the position corresponding to a value 1.47% lower than the peak transmission is 1.1nm. This meets the requirement of tracking precision of CFPI cavity length.

4.5 Test of the spectral analysis system under the frequency-locking condition

4.5.1 The test setup of the spectral analysis system

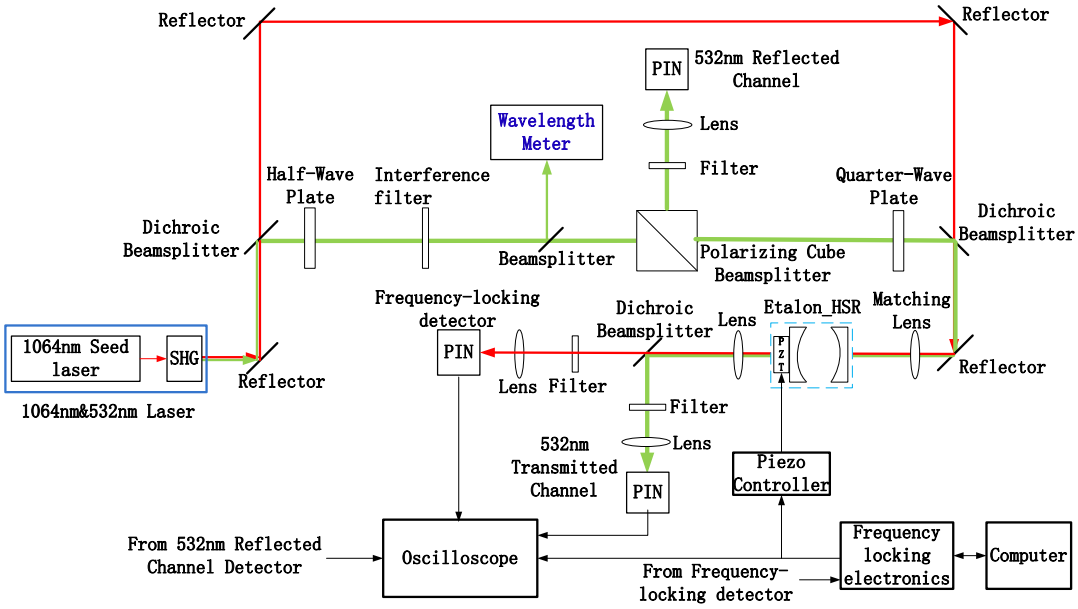

Figure 4.16 Test setup of the spectral analysis system.

Figure 4.16 shows the test setup of the spectral analysis system. Compared to Figure 4.4, the signal generator is replaced by the frequency-locking electronics. Compared to Figure 4.13, dual-wavelength laser is used in this figure. The offset presented in section 4.2.2 has been used in the frequency-locking program to make the center wavelength of CFPI cavity lock with the wavelength of 532nm light during the locking time.

4.5.2 Measurements of transmission and reflection of the spectral analysis system

a) 

b) 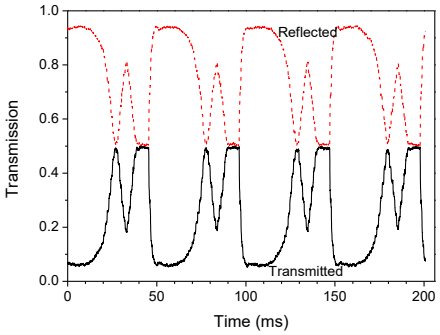

Figure 4.17 The transmitted and reflected signals at 532nm and 1064nm in the tracking stage. a) A photo of transmitted and reflected signal in the tracking stage. The yellow line is the scanning signal from frequency-locking electronic board; the purple line is the transmitted signal from 1064 locking channel PIN detector; the green line and the cyan line are the transmitted and reflected 532nm science channel signals, respectively. The plateau in the zoom figure corresponds to the locking time and the 532nm backscattering light will be received during this period. b) The transmission and reflection of the CFPI at 532nm. The transmission and reflection are obtained from the transmitted and reflected 532nm signals in the left figure. The red dash line represents the reflection and the black solid line represents the transmission.

From the data corresponding to Figure 4.17b, the mean value of the peak transmission and reflection are 0.49 and 0.51, respectively. The transmission is just slight different with the measured peak transmission presented in section 4.2.3, so the center transmission wavelength of the CFPI is accurately locked to the wavelength of 532nm light.

4.5.3 Short-term stability of the spectral analysis system

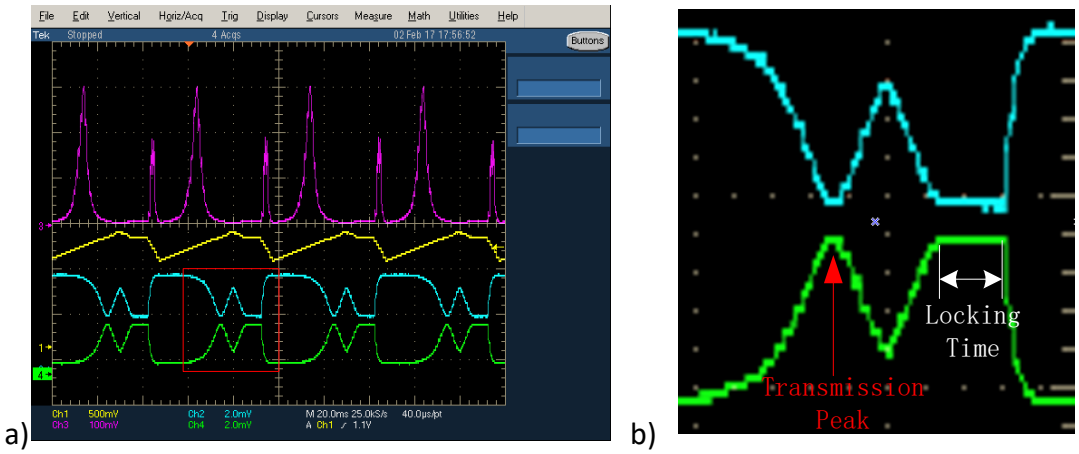

Figure 4.18 A photo of transmitted and reflected signals in the tracking stage. a) Signals on the oscilloscope in the tracking stage; b) zoom of signals in the locking time. The yellow line is the scan signal from frequency-locking electronic board; the purple line is the transmitted signal from 1064 locking channel PIN detector; the green line and the cyan line are the transmitted and reflected 532nm science channel signals , respectively. The plateau in the zoom figure corresponds to the locking time and the 532nm science light will be received during this period.

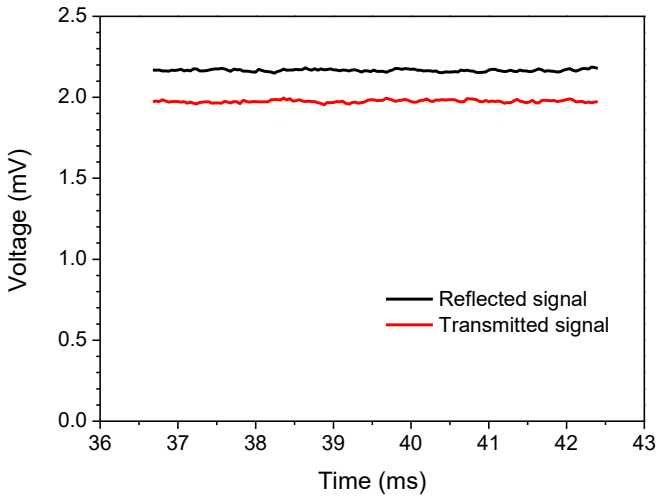

Figure 4.19 Short term stability of the transmission and reflection at the wavelength of 532nm.

The mean values of the transmitted and reflected signals are 1.976mV and 2.167mV, respectively, and the standard deviations of transmitted and reflected signals are 0.008mV and 0.0072mV. So, the relative errors of transmission and reflection are 0.4% and 0.33%, respectively.

4.5.4 Long-term stability of the spectral analysis system

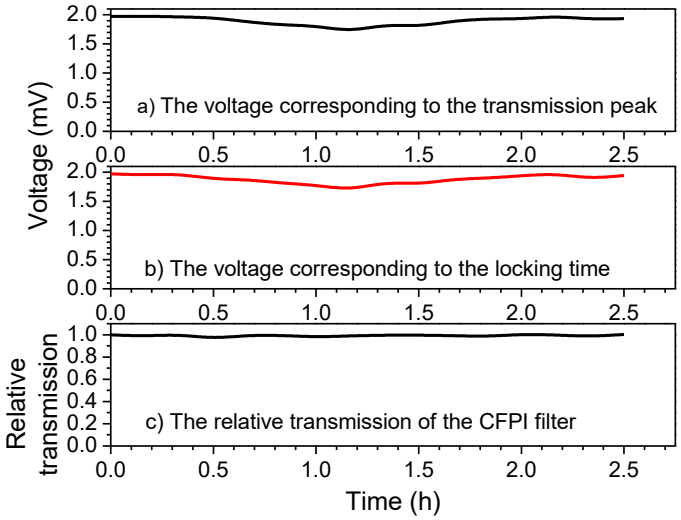

Figure 4.20 The stability of the CFPI transmission at the wavelength of 532nm in 2.5 hours.

The mean value and standard deviation of the relative transmission are 0.99 and 0.011, respectively. Therefore, the relative error of the transmission is 1.1%. This means that the stability of the transmission is 1.1% in 2.5 hours.

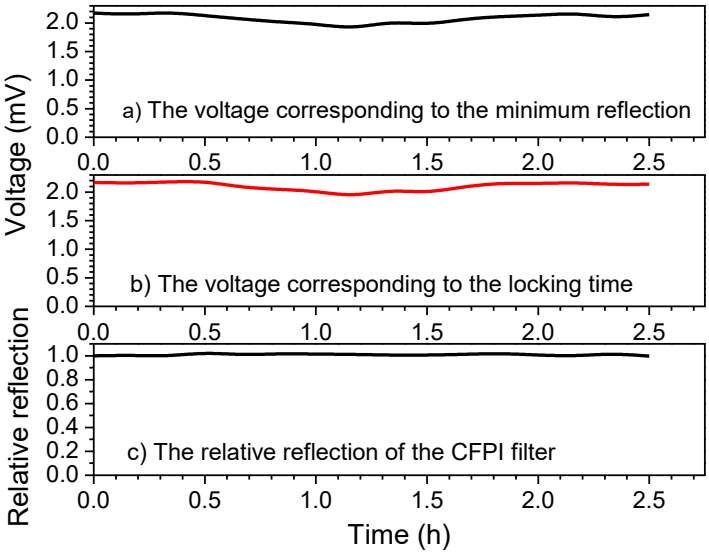

Figure 4.21 The stability of the CFPI reflection at the wavelength of 532nm in 2.5 hours.

The mean value and standard deviation of the relative reflection are 1.0087 and 0.0099, respectively. Therefore, the relative error of the transmission is 0.98%. This means the stability of the transmission is 0.98% in 2.5 hours.

5 Error analysis

The confocal Fabry-Perot interferometer (CFPI) used in the spectral analysis system is resonant for the multimode light scattered by the atmospheric molecules and aerosols. In the case of multi-mode resonance, the odd and even spatial modes degenerate into two distinct groups. According to section 3.1.2.2, the transmission of the CFPI for multimode incident light is described by a Lorentzian curve defined by the following expression

$$T_{\mathrm{CFPI}}\left(T_{pk}, W_{FWHM}, \nu\right) = \frac{T_{pk}}{1 + \left[\frac{2\mathcal{F}^*}{\pi}\right]^2 \sin^2\left(\frac{4\pi r\nu}{c}\right)} = \frac{T_{pk}}{1 + \left[\frac{2FSR}{\pi W_{FWHM}}\right]^2 \sin^2\left(\frac{\pi\nu}{FSR}\right)} \tag{5.1}$$

where,

T_{pk} is the peak transmission of the CFPI at 532nm,

$\mathcal{F}^*$ is the finesse of the CFPI at 532nm,

r is the confocal spacing,

ν is the frequency of the incident light,

FSR is the frequency difference between the adjacent transmission peaks and $FSR = c/4r$ for multimode incident light,

W_{FWHM} is the bandwidth (*FWHM*) of the CFPI transmission at 532nm,

c is the light speed.

Due to the confocal configuration of the CFPI, r equals to the radius of the cavity mirrors. Therefore, the performance of the CFPI only depends on the peak transmission T_{pk} and the bandwidth W_{FWHM} at the wavelength of 532nm. These two parameters have been measured and presented in chapter 4.

According to the expressions (3.56), (3.57), (3.58), (3.59), the transmission and reflection of light backscattered by aerosols and atmospheric molecules are

$$\kappa_{AA}\left(T_{pk}, W_{FWHM}\right) = \int_{-\infty}^{\infty} W_a(\nu) T_{\mathrm{CFPI}}\left(T_{pk}, W_{FWHM}, \nu\right) d\nu \tag{5.2}$$

$$\kappa_{AM}\left(T_{pk}, W_{FWHM}\right) = 1 - \kappa_{AA}\left(T_{pk}, W_{FWHM}\right) \tag{5.3}$$

$$\kappa_{MA}(T_{pk}, W_{FWHM}) = \int_{-\infty}^{\infty} W_m(\nu) T_{\mathrm{CFPI}}(T_{pk}, W_{FWHM}, \nu) d\nu \tag{5.4}$$

$$\kappa_{MM}(T_{pk}, W_{FWHM}) = 1 - \kappa_{MA}(T_{pk}, W_{FWHM}) \tag{5.5}$$

where, κ_{MM} is the fraction of molecular light detected in the molecular channel, κ_{AM} is the fraction of aerosol light detected in the molecular channel, κ_{MA} is the fraction of molecular light detected in the aerosol channel, and κ_{AA} is the fraction of aerosol light detected in the aerosol channel. $W_a(\nu), W_m(\nu)$ are the normalized aerosol and molecular Doppler broadening spectrum.

According to chapter 3, since the same type of PMT detector is used in aerosol channel and molecular channel, η_T and η_R are assumed to have the same value η. The received signals in the aerosol channel and molecular channel are described as follows

$$S_{tot\_T} = \frac{E\lambda_0}{hc}\frac{\pi D^2}{4}\frac{\kappa_{AA}\beta_a(\lambda_0, z) + \kappa_{MA}\beta_m(\lambda_0, z)}{R(z)^2}\exp\left\{\frac{-2}{\cos(\Phi)}\int_z^{z_{sat}}[\alpha_a(\lambda_0, z') + \alpha_m(\lambda_0, z')]dz'\right\}\Delta z_{LOS} T_{RX} T_{TX}\eta \tag{5.6}$$

$$S_{tot\_R} = \frac{E\lambda_0}{hc}\frac{\pi D^2}{4}\frac{\kappa_{AM}\beta_a(\lambda_0, z) + \kappa_{MM}\beta_m(\lambda_0, z)}{R(z)^2}\exp\left\{\frac{-2}{\cos(\Phi)}\int_z^{z_{sat}}[\alpha_a(\lambda_0, z') + \alpha_m(\lambda_0, z')]dz'\right\}\Delta z_{LOS} T_{RX} T_{TX}\eta \tag{5.7}$$

where,

1) S_{tot_T} and S_{tot_R} are the numbers of received photo-electrons in the transmitted channel and reflected channel, respectively.
2) E and λ_0 is the energy and wavelength of the laser, respectively.
3) D is the diameter of the receiving telescope.
4) $R(z)$ is the range from the atmospheric layer to the instrument at altitude z_{sat}, $R(z) = (z_{sat} - z)/\cos(\Phi)$ with the line-of-sight or laser beam incidence angle Φ.

5) $\beta_a(\lambda_0, z)$ and $\beta_m(\lambda_0, z)$ are the aerosol and molecular backscattering coefficients at the altitude z and the wavelength λ_0, respectively.
6) $\alpha_a(\lambda_0, z)$ and $\alpha_m(\lambda_0, z)$ are the aerosol and molecular extinction coefficients at the altitude z and the wavelength λ_0, respectively.
7) Δz_{LOS} is the depth of the illuminated layer, $\Delta z_{LOS} = \Delta z/\cos(\Phi)$ with range gate resolution Δz.
8) T_{TX} and T_{RX} are the transmission of the transmit and receive optics, respectively.
9) *c* is the speed of light and *h* is Planck's constant.

The attenuated backscattering signal scattered by atmospheric molecules is expressed as follows

$$S_m(\lambda_0, z) = \frac{E\lambda_0}{hc}\frac{\pi D^2}{4}\frac{\beta_m(\lambda_0, z)}{R(z)^2}\exp\left\{\frac{-2}{\cos(\Phi)}\int_z^{z_{sat}}[\alpha_a(\lambda_0, z') + \alpha_m(\lambda_0, z')]dz'\right\}\Delta z_{LOS}T_{RX}T_{TX}\eta \quad (5.8)$$

Then

$$S_{tot\_T}(\lambda_0, z) = \left((R_\beta - 1)\kappa_{AA} + \kappa_{MA}\right)S_m(\lambda_0, z) \quad (5.9)$$

$$S_{tot\_R}(\lambda_0, z) = \left((R_\beta - 1)\kappa_{AM} + \kappa_{MM}\right)S_m(\lambda_0, z) \quad (5.10)$$

According to section 3.1.4, the number of photons backscattered by atmospheric molecules $N_m(\lambda_0, z)$ and the number of photons backscattered by aerosols $N_a(\lambda_0, z)$ are as follows

$$N_m(\lambda_0, z) = \frac{1}{\eta}\frac{\kappa_{AA}S_{tot\_R}(\lambda_0, z) - \kappa_{AM}S_{tot\_T}(\lambda_0, z)}{\kappa_{AA}\kappa_{MM} - \kappa_{AM}\kappa_{MA}} \quad (5.11)$$

$$N_a(\lambda_0, z) = \frac{1}{\eta}\frac{\kappa_{MM}S_{tot\_T}(\lambda_0, z) - \kappa_{MA}S_{tot\_R}(\lambda_0, z)}{\kappa_{AA}\kappa_{MM} - \kappa_{AM}\kappa_{MA}} \quad (5.12)$$

According to the equations (5.9), (5.10), (5.11), (5.12), the errors in retrieval of the molecular and aerosol signals, which result in the errors of retrieved extinction and backscattering coefficients, come primarily from three sources: noise from the detector, error due to deviation in the CFPI transmission, and error in retrieval of the molecular and aerosol signals due to fluctuation in the CFPI transmission. The

deviation and fluctuation in the CFPI transmission come from the errors in the peak transmission and the finesse of the CFPI. These will be analyzed in the next sections.

5.1 Error due to the deviation in the CFPI transmission

Photomultiplier tubes (PMTs) are used to detect the backscattering light in the aerosol channel and molecular channel. The PMTs work in photon counting mode due to the advantages in signal-to-noise ratio and stability over the analog mode. In the photon counting mode in which randomly generated photons are detected, the number of signal pulses counted during a certain period of time follows a Poisson distribution. If N is the average number of signal pulses, the detector noise introduced by the PMT can be expressed as [44]

$$n_{tot} = \sqrt{N_{ph} + 2(N_b + N_d)} \tag{5.13}$$

where,

N_{ph} is the number of counts of signal photons,

N_b is the number of counts of background photons,

N_d is the number of dark counts.

The dark current pulses are distributed on the lower pulse height side. This is because the dark current includes thermal electrons not only from the photocathode but also from dynodes. Therefore, some dark current component can be effectively eliminated by setting a proper discrimination level without reducing much of the signal component. On the other hand, the background light can be disregarded when the spaceborne HSRL works at night. In these conditions, the noise in the transmitted channel n_T and the noise in the reflected channel n_R are expressed as

$$n_T = \sqrt{S_{tot\_T}(\lambda_0, z)} \tag{5.14}$$

$$n_R = \sqrt{S_{tot\_R}(\lambda_0, z)} \tag{5.15}$$

The errors in retrieval of the molecular and aerosol signals due to the detector noise and κ-value are

$$\Delta N_m(\lambda_0, z) = \frac{1}{\eta}\frac{\sqrt{(\kappa_{AA})^2(n_R)^2 + (\kappa_{AM})^2(n_T)^2}}{|\kappa_{AA}\kappa_{MM} - \kappa_{AM}\kappa_{MA}|} = \frac{1}{\eta}\frac{\sqrt{(\kappa_{AA})^2 S_{tot\_R}(\lambda_0, z) + (\kappa_{AM})^2 S_{tot\_T}(\lambda_0, z)}}{|\kappa_{AA}\kappa_{MM} - \kappa_{AM}\kappa_{MA}|} \tag{5.16}$$

$$\Delta N_a(\lambda_0, z) = \frac{1}{\eta}\frac{\sqrt{(\kappa_{MM})^2(n_T)^2 + (\kappa_{MA})^2(n_R)^2}}{|\kappa_{AA}\kappa_{MM} - \kappa_{AM}\kappa_{MA}|} = \frac{1}{\eta}\frac{\sqrt{(\kappa_{MM})^2 S_{tot\_T}(\lambda_0, z) + (\kappa_{MA})^2 S_{tot\_R}(\lambda_0, z)}}{|\kappa_{AA}\kappa_{MM} - \kappa_{AM}\kappa_{MA}|} \tag{5.17}$$

So, the relative errors of the retrieved molecular and aerosol signals are

$$e1_m\left(T_{pk}, \mathcal{F}^*, \lambda_0, z\right) = \frac{\Delta N_m(\lambda_0, z)}{N_m(\lambda_0, z)} = \frac{\sqrt{(\kappa_{AA})^2 S_{tot\_R}(\lambda_0, z) + (\kappa_{AM})^2 S_{tot\_T}(\lambda_0, z)}}{|\kappa_{AA} S_{tot\_R}(\lambda_0, z) - \kappa_{AM} S_{tot\_T}(\lambda_0, z)|} = \frac{\sqrt{(\kappa_{AA})^2 \kappa_{MM} + (\kappa_{AM})^2 \kappa_{MA} + (R_\beta - 1)\kappa_{AA}\kappa_{AM}}}{|\kappa_{AA}\kappa_{MM} - \kappa_{AM}\kappa_{MA}|}\frac{1}{\sqrt{S_m(\lambda_0, z)}} \tag{5.18}$$

$$e1_a\left(T_{pk}, \mathcal{F}^*, \lambda_0, z\right) = \frac{\Delta N_a(\lambda_0, z)}{N_a(\lambda_0, z)} = \frac{\sqrt{(\kappa_{MM})^2 S_{tot\_T}(\lambda_0, z) + (\kappa_{MA})^2 S_{tot\_R}(\lambda_0, z)}}{|\kappa_{MM} S_{tot\_T}(\lambda_0, z) - \kappa_{MA} S_{tot\_R}(\lambda_0, z)|} = \frac{\sqrt{(\kappa_{AA}(\kappa_{MM})^2 + \kappa_{AM}(\kappa_{MA})^2)(R_\beta - 1) + \kappa_{MM}\kappa_{MA}}}{(R_\beta - 1)|\kappa_{AA}\kappa_{MM} - \kappa_{AM}\kappa_{MA}|}\frac{1}{\sqrt{S_m(\lambda_0, z)}} \tag{5.19}$$

The designed peak transmission of the CFPI can be calculated by the following expressions

$$T_{pk} = (1 + R^2)/(1 + R)^2 \tag{5.20}$$

where R is the reflectivity of the CFPI mirrors.

The designed peak transmission is calculated and the value is 0.51 for the 532nm incident light. The designed bandwidth of the CFPI at 532nm is 0.76GHz presented in section 3.3.1. According to the measurement results presented in chapter 4, the average value of the peak transmission is 0.49 and the bandwidth is 0.78GHz. Assuming the atmospheric temperature at the ground altitude is 300K. The κ-value

depending on the designed parameters and measured parameters of the CFPI are calculated and the results are shown in the following table.

Table 5.1 The calculated κ-value depending on the designed parameters and measured parameters of the CFPI.

	Calculated by designed parameters	Calculated by measured parameters
κ_{AA}	0.5083	0.4885
κ_{AM}	0.4917	0.5115
κ_{MA}	0.1735	0.1705
κ_{MM}	0.8265	0.8295

According to the parameters presented in section 3.2, when no cloud layer or dust layer are present, the detected signals at the ground altitude in the aerosol and molecular channels are calculated. Then the relative errors of the retrieved molecular and aerosol signals are obtained by using the κ-values presented in table 5.1. The relative error caused by the detector noise is calculated with the designed parameters and shown in the following table

Table 5.2 The relative error of the retrieved molecular and aerosol signals at the ground altitude calculated by the detector noise

Aerosol conditions	Aerosol Parameters	Horizontal Resolution	Vertical Resolution	Accumulated Signals (Number of Photons)	Relative error of the retrieved signals
Low pollution	β=2E-6 LR=50	50 km	1km	S_{tot_a}=6816 S_{tot_m}=12899	$e1_a$=2.1% $e1_m$=2.2%
Medium pollution	β=1E-5 LR=50	50 km	1km	S_{tot_a}=16195 s_{tot_m}=19470	$e1_a$=1.1% $e1_m$=4.9%
High pollution	β=2E-5 LR=50	50 km	1km	S_{tot_a}=16910 s_{tot_m}=18462	$e1_a$=1.0% $e1_m$=8.8%

The relative error is calculated by the measured parameters and the errors caused by the deviation of the CFPI transmission between the measured values and designed

values are shown in the following table

Table 5.3 The relative error of the retrieved molecular and aerosol signals at the ground altitude caused by the deviation of the CFPI transmission

Aerosol conditions	Relative error of the retrieved signals	Error caused by the deviation of the CFPI transmission
Low pollution	$e1_a$=2.2% $e1_m$=2.3%	$\Delta e1_a$=0.08% $\Delta e1_m$=0.09%
Medium pollution	$e1_a$=1.1% $e1_m$=5.1%	$\Delta e1_a$=0.04% $\Delta e1_m$=0.24%
High pollution	$e1_a$=1.1% $e1_m$=9.2%	$\Delta e1_a$=0.04% $\Delta e1_m$=0.44%

The above table shows that the error due to the deviation in the CFPI is much smaller than the error due to the signal-to-noise ratio of received signal in aerosol and molecular channel. So, the accuracy of the peak transmission and bandwidth of the transmission meets the design requirements.

5.2 Error from the fluctuation in the CFPI transmission

Errors from the fluctuation in the CFPI characterization are other potential source of error in the retrieval of aerosol optical properties. Errors in the κ-values comes from three sources: measurements of cavity transmission, altitude resolved atmospheric models of temperature and pressure, and the fluctuation of the cavity transmission caused by the locking error between the center transmission wavelength of the CFPI and the wavelength of the laser source.

According to the measurements presented in section 4.2 and 4.4, the standard deviation of the bandwidth ΔW_{FWHM} is 0.041GHz. The relative error of the peak transmission and reflection are 0.4% and 0.33%. And the fluctuations of the peak transmission and reflection in 2.5 hours are 1.1% and 0.98%, respectively. Therefore, the standard deviation of the peak transmission is

$$\Delta T_{pk} = T_{pk} * \sqrt{(0.4\%)^2 + (1.1\%)^2} = 0.0057$$

Due to the relations: $\kappa_{MA} + \kappa_{MM} = 1$ and $\kappa_{AA} + \kappa_{AM} = 1$, the expressions of

$\mathrm{N_m}(\lambda_0, \mathrm{z})$ and $\mathrm{N_a}(\lambda_0, \mathrm{z})$ become

$$N_m(\lambda_0, z) = \frac{1}{\eta}\frac{\kappa_{AA}(S_{tot\_R}(\lambda_0, z)+S_{tot\_T}(\lambda_0, z)) - S_{tot\_T}(\lambda_0, z)}{\kappa_{AA}+\kappa_{MM} - 1} \quad (5.21)$$

$$N_a(\lambda_0, z) = \frac{1}{\eta}\frac{\kappa_{MM}(S_{tot\_T}(\lambda_0, z) + S_{tot\_R}(\lambda_0, z)) - S_{tot\_R}(\lambda_0, z)}{\kappa_{AA}+\kappa_{MM} - 1} \quad (5.22)$$

The errors in retrieval of the molecular and aerosol signals due to the fluctuation of the CFPI transmission are

$$\Delta N_m(\lambda_0, z) = \Delta N_a(\lambda_0, z) = \frac{\sqrt{(\kappa_{MM}(S_{tot\_T}+S_{tot\_R})-S_{tot\_R})^2(\Delta\kappa_{AA})^2+(\kappa_{AA}(S_{tot\_R}+S_{tot\_T})-S_{tot\_T})^2(\Delta\kappa_{MM})^2}}{\eta|\kappa_{AA}+\kappa_{MM}-1|} \quad (5.23)$$

So, the relative errors of the retrieved molecular and aerosol signals are

$$e2_m = \frac{\Delta N_m(\lambda_0, z)}{N_m(\lambda_0, z)} = \frac{\sqrt{(\kappa_{MM}(S_{tot\_T} + S_{tot\_R}) - S_{tot\_R})^2(\Delta\kappa_{AA})^2 + (\kappa_{AA}(S_{tot\_R}+S_{tot\_T}) - S_{tot\_T})^2(\Delta\kappa_{MM})^2}}{|\kappa_{AA}(S_{tot\_R}+S_{tot\_T}) - S_{tot\_T}|} = \sqrt{(R_\beta - 1)^2\left(\Delta\kappa_{AA}(T_{pk}, W_{FWHM})\right)^2 + \left(\Delta\kappa_{MM}(T_{pk}, W_{FWHM})\right)^2} \quad (5.24)$$

$$e2_a = \frac{\Delta N_a(\lambda_0, z)}{N_a(\lambda_0, z)} = \frac{\sqrt{(\kappa_{MM}(S_{tot\_T} + S_{tot\_R}) - S_{tot\_R})^2(\Delta\kappa_{AA})^2 + (\kappa_{AA}(S_{tot\_R}+S_{tot\_T}) - S_{tot\_T})^2(\Delta\kappa_{MM})^2}}{|\kappa_{MM}(S_{tot\_T} + S_{tot\_R}) - S_{tot\_R}|} = \sqrt{\left(\Delta\kappa_{AA}(T_{pk}, W_{FWHM})\right)^2 + \left(\Delta\kappa_{MM}(T_{pk}, W_{FWHM})\right)^2/(R_\beta - 1)^2} = e2_m/(R_\beta - 1) \quad (5.25)$$

According to the standard deviation of the peak transmission and bandwidth, the relative error of the retrieved molecular and aerosol signals are shown in the following table

Table 5.4 The relative error of the retrieved molecular and aerosol signals at the ground altitude caused by the fluctuation of the CFPI transmission

Aerosol conditions	Aerosol Parameters	Relative error of the retrieved signals
Low pollution	β=2E-6 LR=50	$e2_a$=0.87% $e2_m$=1.1%
Medium pollution	β=1E-5 LR=50	$e2_a$=0.58% $e2_m$=3.7%
High pollution	β=2E-5	$e2_a$=0.6%

	LR=50	$e2_m$=7.6%

The above table shows that the relative errors of the retrieved molecular and aerosol signals caused by the fluctuation of the CFPI transmission are much larger than the error caused by the deviation of the CFPI transmission. However, they are also lower than the errors caused by detector noise.

5.3 The analysis of the error caused by the stability of the CFPI transmission

According to the expressions (5.24), (5.25) and the expressions of κ-value (5.2), (5.3), (5.4), (5.5), the expressions of the relative error caused by the fluctuation of the CFPI transmission become

$$err_m(\Delta T_{pk}, \Delta W_{FWHM}) = \frac{\Delta N_m(\lambda_0, z)}{N_m(\lambda_0, z)}$$
$$= \sqrt{(R_\beta - 1)^2 \left(\left(\frac{\partial \kappa_{AA}}{T_{pk}} \Delta T_{pk}\right)^2 + \left(\frac{\partial \kappa_{AA}}{W_{FWHM}} \Delta W_{FWHM}\right)^2\right)^2 + \left(\left(\frac{\partial \kappa_{MM}}{T_{pk}} \Delta T_{pk}\right)^2 + \left(\frac{\partial \kappa_{MM}}{W_{FWHM}} \Delta W_{FWHM}\right)^2\right)^2} \quad (5.26)$$

$$err_a(\Delta T_{pk}, \Delta W_{FWHM}) = err_m(\Delta T_{pk}, \Delta W_{FWHM}) / (R_\beta - 1) \quad (5.27)$$

Based on the measured peak transmission 0.49 and the measured bandwidth 0.78GHz at 532nm, the relative errors of the retrieved molecular and aerosol signals caused by the error of the CFPI bandwidth at 532nm are calculated in the case of the peak transmission error 0.0057 (relative error 1.1%). A Monte Carlo method has been used in this calculation. The results are shown in Figure 5.1.

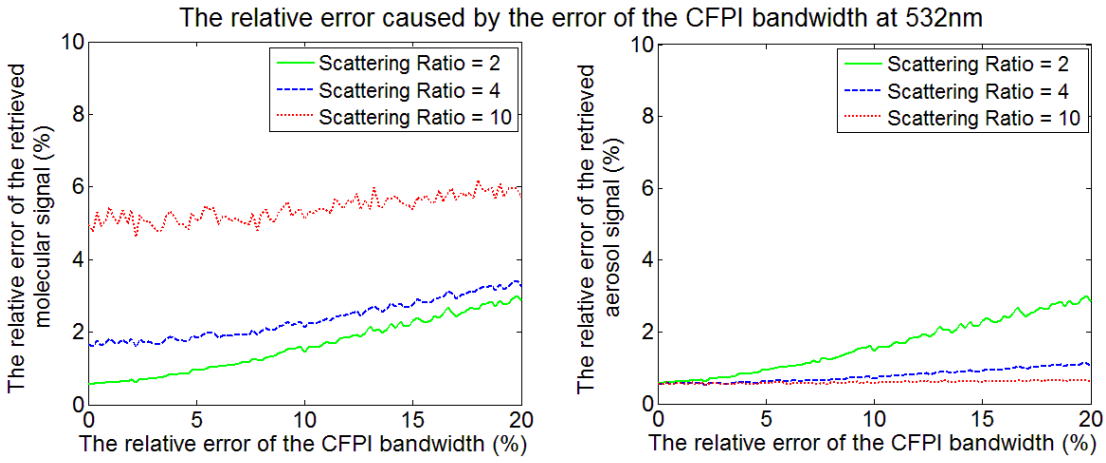

Figure 5.1 The relative errors of the retrieved molecular signal and aerosol signal caused by the error of the CFPI bandwidth in the case of the peak transmission error 0.0057 (relative error 1.1%). Colors represent the different aerosol conditions: green solid line means low air pollution; blue dash line means normal pollution and red

dot line means high pollution.

The relative errors of the retrieved molecular and aerosol signals caused by the error of the CFPI peak transmission at 532nm are also calculated in the case of the bandwidth error 0.041GHz (relative error 5.2%). The results are shown in Figure 5.2.

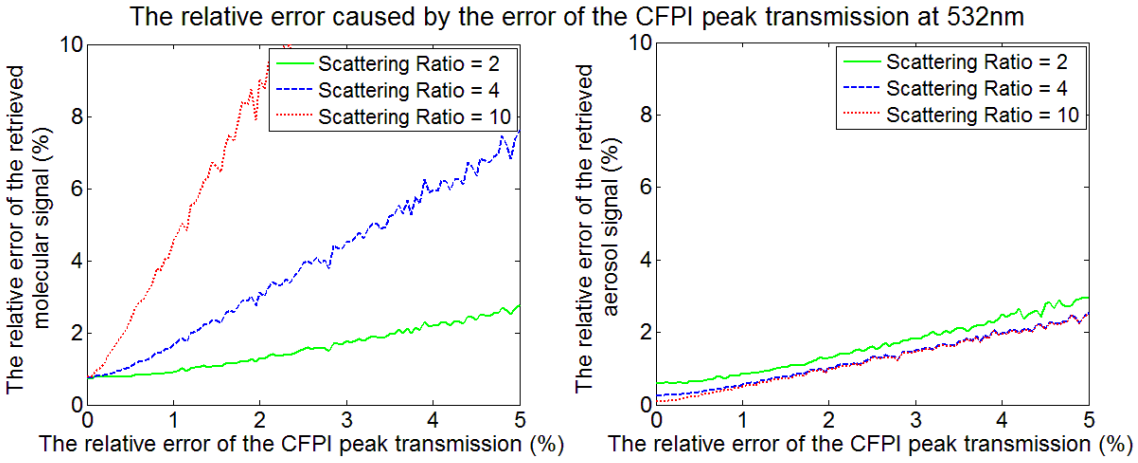

Figure 5.2 The relative errors of the retrieved molecular signal and aerosol signal caused by the error of the CFPI peak transmission in the case of the bandwidth error 0.041GHz (relative error 5.2%). Colors represent the different aerosol conditions: green solid line means low air pollution; blue dash line means normal pollution and red dot line means high pollution.

Figure 5.1 and Figure 5.2 show that the relative errors of the retrieved molecular signals (left) are higher than the relative errors of the retrieved aerosol signals (right) in both the error conditions of the CFPI peak transmission and bandwidth. The relative errors of the retrieved molecular signals are more sensitive to the error of the CFPI peak transmission than to the error of the CFPI bandwidth. With the increase of aerosol concentration, the relative errors of the retrieved molecular signals will increase and the relative errors of the retrieved aerosol signals will decrease.

6 Conclusions and future work

A spectral analysis system for a spaceborne high spectral resolution lidar (HSRL) has been developed based on the combination of an interference filter, a planar Fabry-Perot interferometer (PFPI) and a confocal Fabry-Perot interferometer (CFPI). A frequency-locking subsystem has been used to lock the center transmission wavelength of the spectral analysis system to the wavelength of the emitted laser. By the comparison of molecular absorption filter and three kinds of interferometer filters, CFPI is adopted for the high spectral resolution filter of the spaceborne HSRL due to the higher spectral resolution, larger *étendue* and the adaption to the space platform. The parameter requirements of the spectral analysis system are obtained by the system simulation of the spaceborne HSRL. The spectral analysis system including the spectral filters and the frequency-locking subsystem has been designed and realized. The spectral analysis system has also been tested and an error analysis has been performed. The test results show that the relative errors of the retrieved molecular and aerosol signals caused by the error of the CFPI peak transmission and bandwidth are lower than the error caused by the signal noise and below the error limit.

The spectral analysis system presented in this thesis represents a kind of practical high spectral resolution method that can be applied to spaceborne HSRL. The use of a combination of interference filter, PFPI spectral filter and CFPI spectral filter in spaceborne HSRL is novelty. The CFPI has several key advantages over gas absorption cells and other interferometers. Unlike gas absorption cells, CFPI has no problems of leak and vapor formation which would render the gas absorption cells useless. The CFPI can provide high spectral resolution and large *étendue* simultaneously and is much less sensitive to alignment errors and vibrations than other interferometers. The developed two-stage frequency-locking technique is also a novel technique and can be used whether the locked laser is a pulsed laser or a continuous laser. Test shows that it is a robust method and has very good long-term stability.

The future work will regard the assembly of an entire prototype of the spaceborne HSRL and performing a field testing campaign.

References

[1] V. A. Kovalev and W. E. Eichinger, Elastic Lidar: Theory, Practice and Analysis Methods. John Wiley and Sons, New York (2004).

[2] Hoffman D.S., “Confocal Fabry-Perot Interferometer Based High Spectral Resolution Lidar”, PhD Thesis, Montana State University, Bozeman, 3 (2012).

[3] S. Groß, etc. “Airborne high spectral resolution lidar observation of pollution aerosol during EUCAARI-LONGREX”, Atmospheric Chemistry and Physics, 13, 2435–2444 (2013).

[4] IPCC, 2013: Climate Change 2013: The Physical Science Basis. Contribution of Working Group I to the Fifth Assessment Report of the Intergovernmental Panel on Climate Change [Stocker, T.F., D. Qin, G.-K. Plattner, M. Tignor, S.K. Allen, J. Boschung, A. Nauels, Y. Xia, V. Bex and P.M. Midgley (eds.)]. Cambridge University Press, Cambridge, United Kingdom and New York, NY, USA, 1535 pp.

[5] S. Fuzzi,etc. “Particulate matter, air quality and climate: lessons learned and future needs”, Atmospheric Chemistry and Physics, 15, 8217–8299 (2015).

[6] Weitkamp C., Lidar Range-Resolved Optical Remote Sensing of the Atmosphere, Springer, 2005.

[7] Richard B Miles. et al. “Laser Rayleigh scattering”, MEASUREMENT SCIENCE AND TECHNOLOGY, 12 (2001) R33–R51.

[8] Chiao-Yao She, “Spectral structure of laser light scattering revisited: bandwidths of nonresonant scattering lidars”, APPLIED OPTICS, Vol. 40, No. 27, 2001.

[9] Martha Wallis Dawsey. “INVESTIGATION INTO HIGH SPECTRAL RESOLUTION LIDAR TECHNOLOGIES”, PhD thesis, THE UNIVERSITY OF ARIZONA, 29(2013)

[10] Hair J. W. et al. “Airborne High Spectral Resolution Lidar for profiling aerosol optical properties”, Applied Optics, 6734-6753 (2008).

[11] S. P. Burton et al. “Aerosol classification from airborne HSRL and comparisons with the CALIPSO vertical feature mask”, Atmospheric Measurement Techniques, 6, 1397–1412, 2013.

[12] D. Müller et al. “Airborne Multiwavelength High Spectral Resolution Lidar (HSRL-2) observations during TCAP 2012: vertical profiles of optical and microphysical properties of a smoke/urban haze plume over the northeastern coast of the US”, Atmospheric Measurement Techniques, 7, 3487–3496, 2014.

[13] Dong Liu et al. “System analysis of a tilted field-widened Michelson interferometer for high spectral resolution lidar”, OPTICS EXPRESS, Vol. 20, No. 2,2012.

[14] Arnaud Hélière , Robert Gelsthorpe. “ATLID, THE ATMOSPHERIC LIDAR ON BOARD THE EARTHCARE SATELLITE”, European Space Agency, The Netherlands

[15] J.-L. Bézy. “ ESA’s Earth Observation Lidar Missions and Critical Technology Developments”, ICSO Rhodes, 04-08 October 2010

[16] David M. Winker et al., “Initial performance assessment of CALIOP”, GEOPHYSICAL RESEARCH LETTERS, VOL. 34, L19803, doi:10.1029/2007GL030135, 2007.

[17] OLIVER REITEBUCH et al., “The Airborne Demonstrator for the Direct-Detection Doppler Wind Lidar ALADIN on ADM-Aeolus. Part I: Instrument Design and Comparison to Satellite Instrument”, JOURNAL OF ATMOSPHERIC AND OCEANIC TECHNOLOGY, VOLUME 26,2009.

[18] John E. Yorks et al., “CATS Algorithm Theoretical Basis Document Level 1 and Level 2 Data Products”, 17 (2016).

[19] Joao Pereira do Carmo et al. “ATLID, ESA ATMOSPHERIC LIDAR DEVELOPEMENT STATUS”, EPJ Web of Conferences,119, 04003 (2016).

[20] W. Demtröder, Laser Spectroscopy: Vol. 1: Basic Principles , 4th ed., Springer, 2008.

[21] Ulrike Paffrath ,“Performance assessment of the Aeolus Doppler wind lidar prototype,” PhD Thesis, Technical University of Munich, Munich, 2006.

[22] B. Witschas, Analytical model for Rayleigh–Brillouin line shapes in air, APPLIED OPTICS, 268-269 (2011).

[23] G. D. Boyd and J. P. Gordon, “Confocal Multimode Resonator for Millimeter

Through Optical Wavelength Masers", Bell Sys. Tech. J. 40, 453 (1961).

[24] Charles Gaomi Zha, "Characterizing a Fabry-Perot Transfer Cavity", Rice University, 2013.

[25] Michael Hercher, "The Spherical Mirror Fabry-Perot Interferometer", APPLIED OPTICS , Vol. 7, No. 5, 1968.

[26] G.J. MARSEILLE et al. "Simulation of Wind Profiles from a Space-borne Doppler Wind Lidar", Q. J. R. Meteorol. Soc. (2003), 129, pp. 3079–3098 doi: 10.1256/qj.

[27] J. R. Johnson, "A High Resolution Scanning Confocal Interferometer" Appl. Opt. 7, 1061-1072,1968.

[28] Rich Ferrare et al. "Spaceborne Aerosol and Ozone Lidars for Air Quality Applications", NCAR Community Workshop on Air Quality Remote Sensing from Space, February, 2006.

[29] X. Wang, C. Song, A. Boselli, M. Iarlori, V. Rizi, N. Spinelli, "SYSTEM SIMULATION OF SPACEBORNE AND AIRBORNE HIGH SPECTRAL RESOLUTION LIDAR FOR AEROSOL MONITORING" , XXXVIII Meeting of the Italian Section of the Combustion Institute, doi: 10.4405/38proci2015.XI3

[30] Changbo Song, Antonella Boselli, Alessia Sannino, Yiming Zhao, Nicola Spinelli, Xuan Wang, "Analysis of the influence of system parameters on the measurement accuracy of a high spectral resolution lidar", Lidar Technologies, Techniques, and Measurements for Atmospheric Remote Sensing XII, Proc. of SPIE Vol. 10006,2016 doi: 10.1117/12.2241971

[31] https://www.thorlabs.com/newgrouppage9.cfm?objectgroup_ID=859.

[32] Neal, K.A. (2009), "A Confocal Fabry-Perot Interferometer for Use in Lidar Receivers." Master's Thesis, Montana State University, Bozeman, Montana, USA.

[33] Amnon Yariv, Pochi Yeh."Photonics: optical electronics in modern communications",6th ed., Oxford University Press, 2007.

[34] Peter W. Milonni, Joseph H. Eberly, "Laser physics", John Wiley & Sons, Inc., 2010. ISBN 978-0-470-38771-9.

[35] https://www.rp-photonics.com/mode_matching.html.

[36] Neal H. Zaun et al. “Solid-etalon for the CALIPSO lidar receiver”, Earth Observing Systems IX, Proc. of SPIE Vol. 5542 (SPIE, Bellingham, WA, 2004) doi: 10.1117/12.559883.

[37] CVI Optical Components and Assemblies, p280-281, 2005, CVI Laser, LLC.

[38] Luca Giovannelli, “Study of a Fabry-Perot interferometer prototype for space applications”, Master Thesis, University of Rome Tor Vergata.

[39] H.Angus Macleod, “Thin-Film Optical Filters”, 4th ed., CRC Press (Taylor & Francis Group), 2010.

[40] Dipl.-Phys. Katharina Möhle, “Piezoelectrically Tunable Optical Cavities for the Gravitational Wave Detector LISA”, PhD thesis, Humboldt-Universität zu Berlin, 2013.

[41] Paolo Farinello, “Solid-State Lasers for High Spectral Resolution Lidar Applications”, PhD thesis, University of Pavia, 2016

[42] PZ 96E User Manual S-310, S-311, S-314, S-315, S-316 Tilt Platforms and Z-axis Positioners, Release: 1.10 Date: 2003-02-04.

[43] K. P. Birch and M. J. Downs, “An Updated Edlén Equation for the Refractive Index of Air”, Metrologia 30, 155 (1993).

[44] Photon Counting, Using Photomultiplier Tubes. Technical Information, Hamamatsu Corp. 2001.

Acknowledgements

This PhD thesis is financially supported by international scientific cooperation project LISA (LIdar for Space study of the Atmosphere) between Consorzio Nazionale Interuniversitario per le Scienze Fisiche della Materia (CNISM) and Beijing Research Institute of Telemetry (BRIT). The international cooperation project is operated in the framework of China-Italy Laser Remote Sensing Joint Research Center. I would also like to thank Chinese Ministry of Science and Technology (MOST) for partly funding the international cooperation project. Undertaking this PhD has been a truly life-changing experience for me and it would not have been possible to do without the support and guidance that I received from many people.

First and foremost, I would like to thank my supervisors for their great supports and helps. I would like to express my deepest gratitude to my supervisor, Dr. Xuan Wang, for his excellent guidance, caring and patience. I learned a lot from him, including a wide range of knowledge in the field, effective research methods and practical issues beyond the textbooks. Without his guidance and constant feedback this PhD would not have been achievable. I would also like to thank my co-supervisor, Prof. Nicola Spinelli, for his continuous guidance, novel suggestions and providing me an excellent atmosphere for doing research. He also patiently corrected my dissertation and financially supported for my attendance at various meetings. I would like to thank my coordinator, Prof. Salvatore Capozziello, for his guidance and financing me for international conferences. I am especially thankful to Mr. Guido Celentano for his kindness and great help during the whole period of my PhD study.

I would like to thank Dr. Alberto Porzio for his guidance and suggestion on confocal Fabry-Perot cavity. I am very grateful to Giuseppe Passeggio for his supports on optomechanics. I would also like to thank BrightSolutions Srl for supporting my experiments, Dr. Marco Iarlori and Prof. Vincenzo Rizi, Universit à degli Studi dell'Aquila, for the discussions on lidar signal simulations. A special acknowledgement goes to Prof. Riccardo Bruzzese for his suggestions and corrections

on my dissertation. I would also like to thank Antonella Boselli for her great help. Many thanks to lab colleagues Alessia Sannino, Gaetano Sasso, Carmen De Marco, Francesco Di Guida and all the members in our group for their scientific helps during the research program and also helps in daily life.

I would like to thank many people from Beijing Research Institute of Telemetry (BRIT). I am very grateful to Yiming Zhao for her support on my research project and a big thanks to Chao Chu for his support and help in my difficult time. My sincere thanks also go to Juling Zhan for her continuous support and help during the whole period of my PhD study. I would like to specially thank Lianghai Li, director of BRIT, Yong Yu, vice director of BRIT and Yanhua Li, former director of BRIT for giving me the opportunity to go abroad for pursuing the doctorate degree.

I would also like to thank my friends, Sen Mou and Yuntao He, for their always willing to help and give their best suggestions. Special thanks to Elaheh for her warm help to correct the writing of my dissertation. Many thanks to Mr. Jijil, Ms.Susan, Ms.Deborah, Mr.Ehsan, Mr. Atanu, Mr. Sam, Mr.Anoop, Mr.Akif, Ms.Fatema, Mr. Yue Yu, Mr. Jian Xiao, Mr. Chenkai Qu and all my friends in Naples. I am very pleased for having a happy time with you.

Finally, I would like to thank my wife, Jing Gong. She undertook a lot of family work for supporting me to go abroad for the doctoral study. She was always there cheering me up, giving me strong support and even helps me to correct the writing of my dissertation. I would like to say sorry to my son, Ruijie Song. I could not spend more time with him, but he still brought me a lot of happiness when I called him. I would like to thank my parents and my parents-in-law, they always gave me great support and encouragement. I would also like to thank my two brothers and all the people who support and help me.

Naples, Italy
April, 2017

Changbo Song